The Weak, Strong, and Coherent Regimes of Fröhlich Condensation and their Applications to Terahertz Medicine and Quantum Consciousness

Jeffrey R. Reimers[†*], Laura K. McKemmish[†], Ross H. McKenzie[‡], Alan E. Mark[¶], and Noel S. Hush[‖]

†: School of Chemistry, The University of Sydney, NSW 2006 Australia

‡: School of Physical Sciences, The University of Queensland, QLD 4072, Australia

¶: School of Molecular and Microbial Sciences and Institute for Molecular Biosciences, The University of Queensland, QLD 4072, Australia

‖: School of Molecular and Microbial Biosciences, The University of Sydney, NSW 2006 Australia

* to whom correspondence should be sent, email reimers@chem.usyd.edu.au phone +61(2)93514417 fax +61(2)93513329

SUPPORTING INFORMATION

A. Fröhlich's model

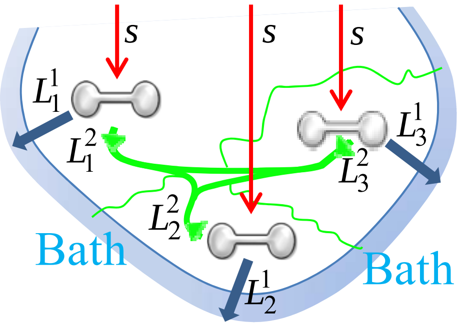

Figure 1 from the main text depicts Fröhlich's model for energy flow through a complex system. The system of interest is taken to consist of a number *Z* of coupled oscillators whose collective motions occur at frequencies ω_i (for $i = 1$ to Z) in a band of finite width at average frequency ω_0. The model does not consider the form of the dispersion of these frequencies, but an important property is the lowest frequency ω_1. These collective motions are each fed energy at the rate of *s* per unit time,

$$\frac{\mathrm{d}E_i}{\mathrm{d}t} = s\,, \tag{6}$$

while two-body "collisions" with surrounding bath states dissipate this energy at the rate of

$$L_i^1 = \phi(n_i e^{\hbar\omega_i/kT} - 1 - n_i)\,. \tag{7}$$

In this equation, ϕ is the rate of energy gain at 0 K if one quantum of excitation is present, $\hbar$ is Planck's constant $h/2\pi$, k is Boltzmann's constant, T is the bath temperature, and n_i is the *average* number of quanta of excitation of collective mode *i*. In addition, three-body interactions involving two system states and the bath redistribute the energy amongst the oscillators, with the net rate of energy loss from oscillator *i* being

$$L_i^2 = \chi\sum_{j=1}^{Z} n_i(1+n_j)e^{\hbar(\omega_i-\omega_j)/kT} - n_j(1+n_i) \tag{8}$$

for scaling factor χ. Equations 2-3 arise from the detailed balance requirement that equilibrium is established whenever $s = 0$, with the average number of quanta in each mode given by the Planck distribution function (main text Eqn. (1))

$$n_i^T = \left(e^{\hbar\omega_i/kT} - 1\right)^{-1} \tag{1}$$

depicting a canonical energy distribution. Such an energy distribution is a requirement of most models for chemical reaction kinetics, eg., the Arrhenius equation and transition-state theory.

B. **Analytical Properties of Fröhlich’s model deduced from the simulations**

The total number of quanta *N* evaluated across the full parameter space (see Section E) is well approximated by

$$N \approx N^{\chi=0} + Z\frac{s}{\varphi}n_1^T . \tag{9}$$

This equation is similar to Fröhlich’s equation, Eqn. 2 from the main text, but applies beyond the high-temperature limit for which the original equation was derived.

To measure the energy present in the system oscillations as a result of the steady-state energy flow from input source to bath, the effective system temperature is defined from the total system energy *E* using the definition

$$E = \sum_{i=1}^{Z} n_i \hbar\omega_i = \sum_{i=1}^{Z} \left(e^{\hbar w_i / kT_S} - 1\right)^{-1} \hbar\omega_i . \tag{10}$$

Over all of the parameter space examined in the simulations (see Section E), this effective temperature is well represented by

$$\frac{T_S}{T} \approx 1 + \frac{s}{\phi} e^{-\hbar\omega_0 / 2kT} . \tag{11}$$

C. **The Wu-Austin Hamiltonian**

Wu and Austin (*33-35*) proposed a dynamical model containing the *Z* system modes connected to harmonic baths representing the energy input source and the surrounding thermal-relaxation bath. For Z_B relaxation-bath modes *k* of frequency Ω_k and Z_I input modes *l* of frequency Ω'_l, their Hamiltonian is (main text Eqn (5))

$$H = \sum_{i=1}^{Z} \hbar\omega_i a_i^\dagger a_i + \sum_{k=1}^{Z_B} \hbar\Omega_k b_k^\dagger b_k + \sum_{l=1}^{Z_I} \hbar\Omega'_l\, c_l^\dagger c_l + \sum_{i=1}^{Z} \sum_{l=1}^{Z_I} \gamma a_i c_l^\dagger + \gamma^\dagger a_i^\dagger c_l$$

$$+ \sum_{i=1}^{Z} \sum_{j=1}^{Z_B} \sum_{k=1}^{Z_B} \alpha a_i b_j^\dagger b_k + \alpha^\dagger a_i^\dagger b_j b_k^\dagger + \sum_{i=1}^{Z} \sum_{j=1}^{Z} \sum_{k=1}^{Z_B} \beta a_i a_j^\dagger b_k + \beta^\dagger a_i^\dagger a_j b_k^\dagger \qquad (5)$$

where a_i, b_k, and c_l are creation operators for the system, bath, and input oscillators, respectively. Further, they assumed that unspecified processes maintain the bath and input oscillators in equilibrium canonical distributions at temperatures *T* and T_I, respectively. We implement these constraints using Nose-Hoover thermostats (*42*) with time constants of 0.1 ps each. Only linear frequency dispersion amongst $Z = 25$ source oscillators is considered, while a uniform spectral distribution of the bath and input oscillators is assumed, choosing $Z_B = 430$ bath modes and $Z_I = 200$ input modes; as demonstrated in Supporting Information, all simple properties of the (quantum (*43, 44*)) dynamics are converged to the infinite-mode limit using these numbers of oscillators.

The remaining parameters present in the Wu-Austin Hamiltonian are the couplings α, β, and γ; these may be related to mode-specific Fröhlich-like parameters using (in the high-temperature limit for simplicity) (*49-51*)

$$s_i = \frac{k Z_S \gamma^2 (T_I - T_{Si})}{\hbar^2 \omega_i} \quad , \qquad (12)$$

$$\phi_i = \frac{k^2 T^2 \alpha^2}{\hbar^3} \sum_{j=1}^{Z_B} \frac{1}{\Omega_j (\Omega_j + \omega_i)} \exp \frac{\Omega_j}{kT} \quad , \qquad \text{and} \qquad (13)$$

$$\chi_i = \frac{k^2 T \beta^2}{\hbar^3 N} \sum_{j \neq i = 1}^{Z} \frac{T_{Sj}}{\omega_j \, | \omega_j - \omega_i |} \quad , \qquad (14)$$

where T_{Si} is the effective temperature of system mode i. The simulations described later reveal that these s_i rates are very close to Fröhlich's parameter s and indeed indicate the energy flow into the system modes from the input. It is more difficult to establish a physical connection between the Wu-Austin quantities ϕ_i, χ_i and Fröhlich's parameters ϕ, χ, however. The energy flows ϕ and ϕ_I have different functional dependences while the bath thermostats provide non-linear coupling even when $\beta = 0$ making the illustrative $\chi = 0$ scenario unattainable.

D. **Methods**

The steady state solution to Fröhlich's equations, Eqn. 6-8, is evaluated by two independent methods. First, Eqns. 6-8 are solved directly by numerical solution to the differential equations. A fourth-order Runga-Kutta method is used with adaptive time step and trajectory duration. The time step used varied from 10^{-6} ϕ/kT (rare) to 0.5 ϕ/kT (common). Very short time steps were required especially when the condensate forms and when $\omega_0/kT = 10$. Second, the steady-state solution was found by solution of the Equations 7-11 from Fröhlich's treatise (*1*). These lead to:

$$A = 1 - \frac{\chi}{\phi + N\chi}\frac{s}{\phi}\sum_{i=1}^{Z} e^{-\hbar\omega_i / kT}\ , \tag{15}$$

$$n_i = \left(1 + \frac{s}{\phi}\right)\left(Ae^{\hbar\omega\ / kT} - 1\right)^{-1} \quad \text{, and} \tag{16}$$

$$N = \sum_{i=1}^{Z} n_i \tag{17}$$

which are solved for a self-consistent solution starting with a trial value of N. If the value of N used (in Eqn. 15) in iteration k of this procedure is N_k and that deduced from Eqn. 17 is N_{k+1}, the calculation procedure minimizes $N_{k+1} - N_k$. Initial values N_0 are obtained by extrapolation from results obtained either at smaller values of χ/ϕ or at larger values of $\hbar\omega_0 / kT$. A Newton-Raphson procedure is used for finding the root of the function, if possible. For arbitrary values of N_k, a solution cannot always be found with physically meaningful values, ie., $0 < A \leq 1$ and $n_i > 0$. In general the function $N_{k+1} - N_k$ has a dense manifold of roots but of these only one is physically meaningful. When the Newton-Raphson procedure cannot find this one root, grid searching using increasingly finer and finer grids is performed. The results obtained from the two computational procedures are in excellent agreement.

When the additional terms L_i^3 are added to Fröhlich's equations (see Section F), the steady state is obtained from numerical solution to the differential equations only.

The coherence lifetime arising from the quantum dynamics of the lowest-frequency mode in the Wu-Austin model is determined from the calculated linewidths of the power spectrum $A(\omega)$ of the dynamics, obtained from the Fourier transform

$$A(\omega) = \int_{-\infty}^{\infty} a(t) e^{-i\omega t} \mathrm{d}t \tag{18}$$

of the autocorrelation of the motion

$$a(t) = \int_{-\infty}^{\infty} \mathrm{d}\mathbf{p}_B \mathrm{d}\mathbf{q}_B \int_{-\infty}^{\infty} \mathrm{d}\mathbf{p}_I \mathrm{d}\mathbf{q}_I < \Psi_1(0) \,|\, \Psi_1(t) > \tag{19}$$

of an initial Gaussian coherent state soliton $\psi_1(0)$ in system oscillator 1, where $\mathbf{p}_B$ and $\mathbf{q}_B$ are the momenta and positions of the bath oscillators, respectively, while $\mathbf{p}_I$ and $\mathbf{q}_I$ are the momenta and positions of the input oscillators, respectively. Note that this approach ignores the direct contribution to decoherence ensuing from the remaining system oscillators and the baths and hence provides an upper bound to the coherence lifetime. The quantum dynamics is determined using the Thawed-Gaussian approximation (*43, 44*) to provide the solution to the time-dependent Schrödinger equation, an approximation that is exact for the time-dependent effective harmonic potential provided by Eqn. 5. This method allows the quantum dynamics of the system to be determined using slightly augmented classical molecular mechanics methodologies. To ensure that coherence is not lost because of numerical issues associated with the trajectory solver, energy conservation to six decimal places is maintained over the ca. 1 μs time span of the trajectories. Some detailed examples of how coherence is determined from the dynamics is provided later in Fig. S10. To aid in the spanning the configuration space of the integrals in Eqn. 19, the frequencies, positions, and momenta of the bath and input modes are randomized after ca. every 50 ps of dynamics, this time being much larger than any coherence time found in our simulations. The bath modes are selected randomly at frequencies up to $2kT/\hbar$ while the input modes are selected only within the critical range of $\omega_1/2$ to $3(2\omega_0-\omega_1)/2$ for computational efficiency.

Numerical solutions to the Wu-Austin Hamiltonian dynamics in regions depicting strong condensates are difficult to obtain. Large values of the energy couplings α, β, and γ are required so that the condensate forms within a computationally feasible time frame, while excessive values of α or β lead to crossings of the transition state that define the physically meaningful region of the potential. Extreme source temperatures are demanded as the condensate must feed enormous energy into the lowest mode and the energy supply cannot falter; large source temperatures also allow γ, and hence α and β, to be minimized. The condensates reported display the expected dependence on the system parameters and can be formed using a variety of starting conditions.

E. Numerical Solutions to Fröhlich's equations over the whole range of the parameter space

Solutions to Fröhlich's equations obtained over a wide region of the parameter space are provided in Figs. S1-S8. The parameters used in these simulations are:

Figure	Temp[a]	Method	Dispersion	Z	χ/ϕ	χ_3/ϕ[c]
S1	Planck	numerical	linear	25	varied	0
S2	Planck	numerical	linear	100	varied	0
S3	Planck	numerical	linear	500	varied	0
S4	Planck	numerical	cosine	25	varied	0
S5	Planck	numerical	Gaussian	25	varied	0
S6	Classical	numerical	linear	25	varied	0
S7	Planck	approximate[b]	-	-	varied	0
S8	Planck	numerical	linear	25	0.02	varied

a: At thermal equilibrium either a Planck semiclassical ensemble with $n_i^T = \left(e^{\hbar\omega_i/kT} - 1\right)^{-1}$ or else a classical ensemble embodying equipartition of energy with $n_i^T = kT/\hbar\omega_i$

b: Using the approximate expressions: $N \approx N^{\chi=0} + Z\frac{s}{\varphi}n_1^T$ and $\frac{T_S}{T} = 1 + \frac{s}{\phi}e^{-\hbar\omega_0/2kT}$

c: See Supporting Information Section C.

Each figure shows results from a complete 4-dimensional grid evaluated at:

- s/ϕ = 0, 0.010, 0.028, 0.077, 0.22, 0.76, 1.67, 4.64, 12.9, 35.9, and 100;
- χ/ϕ = 0, 0.00010, 0.00028, 0.00077, 0.0022, 0.0060, 0.046, 0.13, 0.36, and 1;
- $\hbar\omega_0/kT$ = 0.010, 0.022, 0.046, 0.10, 0.22, 0.46, 1.0, 2.2, 4.6, 10.0, with some results also included for $\hbar\omega_0/kT = 10^{-3}$, 10^{-4}, and 10^{-5} ; and
- ω_1/ω_0 = 0.04, 0.12, 0.20, 0.28, 0.36, 0.44, 0.52, 0.60, 0.68, 0.76, 0.84.0.92.

On each figure, a grid of plots of the form shown to the right is provided, with each plot corresponding to the indicated values of $\hbar\omega_0/kT$ and ω_1/ω_0. Each plot presents the condensate property evaluated at different values of s/ϕ and χ/ϕ, as indicated to the right.

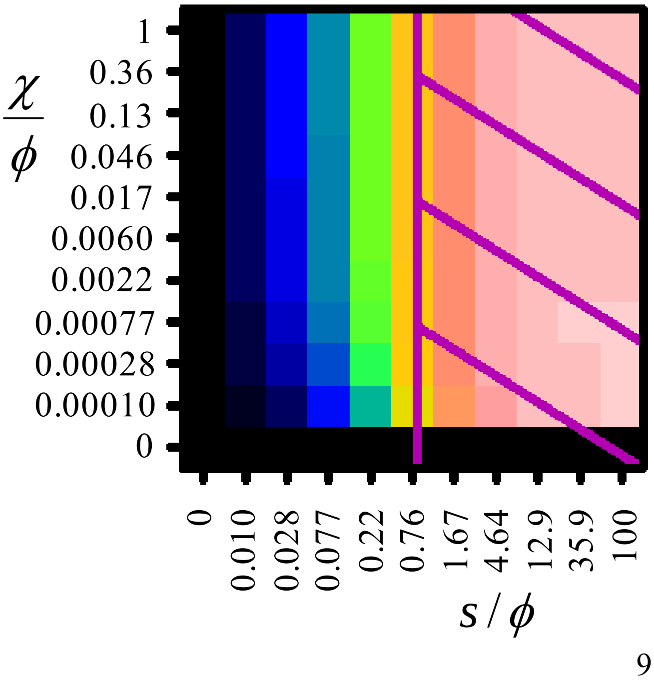

Each figure also consists of parts A-G (on separate pages) giving the following properties of the condensate:

Part	Property
A	$\log \frac{T_S}{T}$
B	$\log \frac{N}{Z}$
C	$\log \frac{N - N^{\chi=0}}{Z}$
D	$\log \frac{n_1}{Z}$
E	$\eta = \frac{n_1 - n_1^{\chi=0}}{N}$
F	$\frac{n_1 \omega_1}{\sum_{i=1}^{Z} n_i \omega_i}$
G	$\frac{n_1}{n_1^{\chi=0}}$

Part A shows the effective temperature of the system modes estimated from the total system-mode energy using Eqn. 10. It is this property that is shown hatched in Figs. 2 and 3 of the main text. The system temperature can exceed 30000 K for a room temperature bath.

Part B shows the average number of vibrational quanta per oscillator. This can be quite low for systems at low vibrational temperature but exceeds a million for some of the condensates considered. Fröhlich condensation thus indeed leads to large amounts of vibrational energy in the system.

Part C shows the number of quanta per oscillator found in the system above that produced at $\chi = 0$. High excitation rates and low relaxation rates to the bath can lead to very high values of N in a way that does not involve condensation, so Part C better represents the condensate than does Part B. Use of the Wu-Austin Hamiltonian does not lead to results for this quantity, however, and it may be of less general utility.

Part D shows the number of quanta in the lowest-frequency mode, normalized by the number of oscillators. This quantity grows large as the condensate forms and so this property shows a different aspect of the condensation process than that shown in Parts B and C.

Part E shows the condensation index η that is reported in the main text in Figure 2. It shows approximately how many of the excess quanta associated with condensation reside in the lowest mode and is a good single descriptor of the condensation process. Strong condensates have indices exceeding 0.8, with 0.9 being desirable.

Part F shows another descriptor of the condensation, the fraction of the total vibrational energy present in mode 1. When the condensate forms this is high, but a large amount of vibrational energy is an additional requirement.

Part G enhances a property of the condensation when it is weakly established, the ratio of number of vibrational energy present in mode 1 to that obtained at $\chi = 0$ (ie., when there is a steady state energy flow from source to bath but no condensation). This ratio can reach large values but all those above 2 are represented as white so as to emphasise the weak condensation regime. Extracts of these figures are presented in the main text in Figure 3.

Fig. S1A: LINEAR Z= 25 log T_S/T

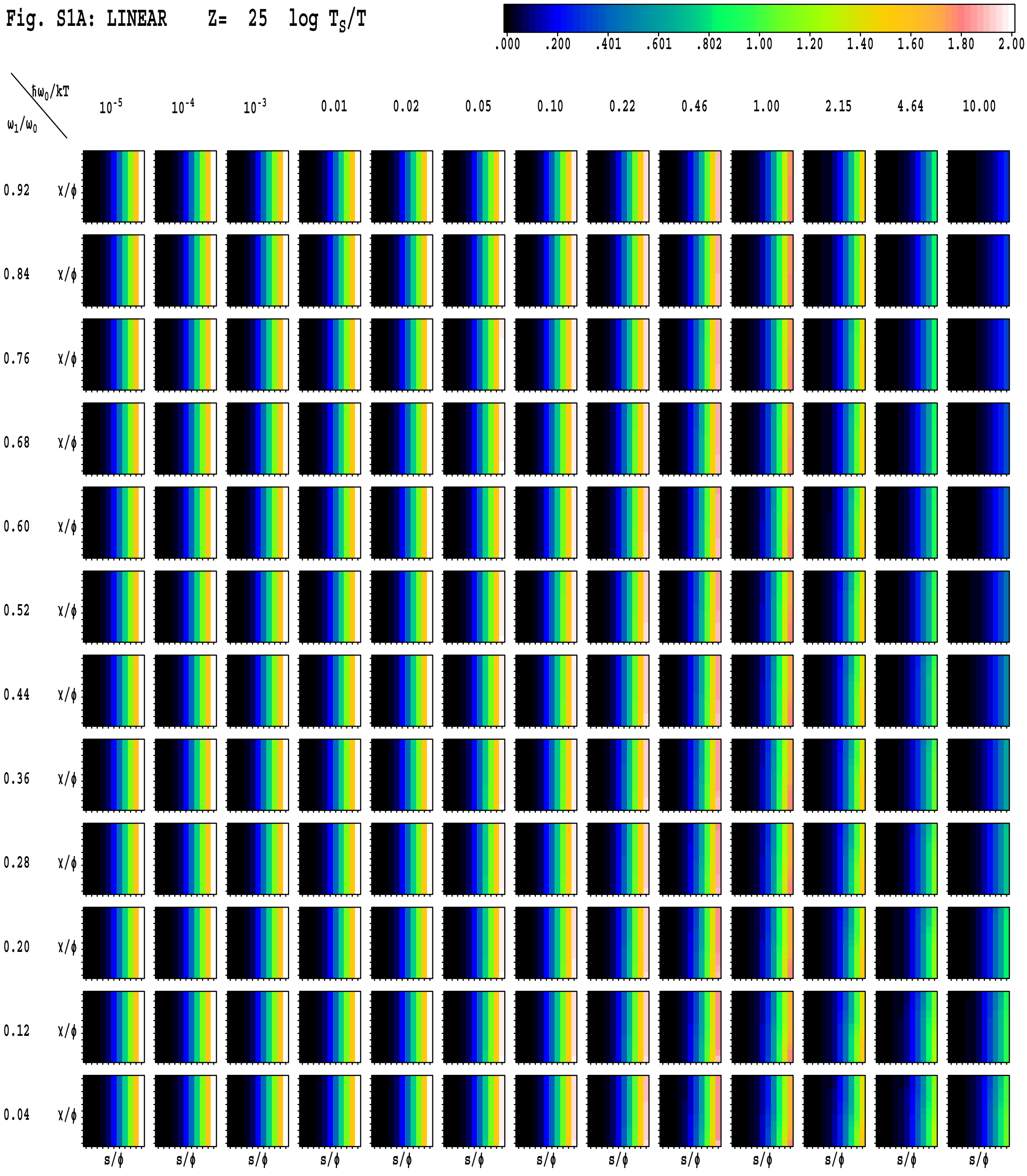

Fig. S1B: LINEAR Z= 25 log N/z

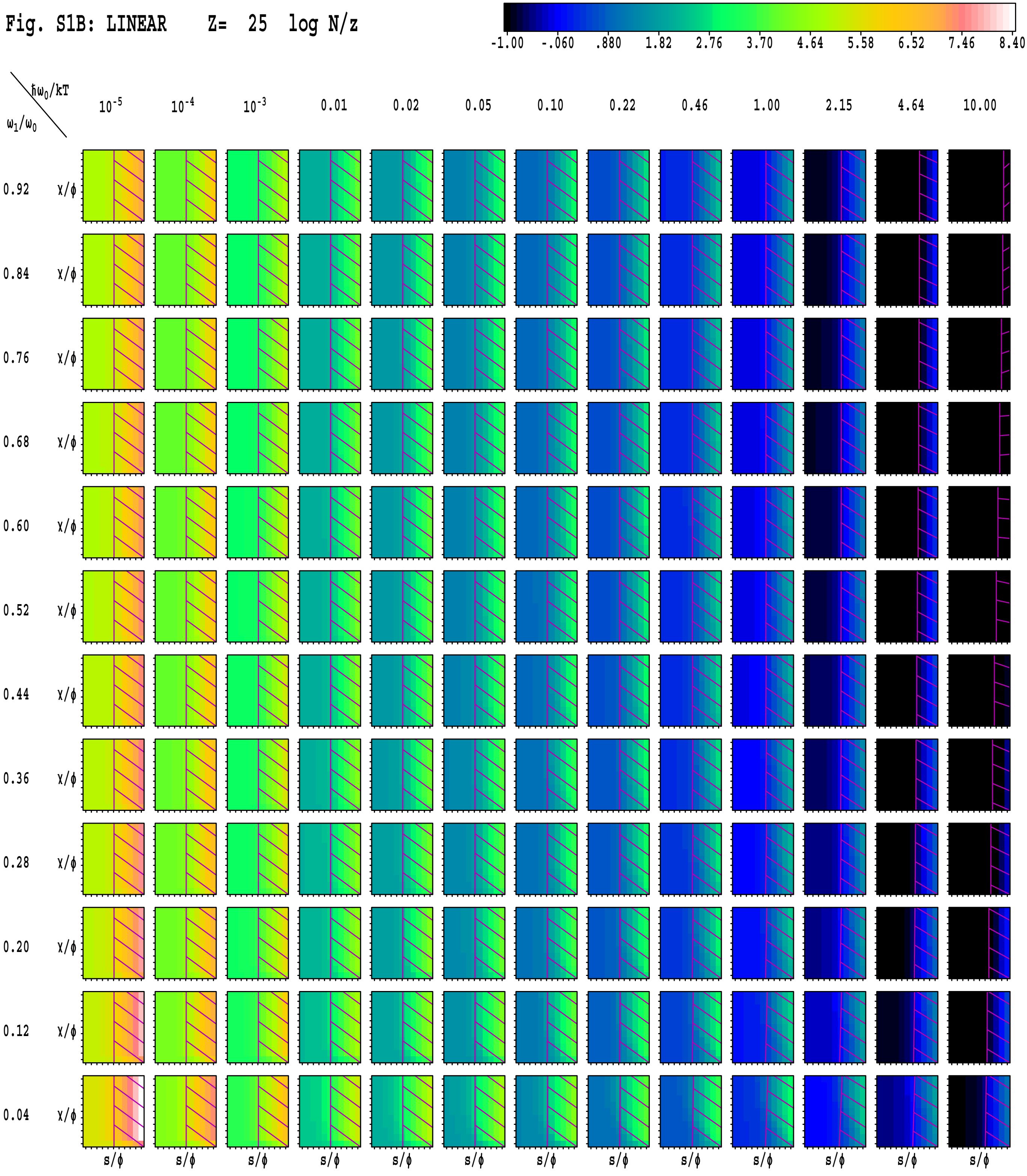

Fig. S1C: LINEAR Z= 25 log $(N-N^{\chi=0})/z$

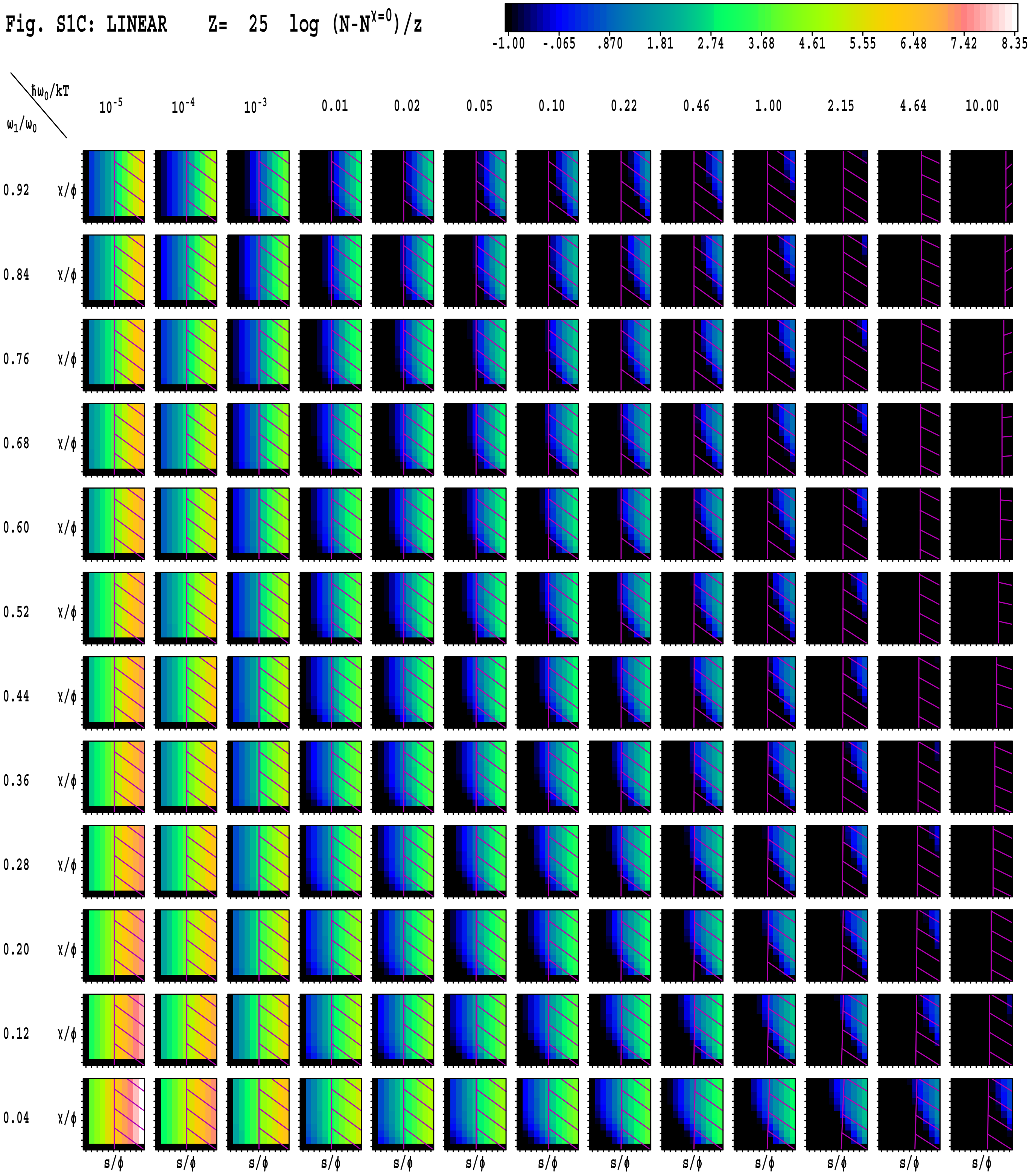

Fig. S1D: LINEAR Z= 25 n_1/N

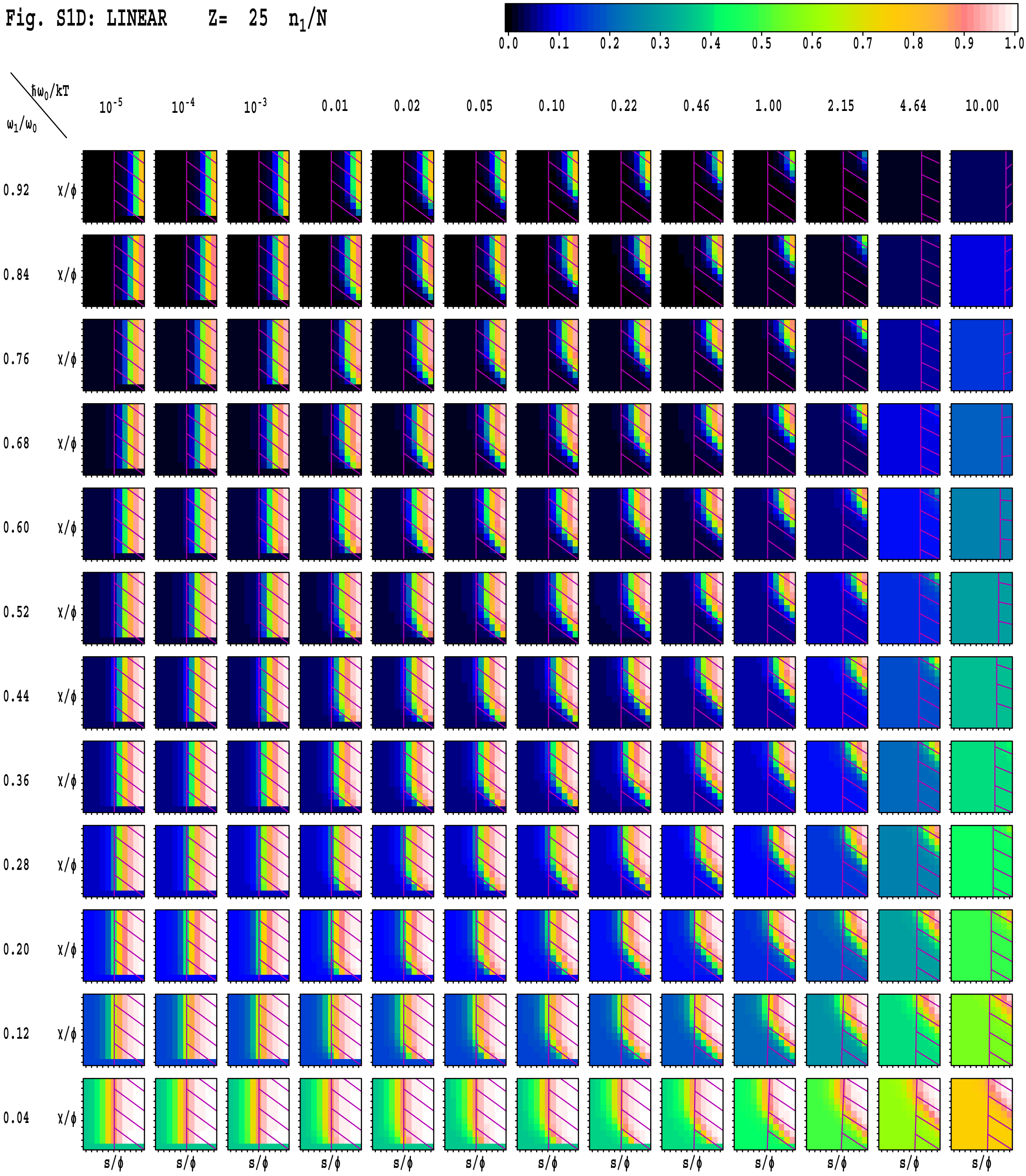

Fig. S1E: LINEAR Z= 25 $\eta=(n_1-n_1^{\chi=0})/N$

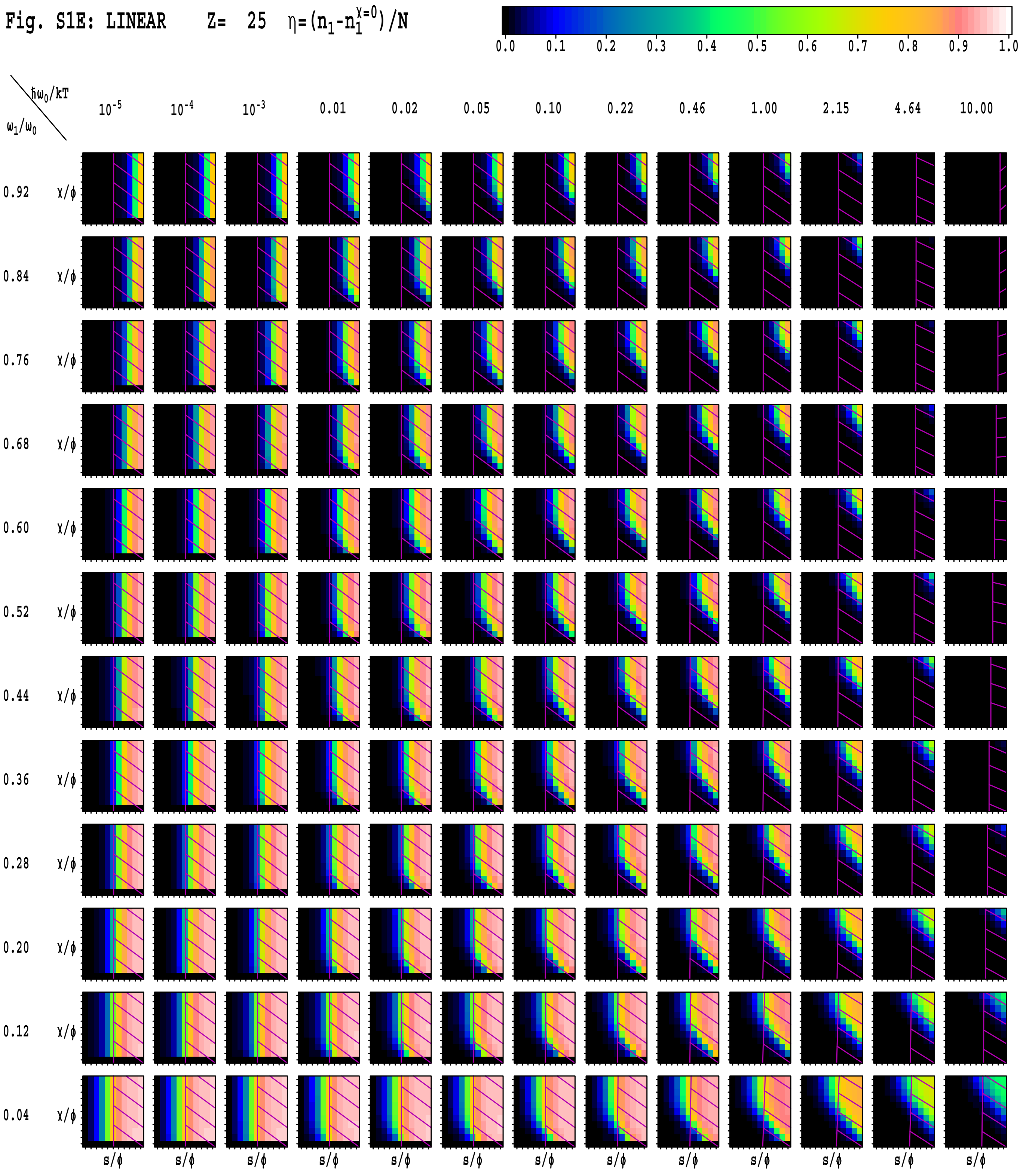

Fig. S1F: LINEAR Z= 25 $n_1\omega_1/\Sigma n_i\omega_i$

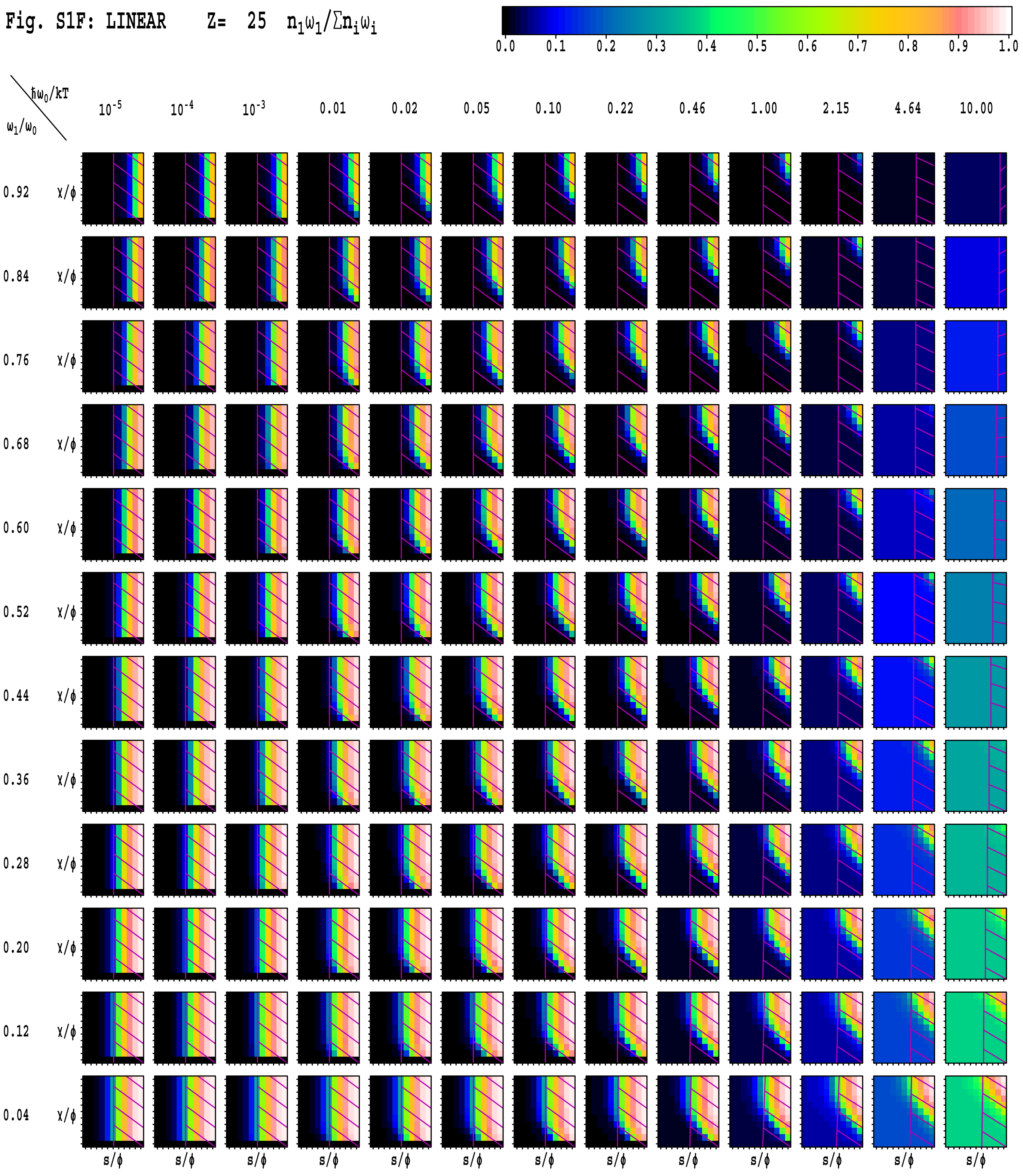

Fig. S1G: LINEAR Z= 25 $n_1/n_1^{\chi=0}$

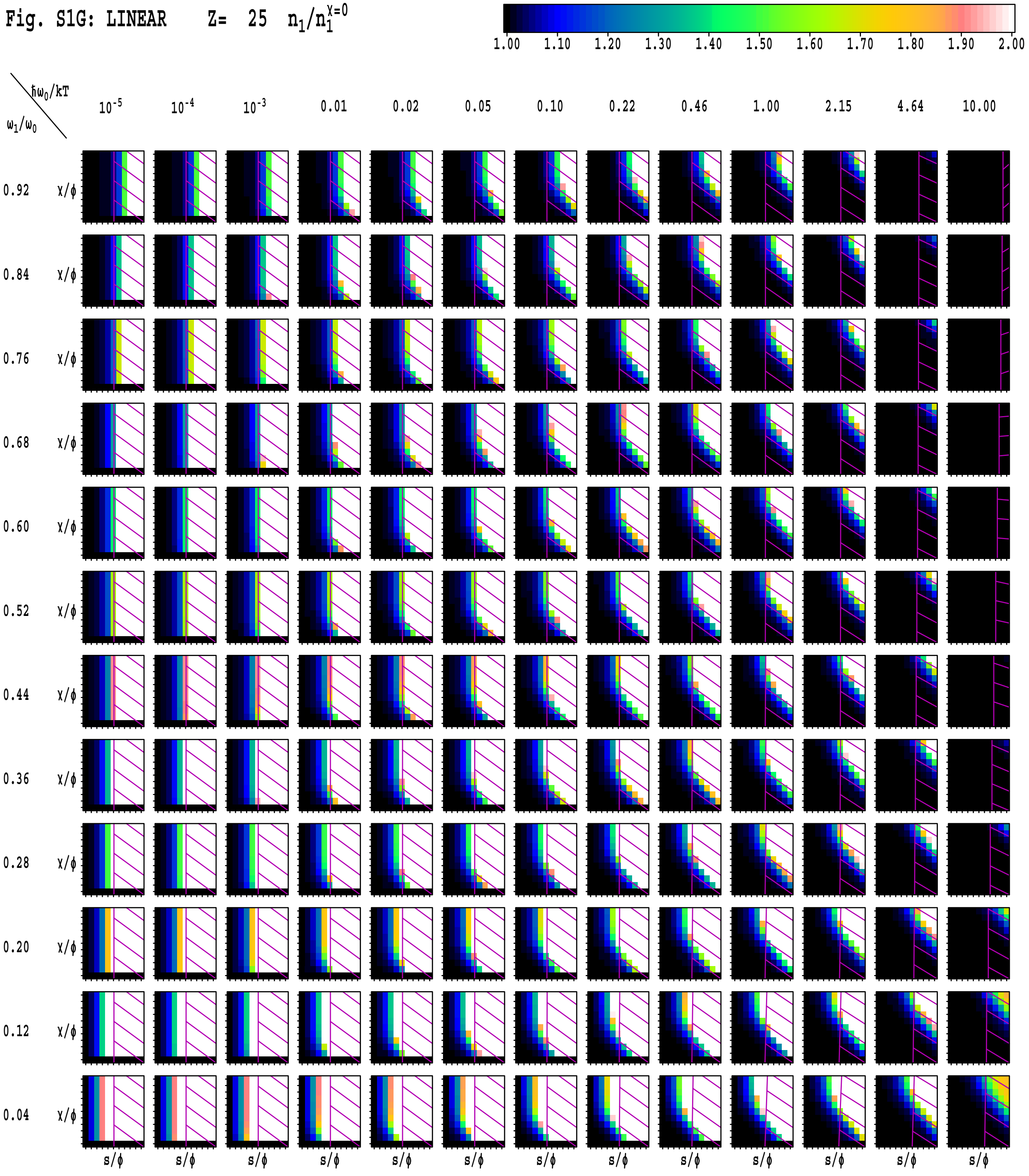

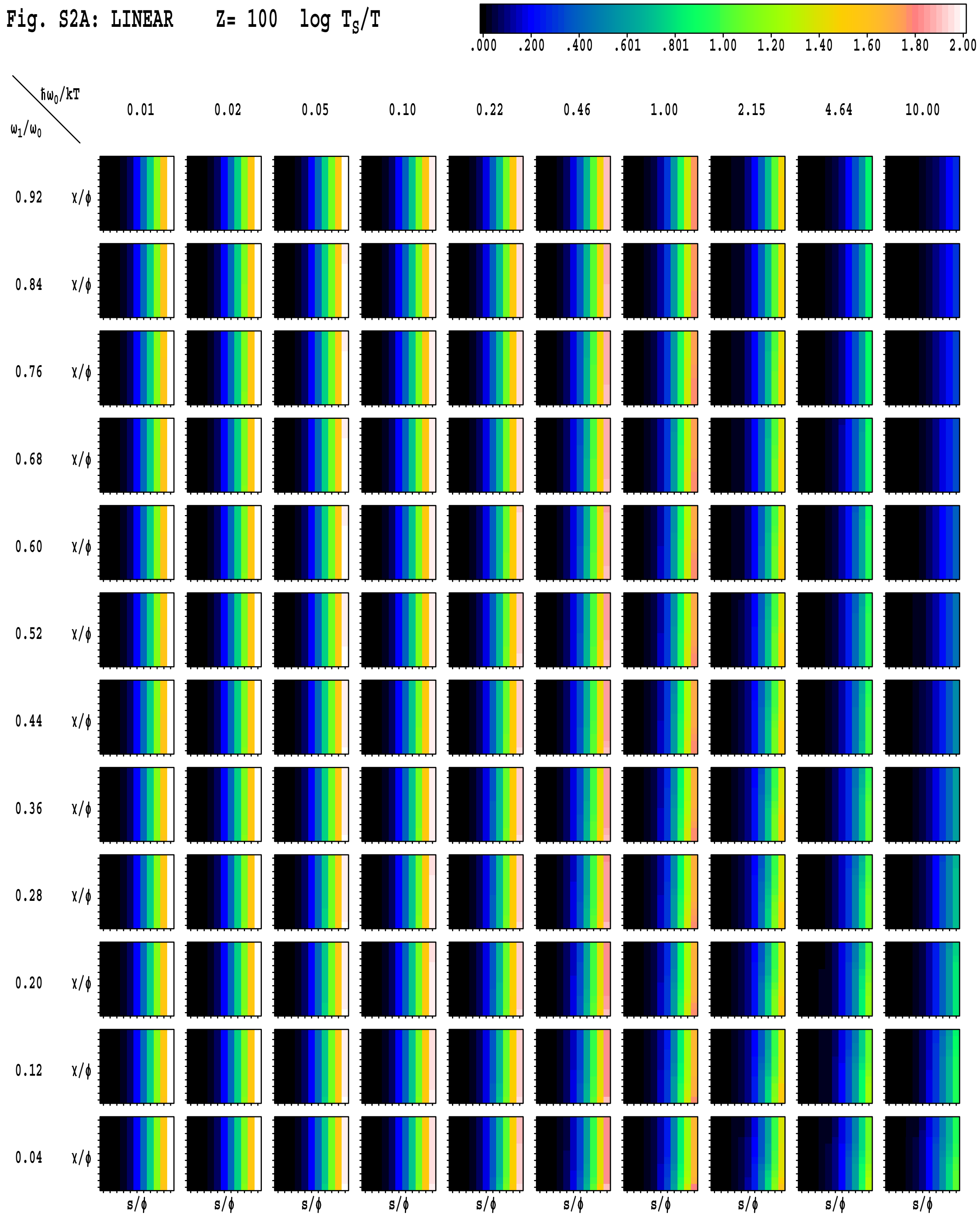

Fig. S2A: LINEAR Z= 100 log T_S/T

Fig. S2B: LINEAR Z= 100 log N/z

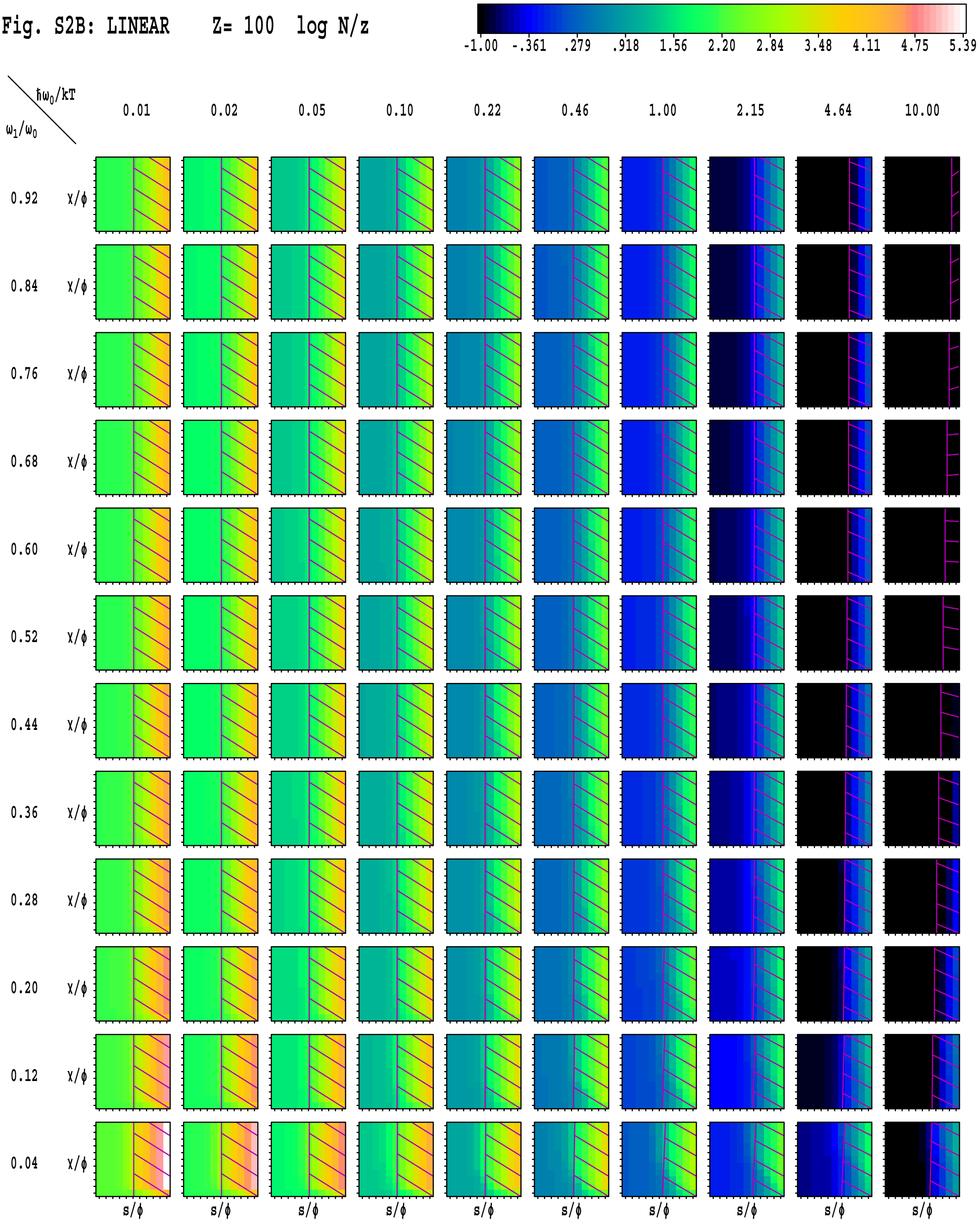

Fig. S2C: LINEAR Z= 100 log $(N-N^{\chi=0})/z$

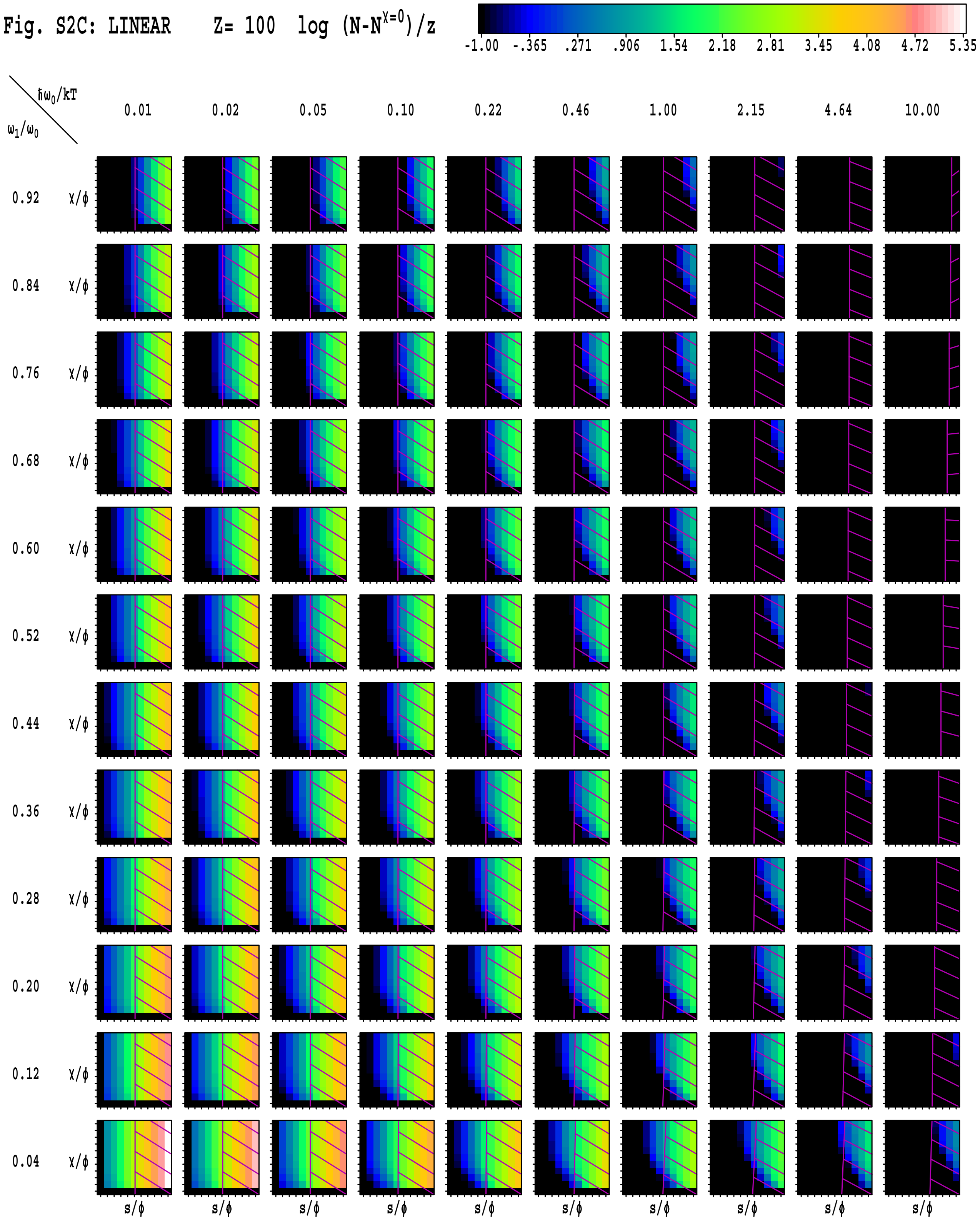

Fig. S2D: LINEAR Z= 100 n_1/N

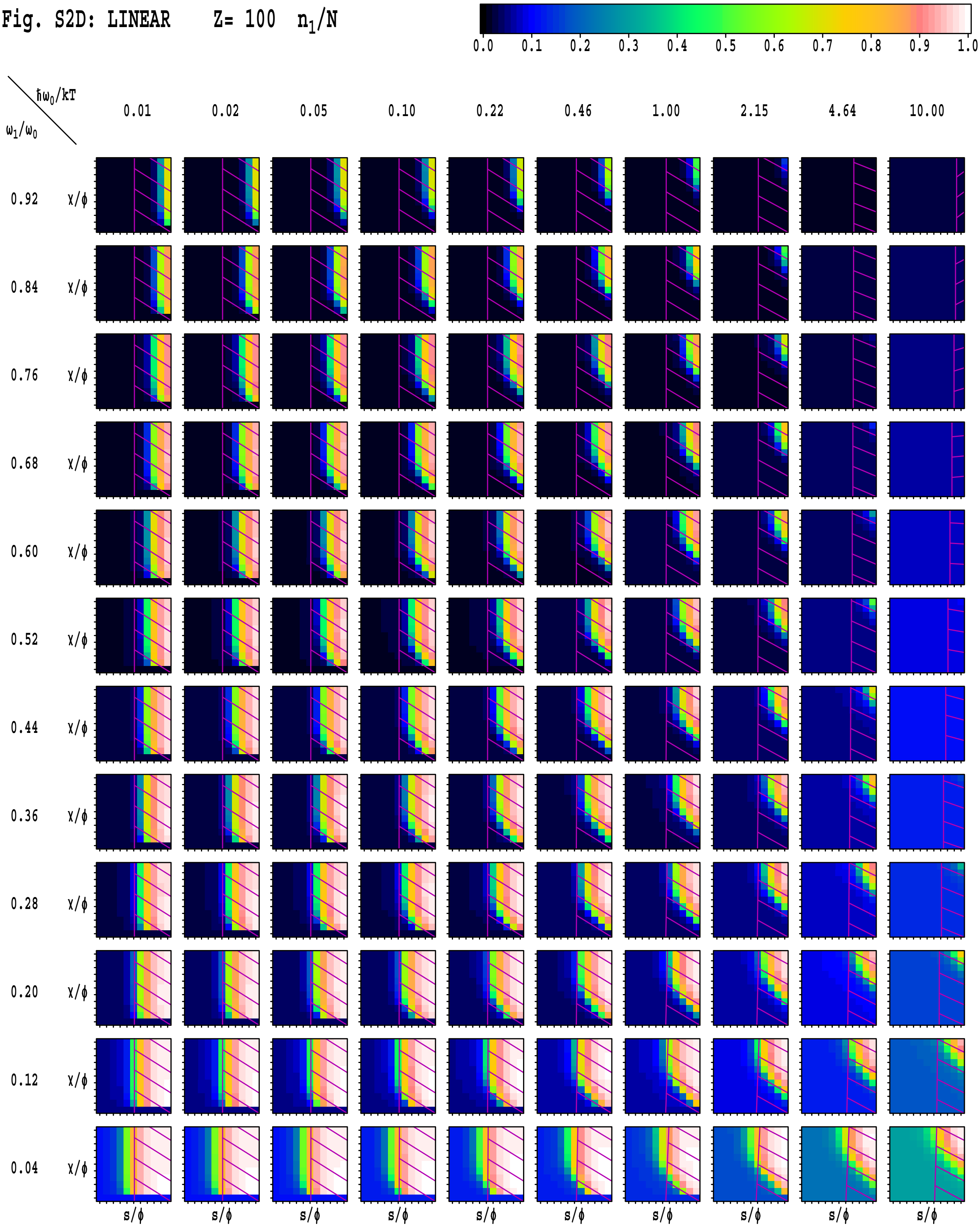

Fig. S2E: LINEAR Z= 100 $\eta=(n_1-n_1^{\chi=0})/N$

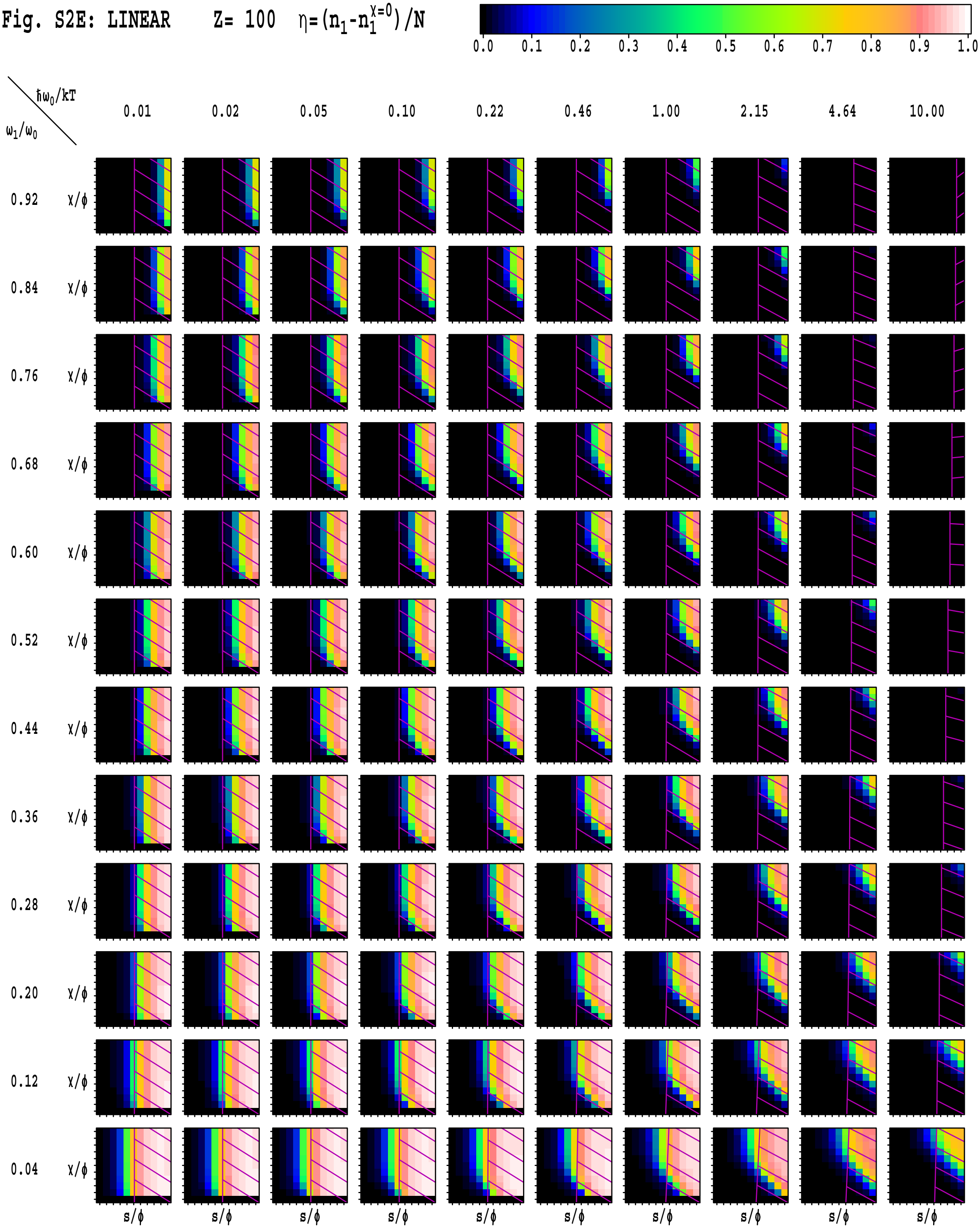

Fig. S2F: LINEAR Z= 100 $n_1\omega_1/\sum n_i\omega_i$

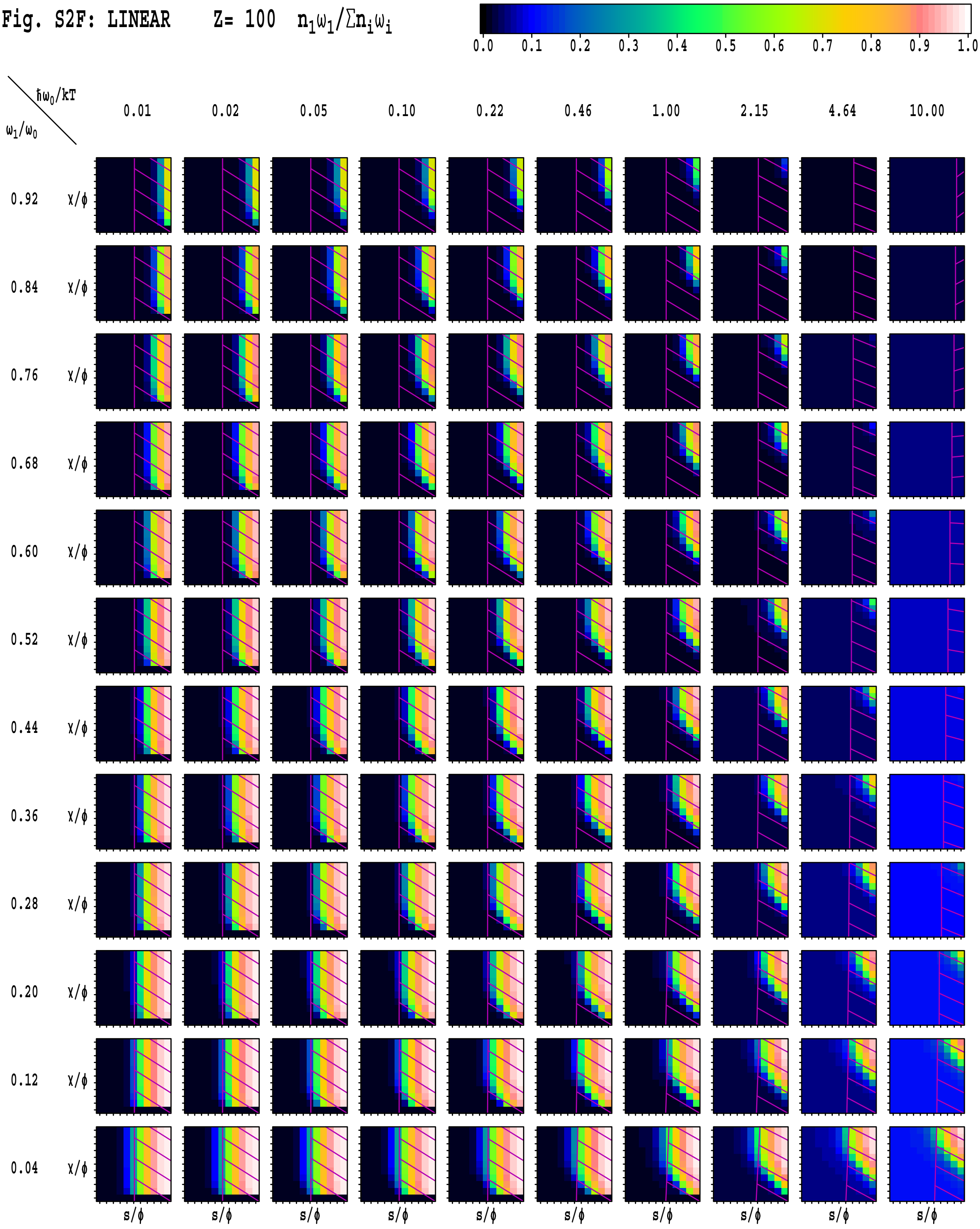

Fig. S2G: LINEAR Z= 100 $n_1/n_1^{\chi=0}$

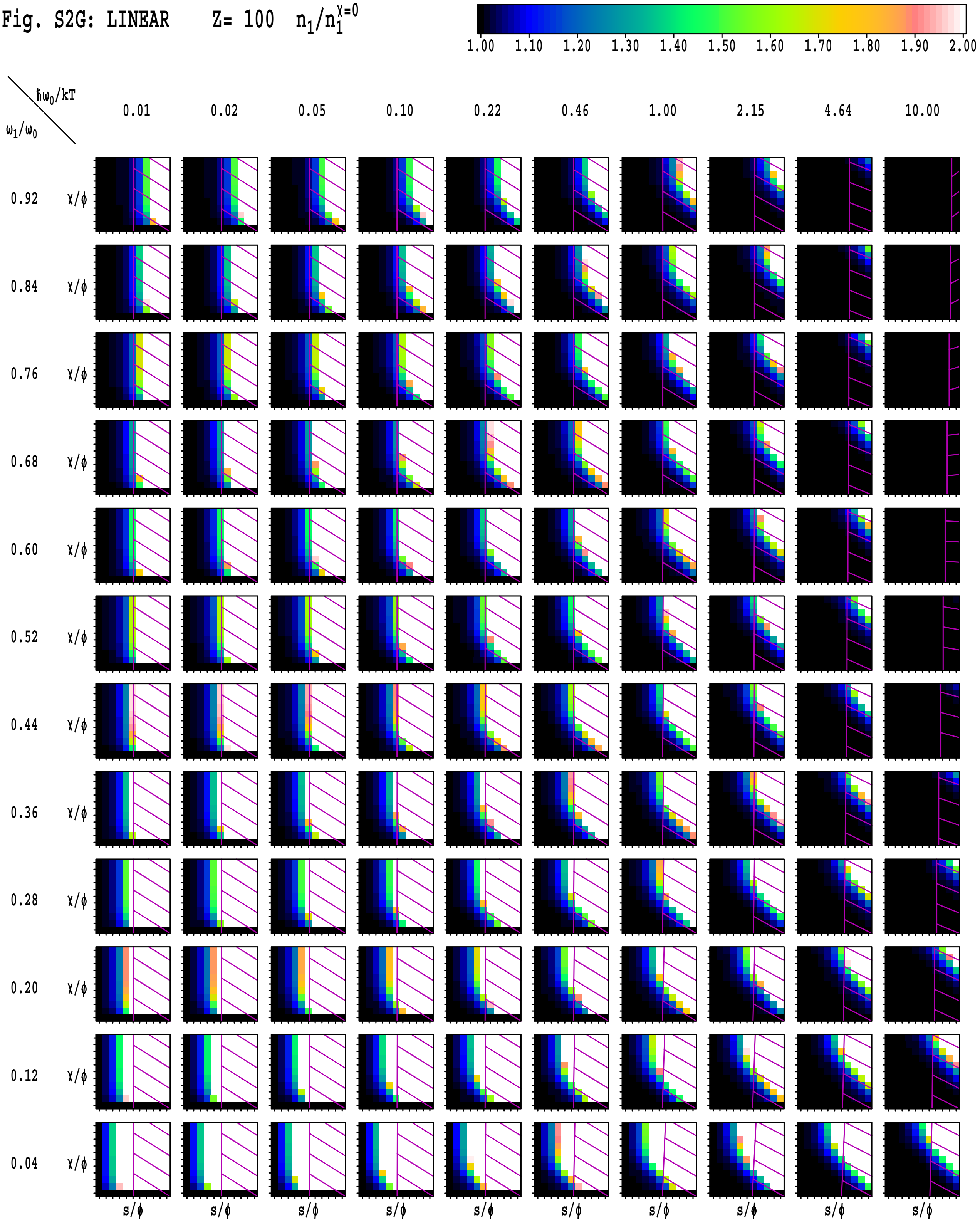

Fig. S3A: LINEAR Z= 500 log T_S/T

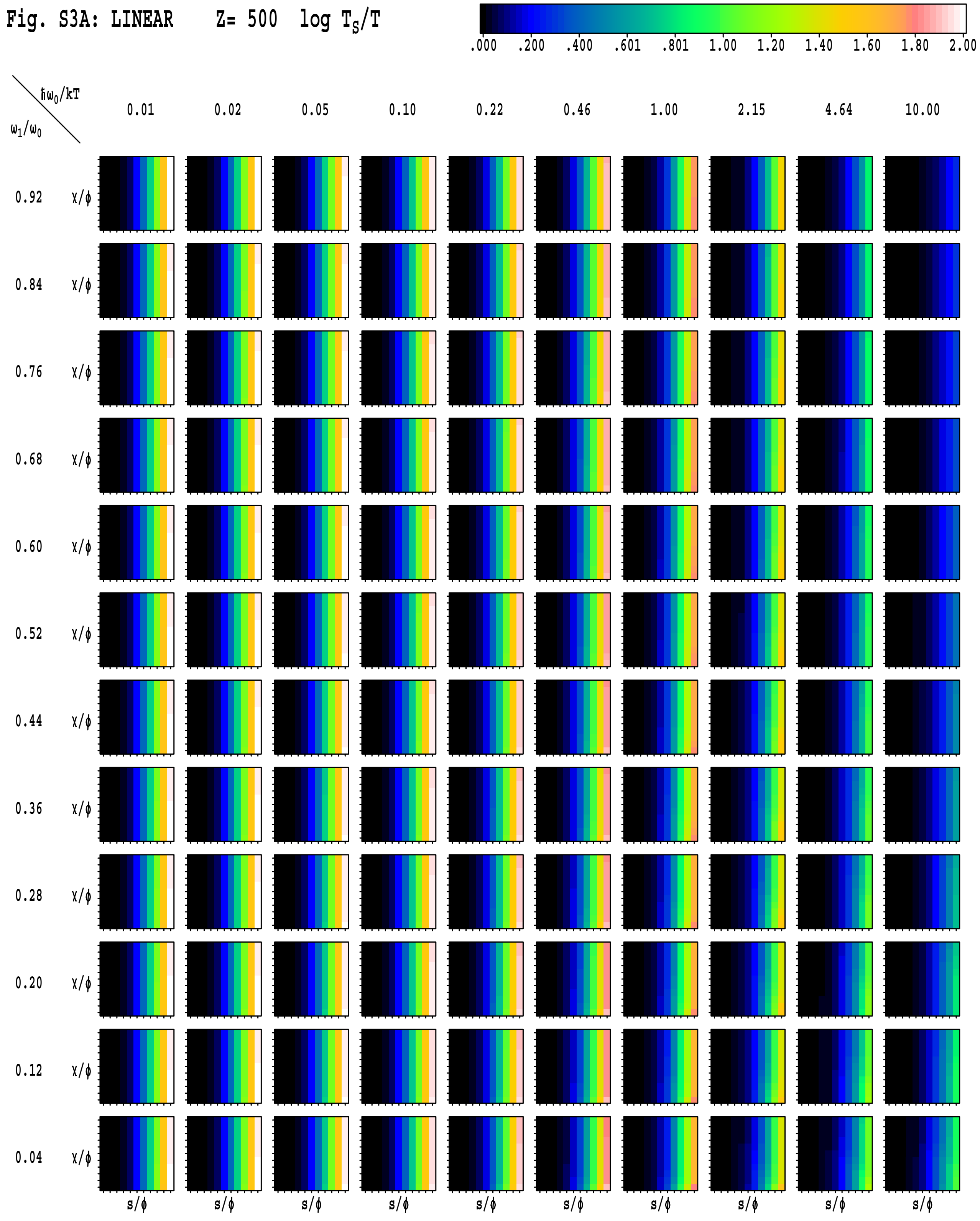

Fig. S3B: LINEAR Z= 500 log N/z

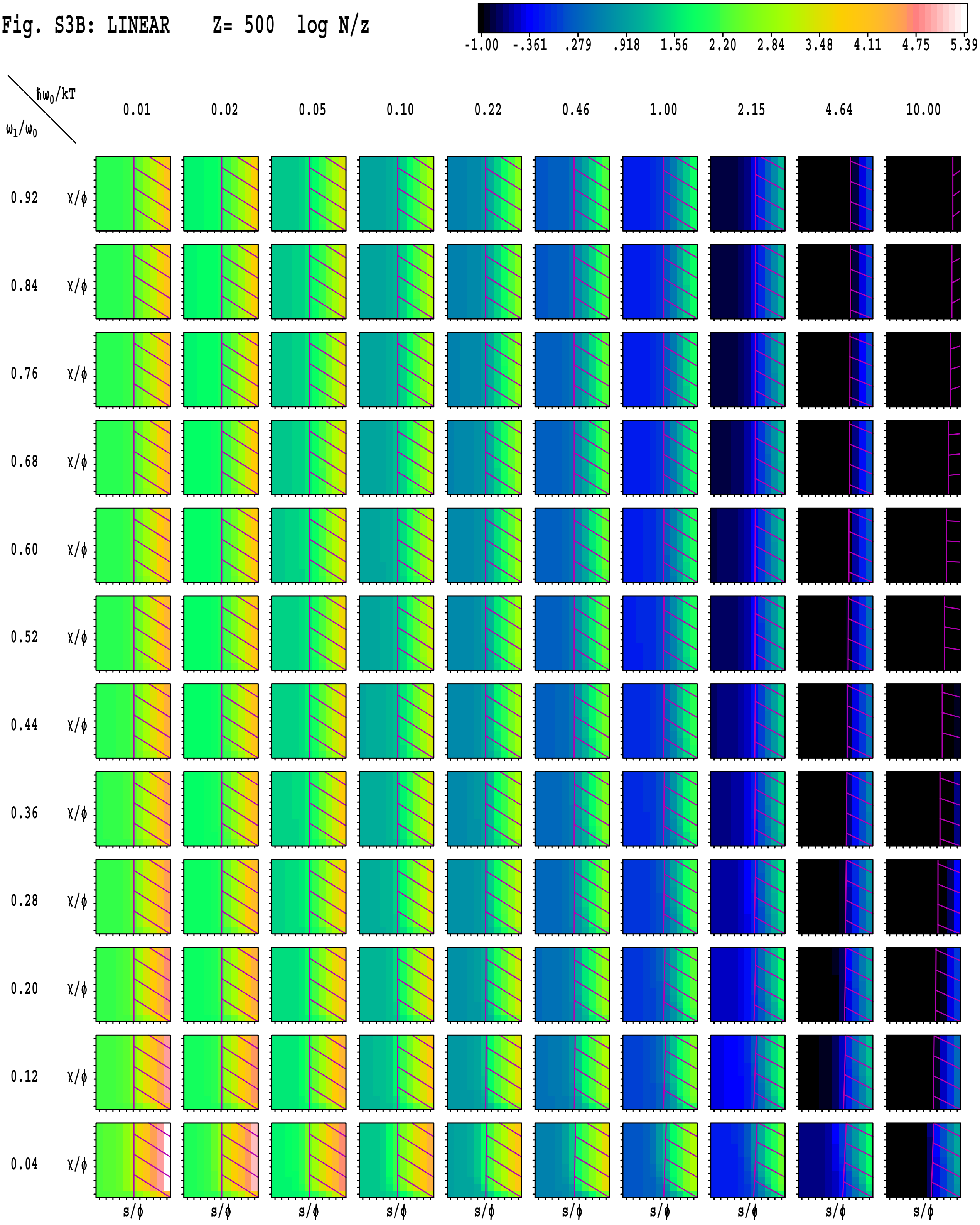

Fig. S3C: LINEAR Z= 500 log $(N-N^{\chi=0})/z$

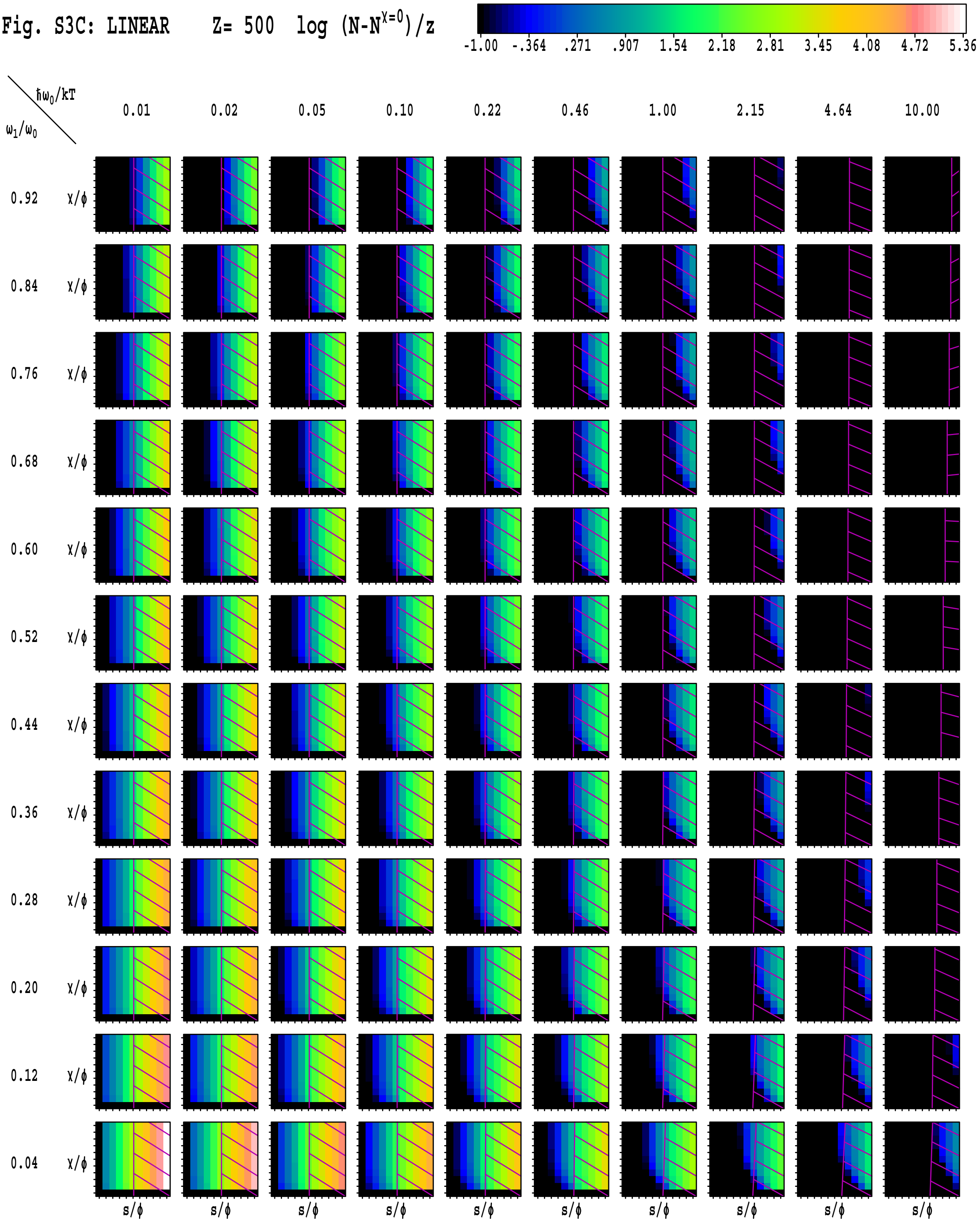

Fig. S3D: LINEAR Z= 500 n_1/N

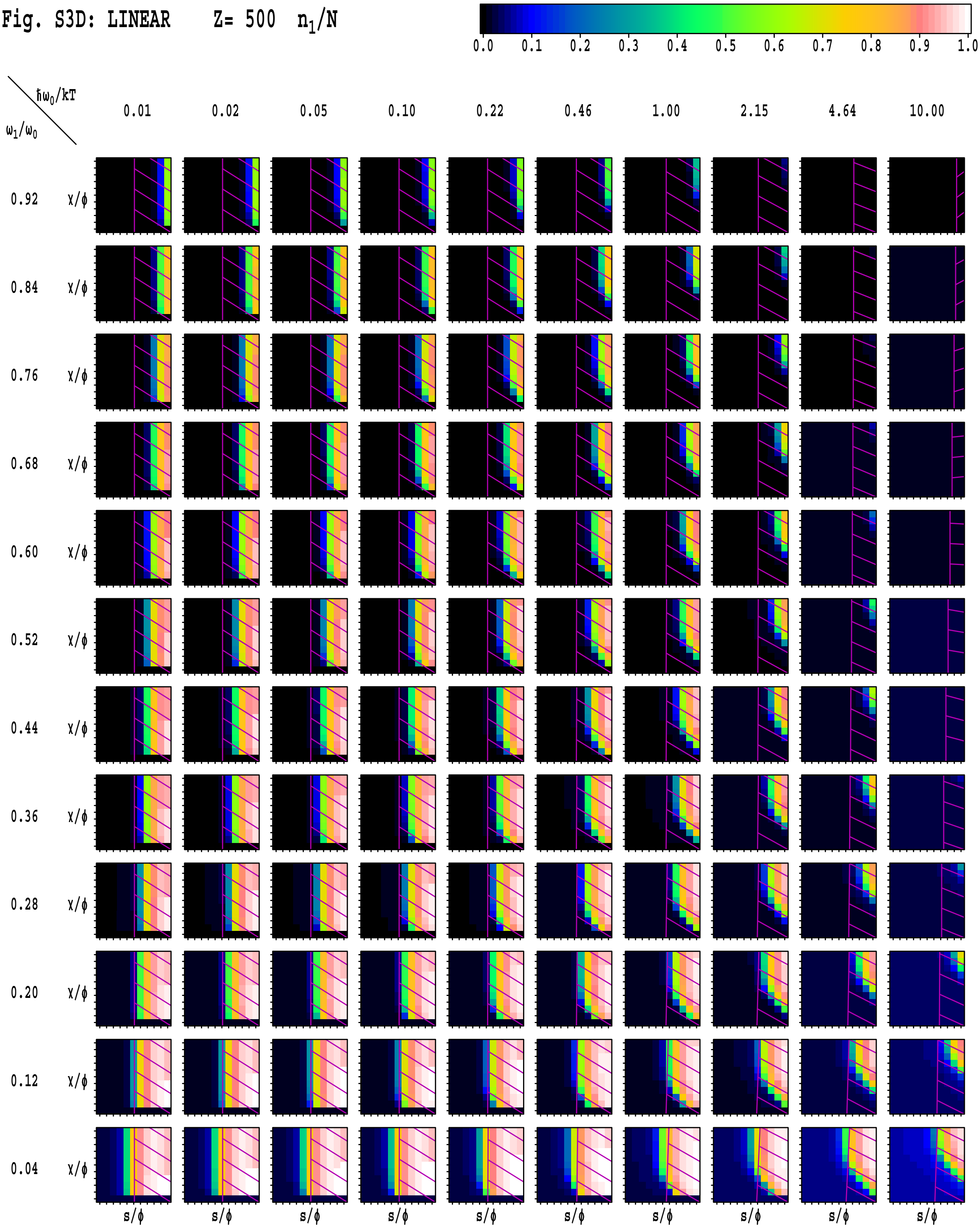

Fig. S3E: LINEAR Z= 500 $\eta=(n_1-n_1^{\chi=0})/N$

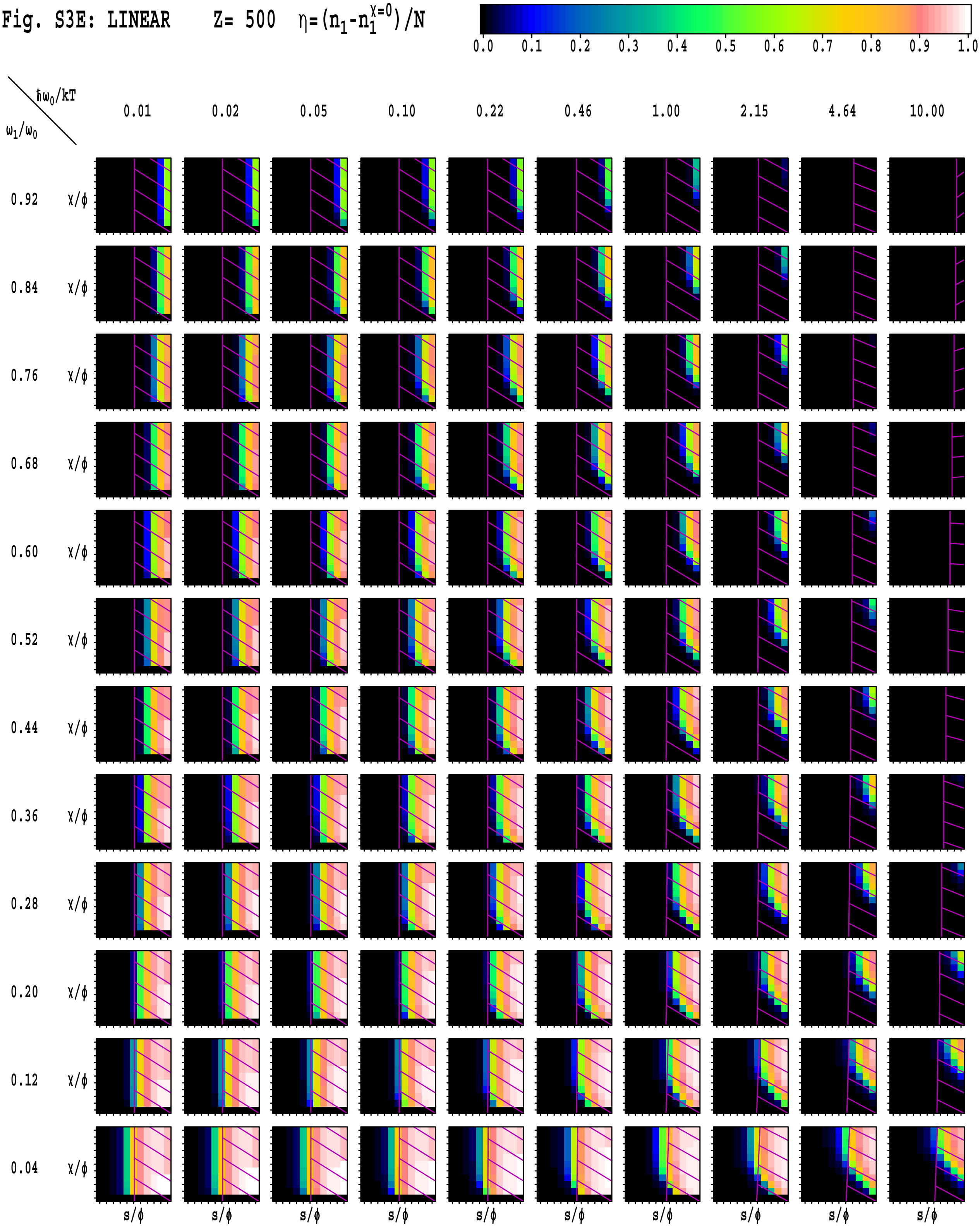

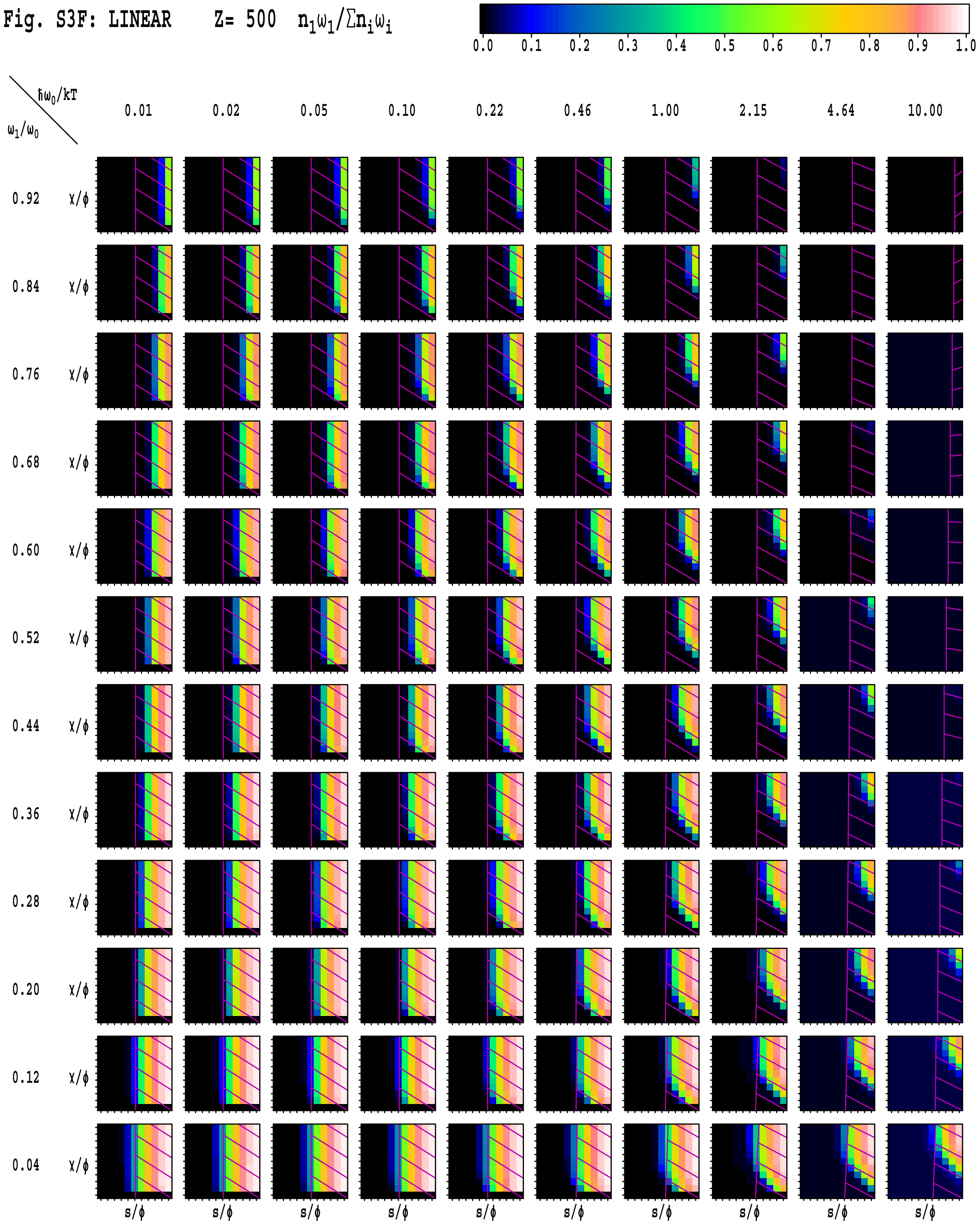

Fig. S3F: LINEAR Z= 500 $n_1\omega_1/\Sigma n_i\omega_i$

Fig. S3G: LINEAR Z= 500 $n_1/n_1^{\chi=0}$

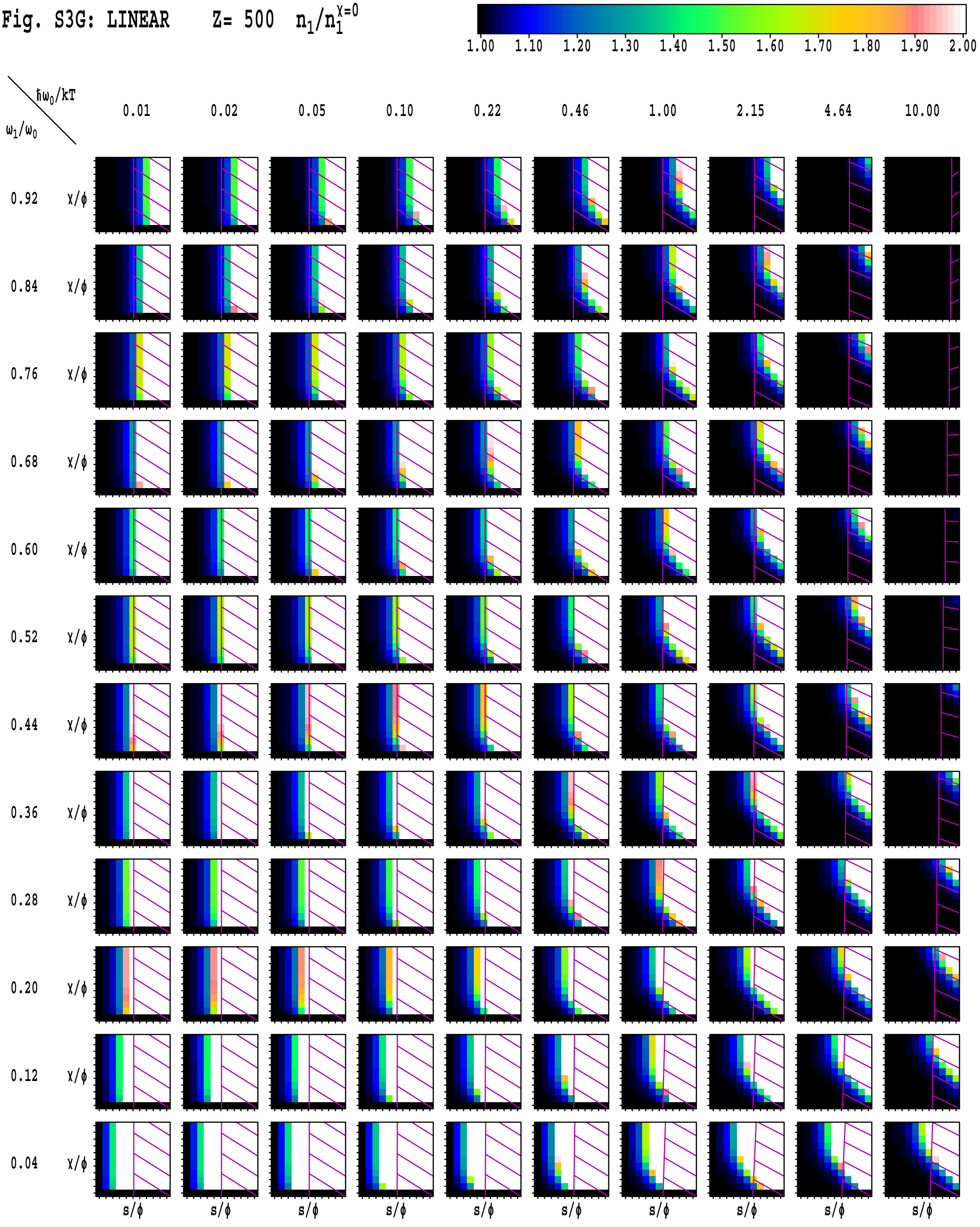

Fig. S4A: COSINE Z= 25 log T_S/T

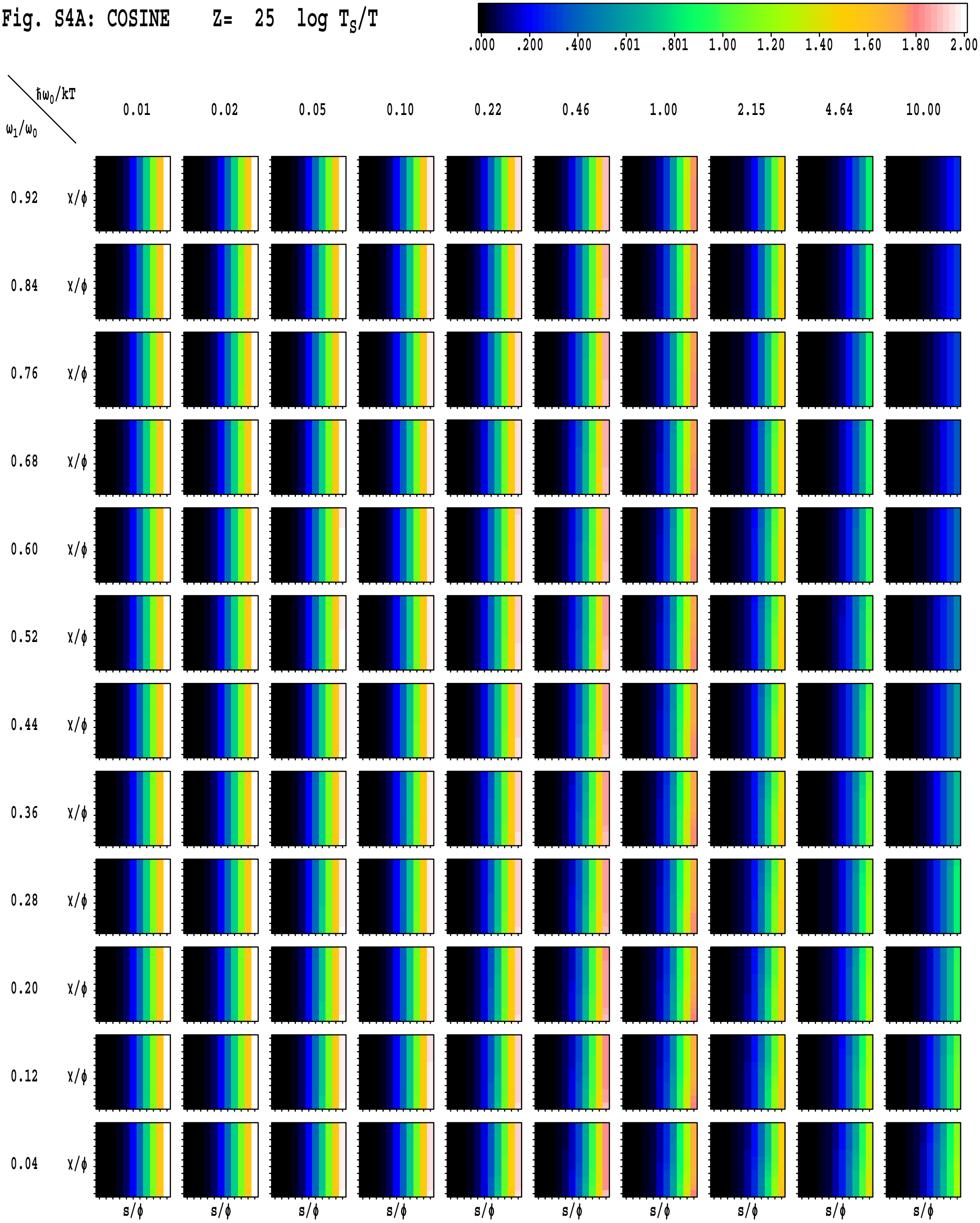

Fig. S4B: COSINE Z= 25 log N/z

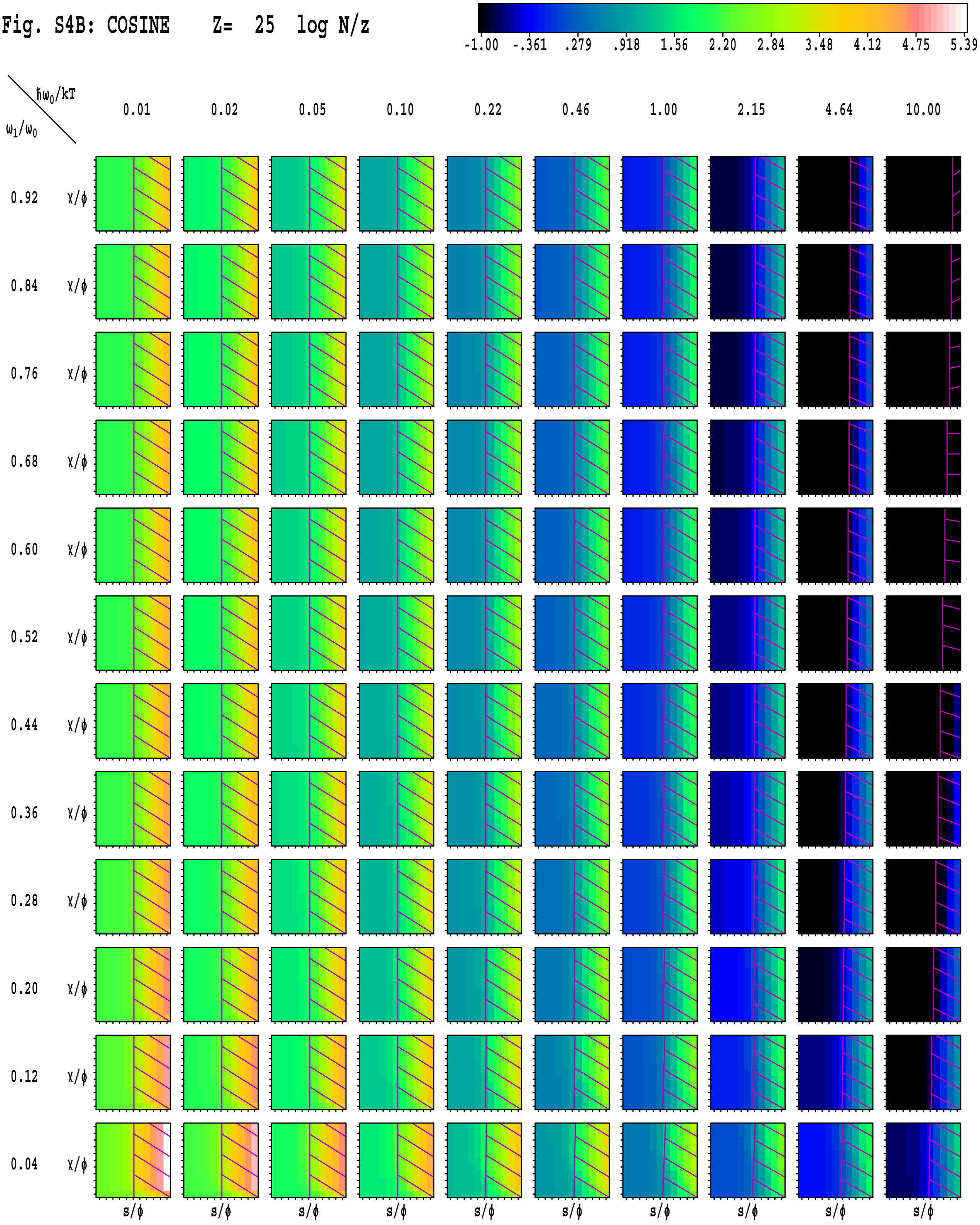

Fig. S4C: COSINE Z= 25 log $(N-N^{\chi=0})/z$

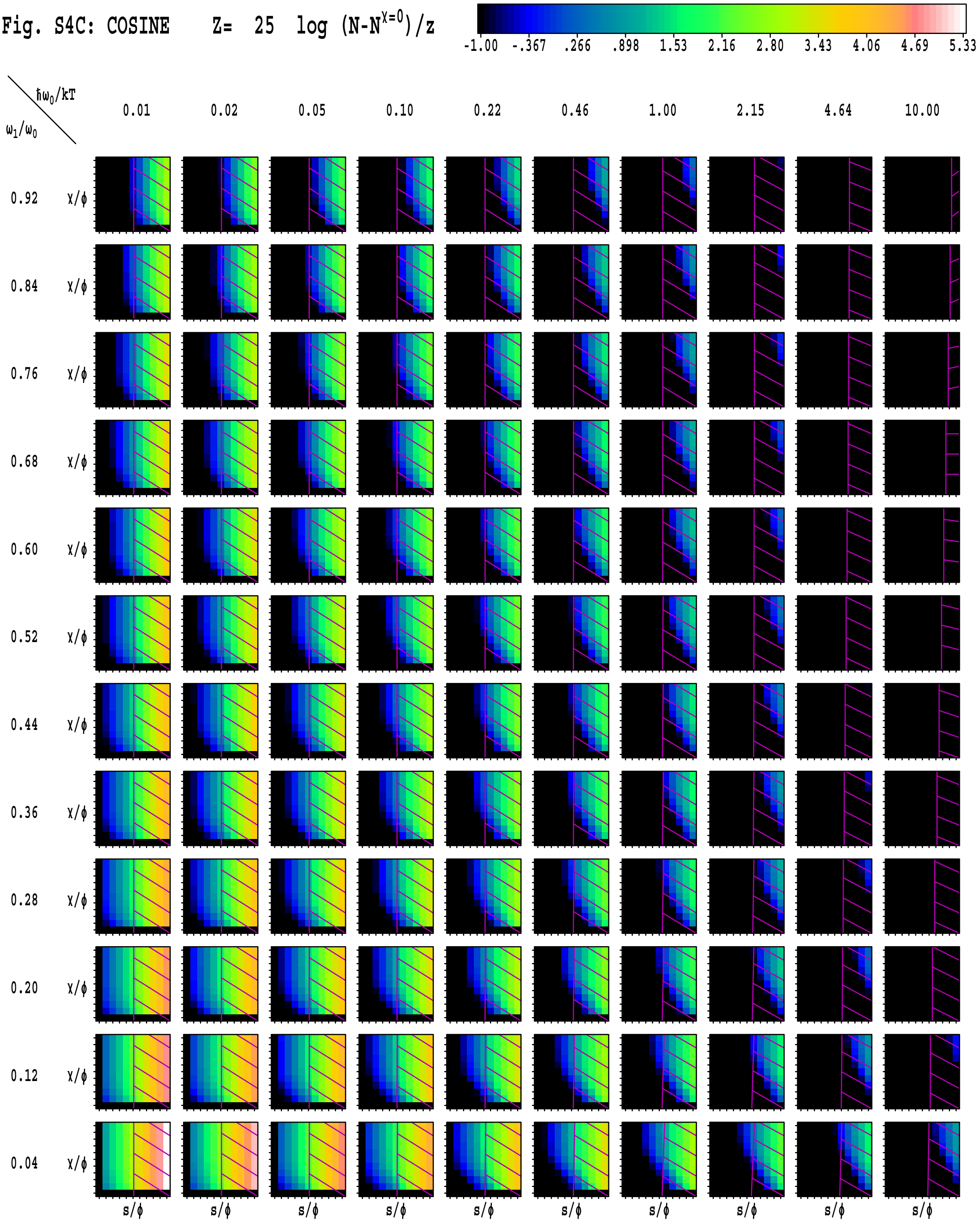

Fig. S4D: COSINE Z= 25 n_1/N

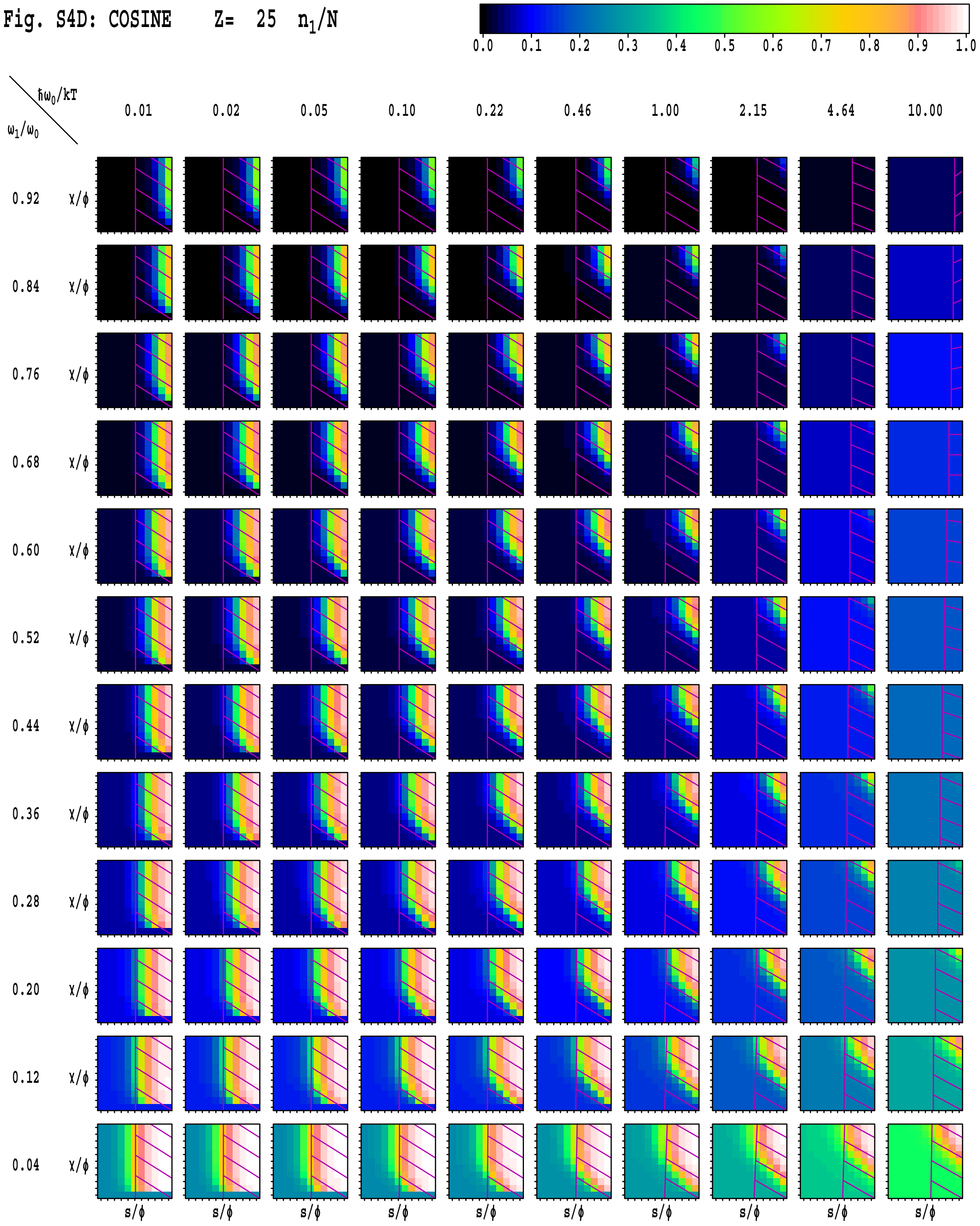

Fig. S4E: COSINE Z= 25 $\eta=(n_1-n_1^{\chi=0})/N$

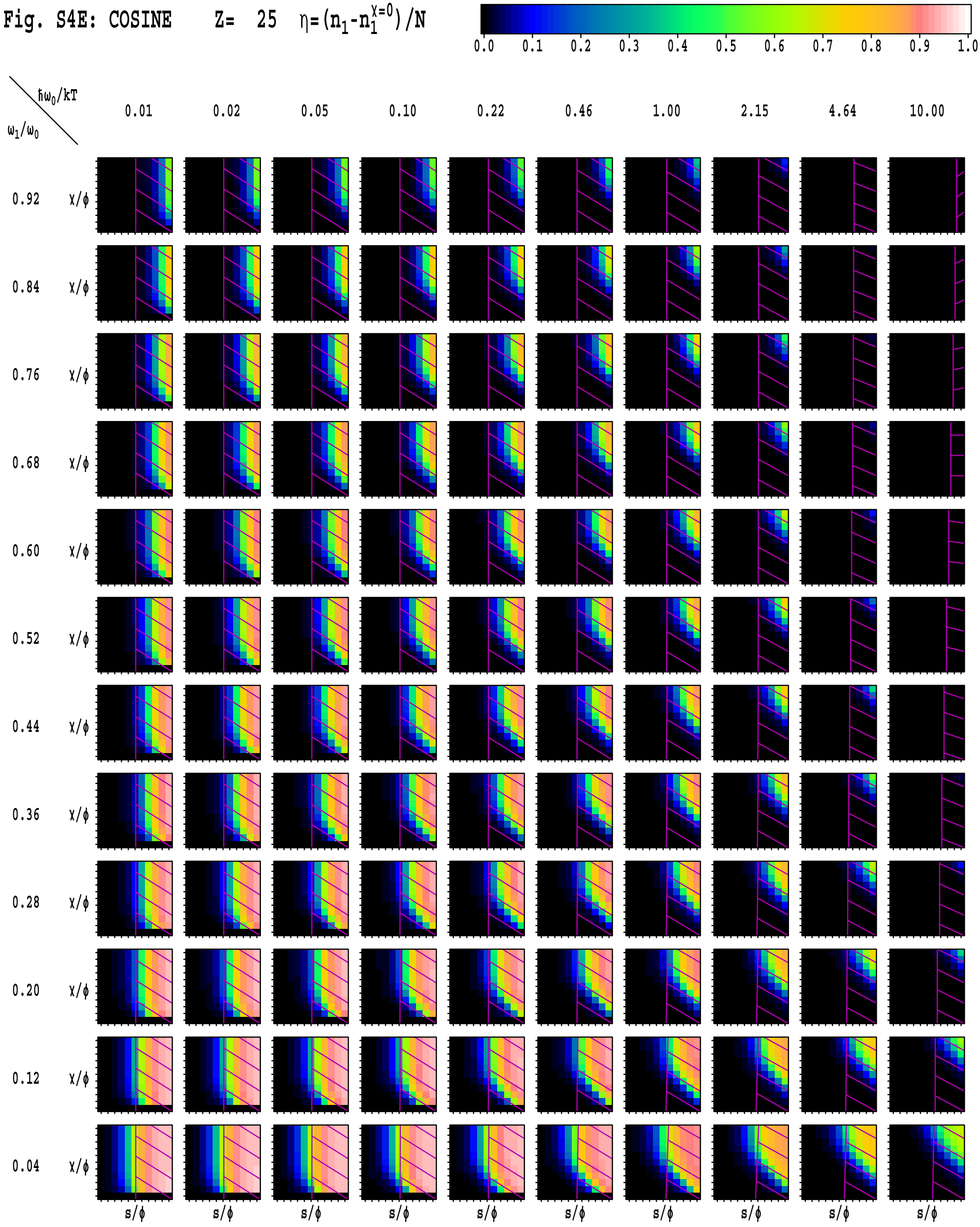

Fig. S4F: COSINE Z= 25 $n_1\omega_1/\sum n_i\omega_i$

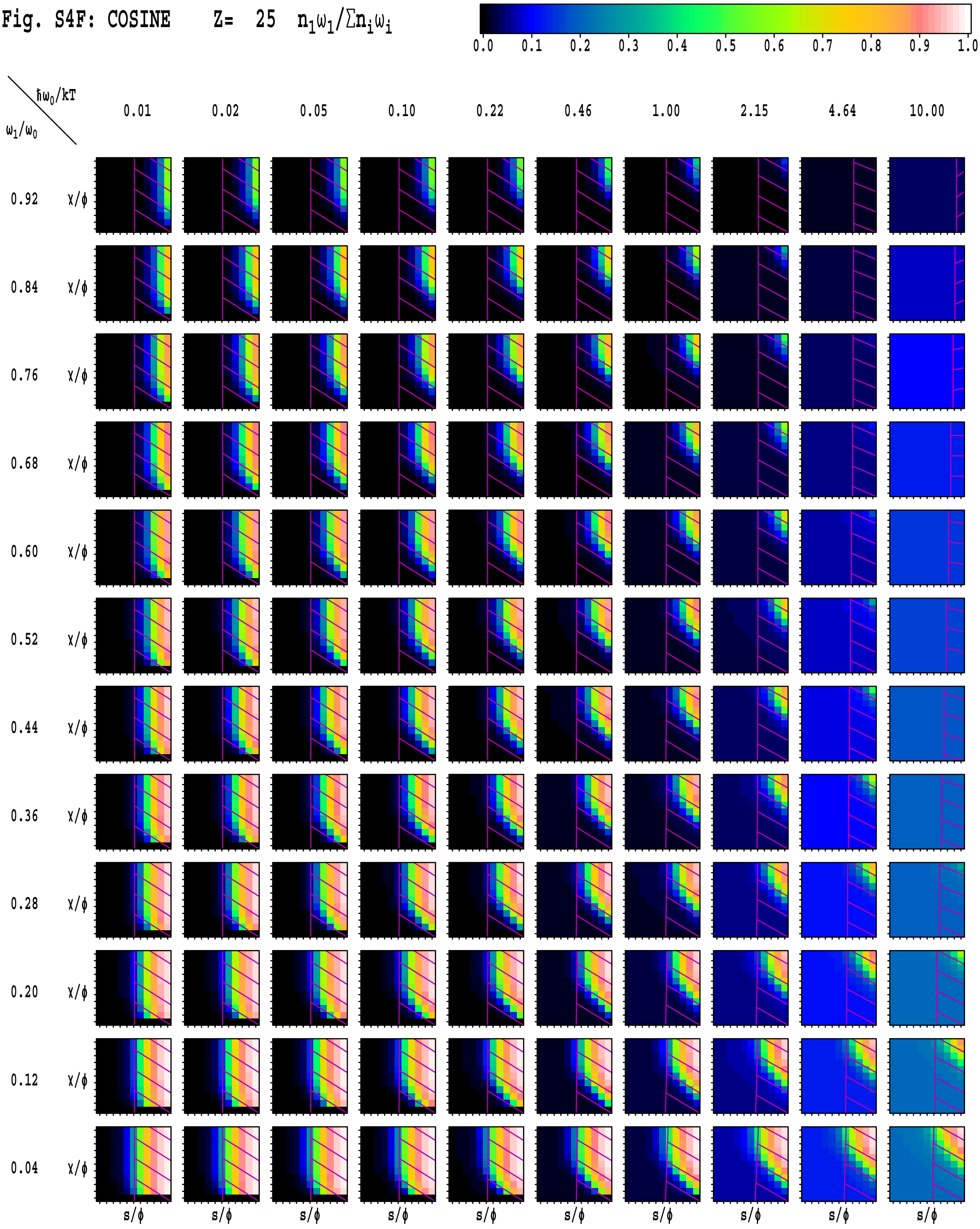

Fig. S4G: COSINE Z= 25 $n_1/n_1^{\chi=0}$

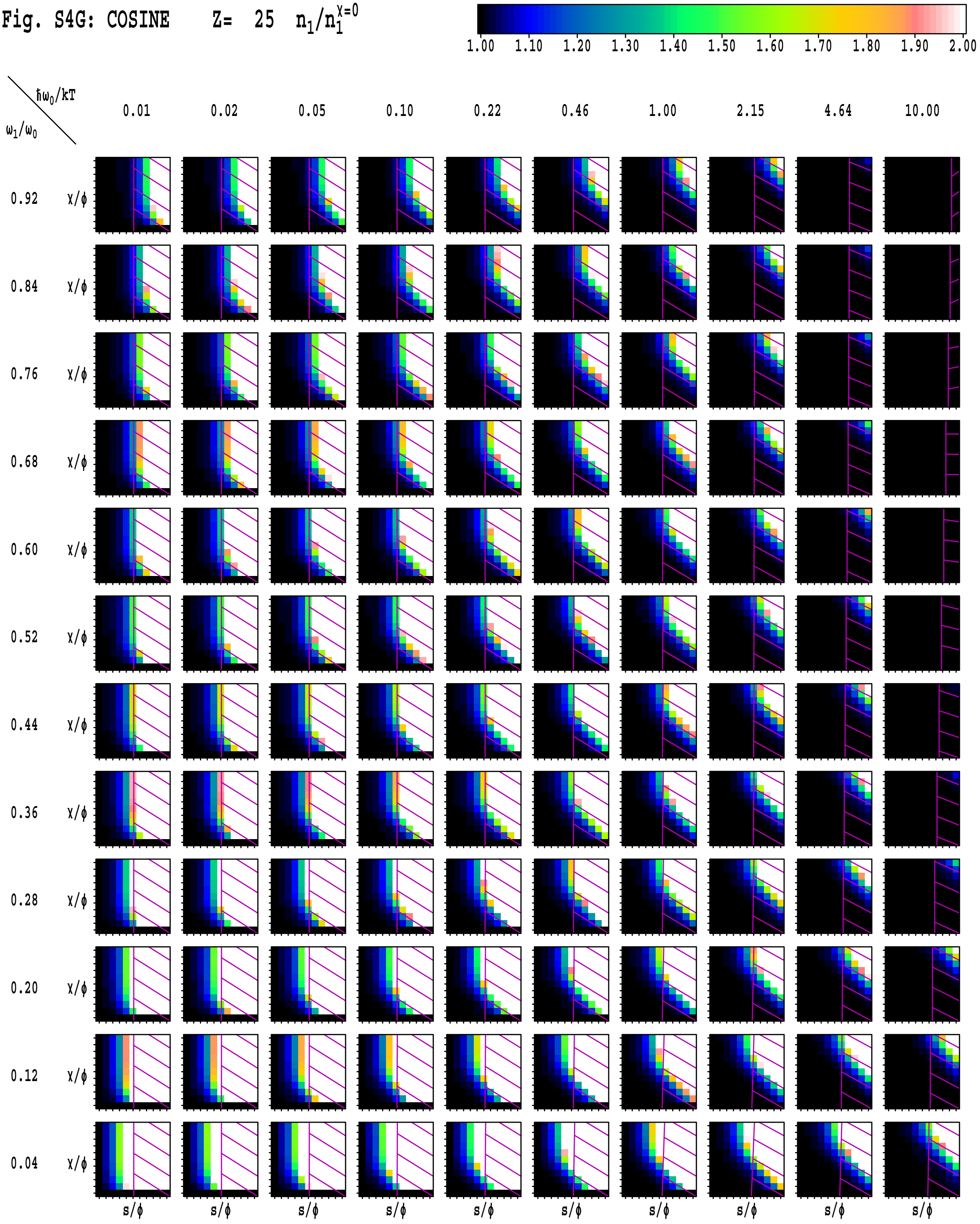

Fig. S5A: GAUSSIAN Z= 25 log T_S/T

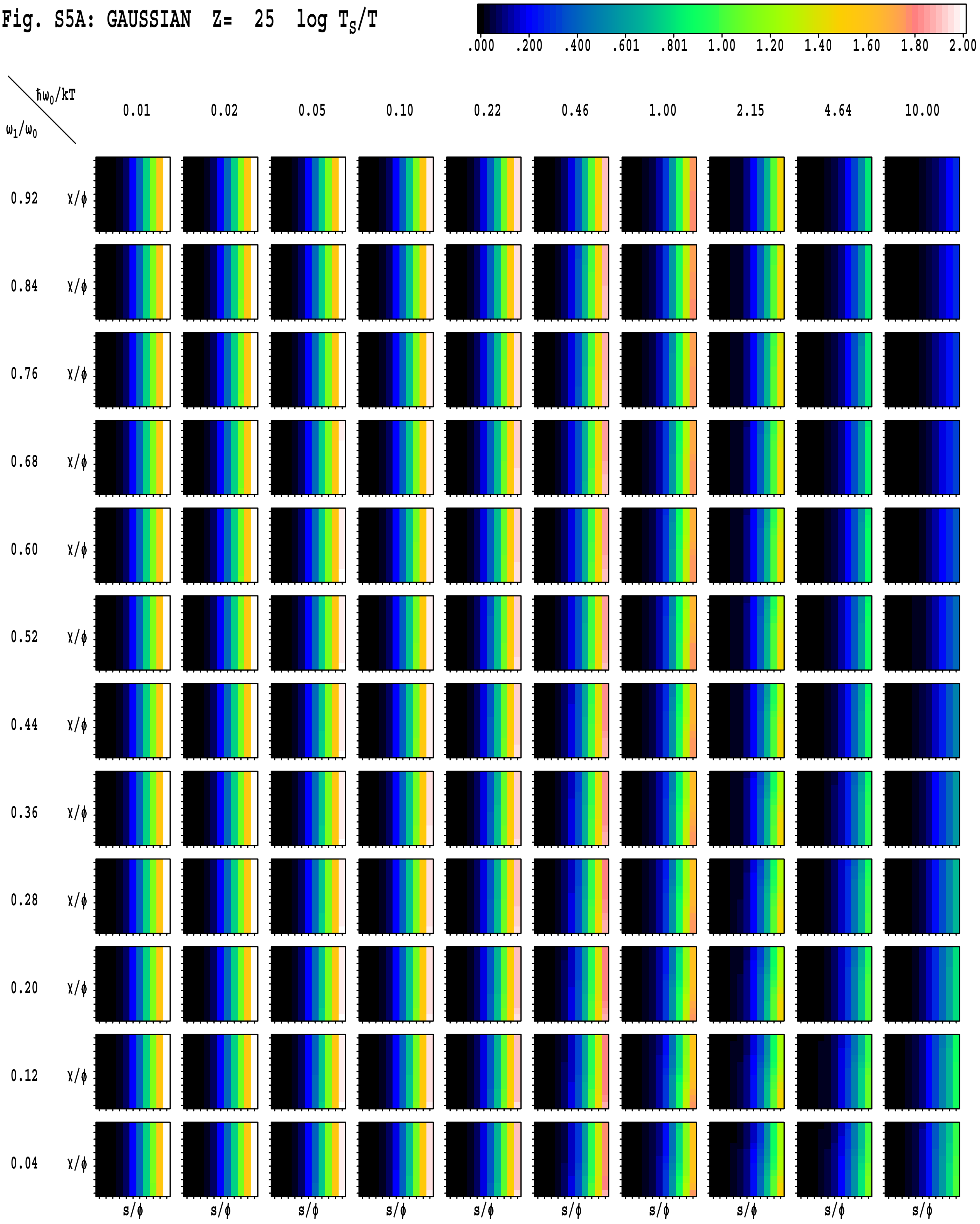

Fig. S5B: GAUSSIAN Z= 25 log N/z

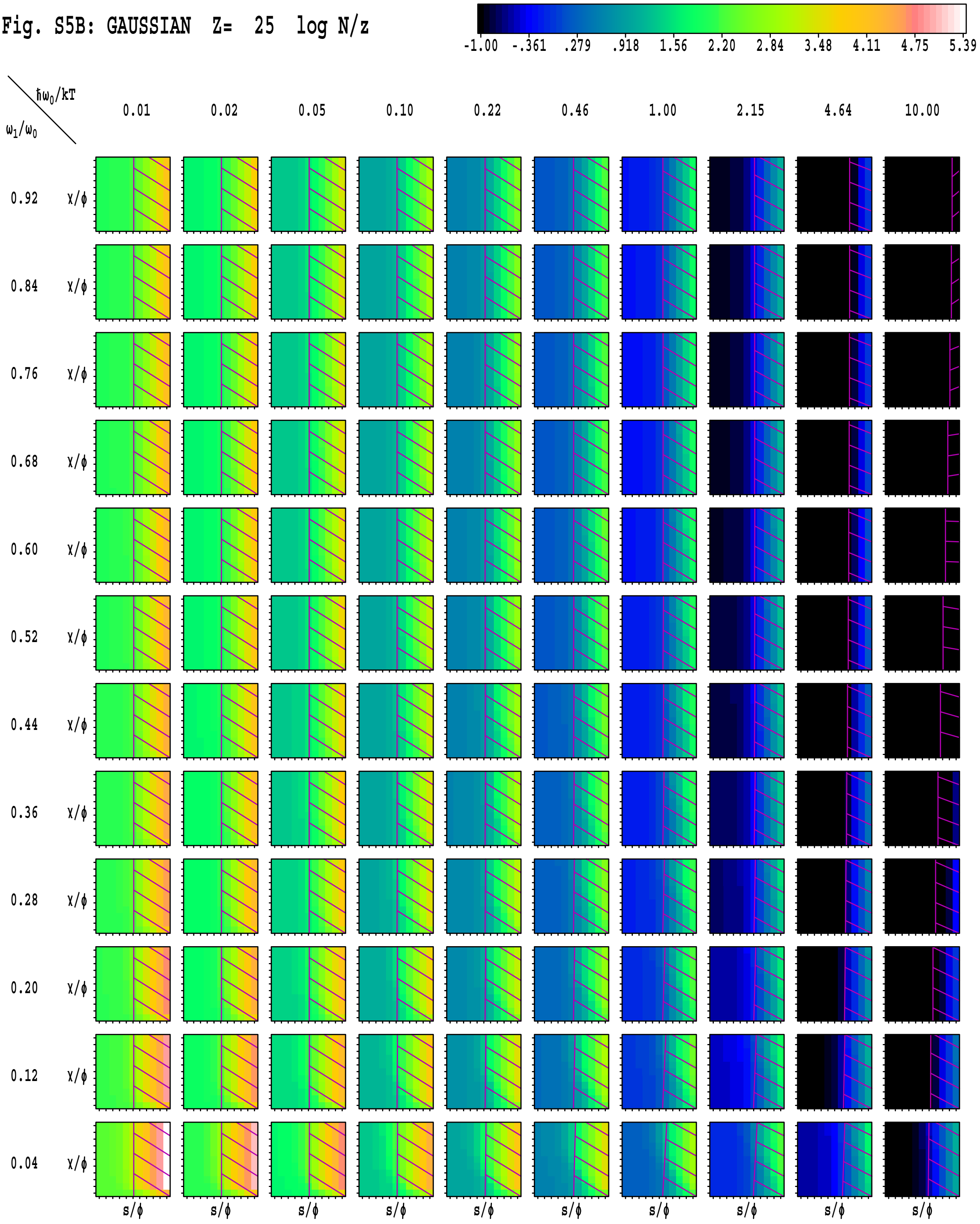

Fig. S5C: GAUSSIAN Z= 25 log $(N-N^{\chi=0})/z$

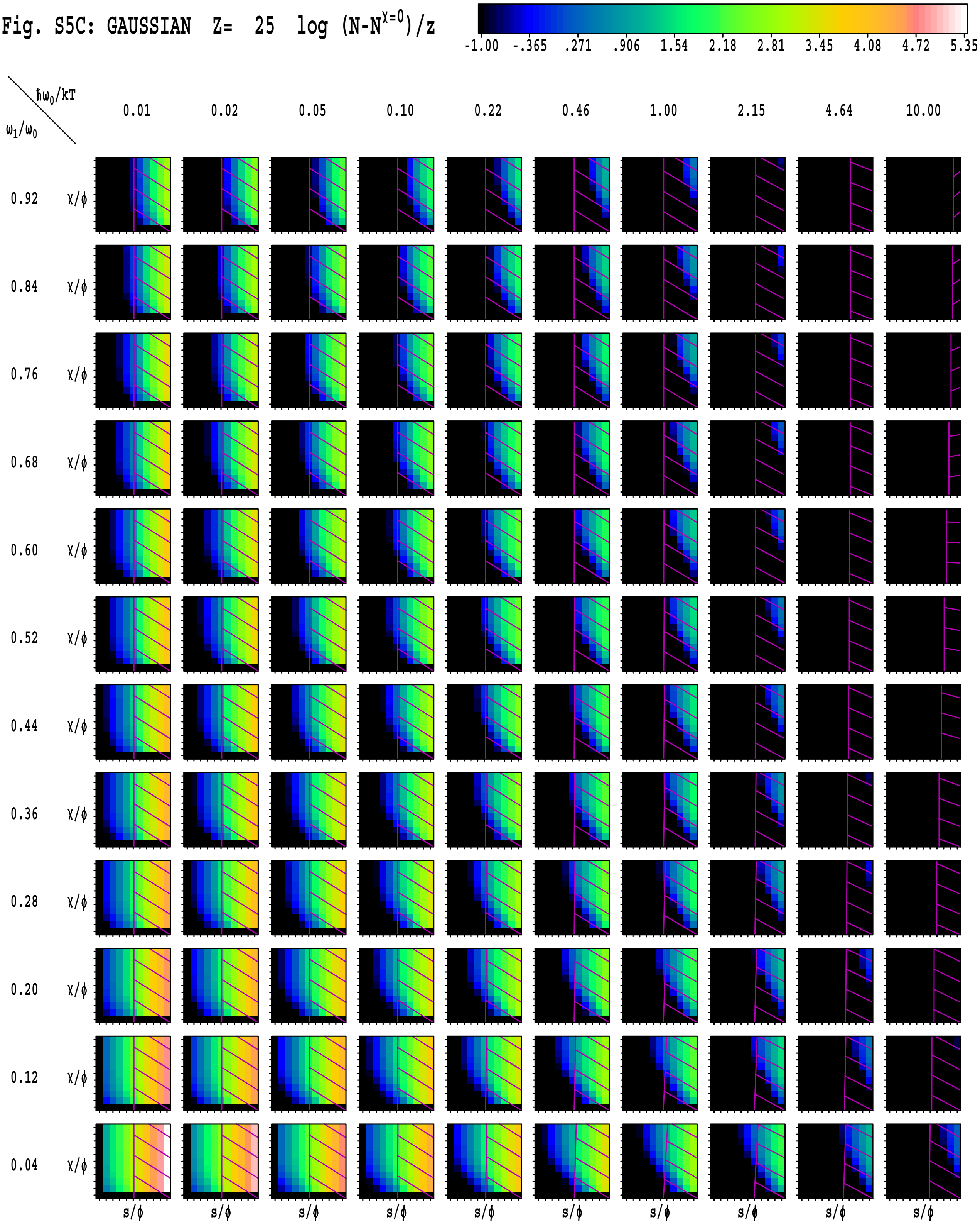

Fig. S5D: GAUSSIAN Z= 25 n_1/N

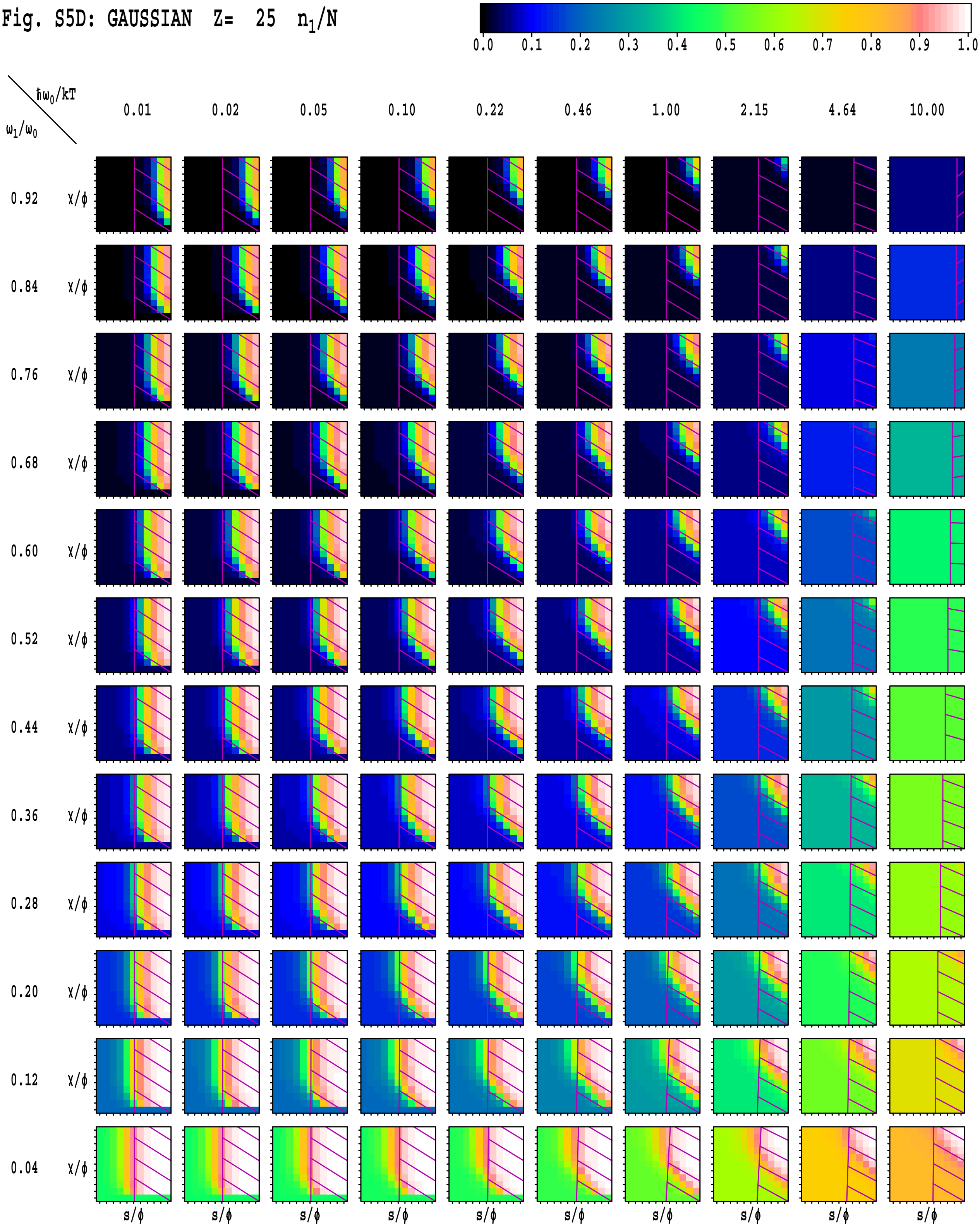

Fig. S5E: GAUSSIAN Z= 25 $\eta=(n_1-n_1^{\chi=0})/N$

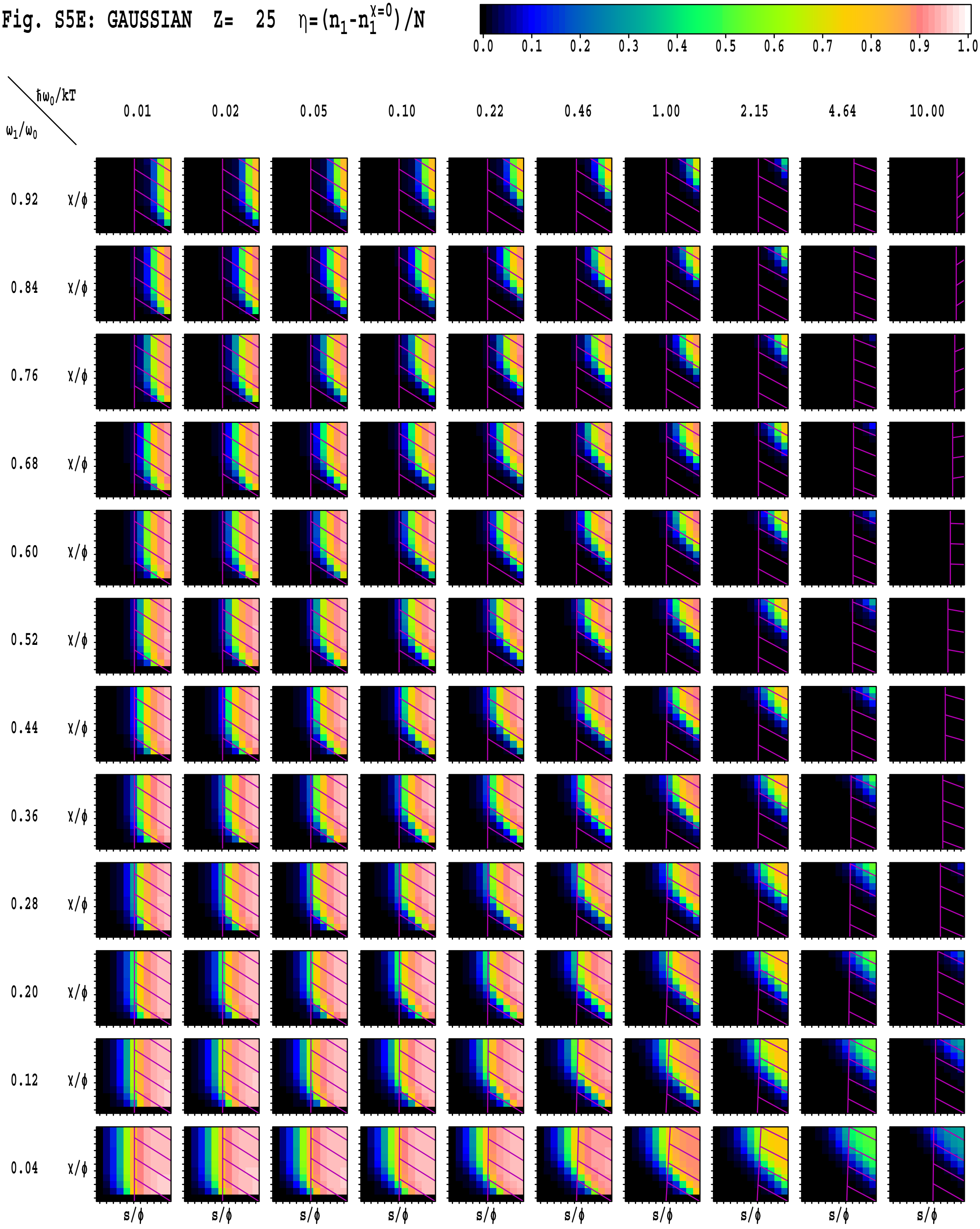

Fig. S5F: GAUSSIAN Z= 25 $n_1\omega_1/\Sigma n_i\omega_i$

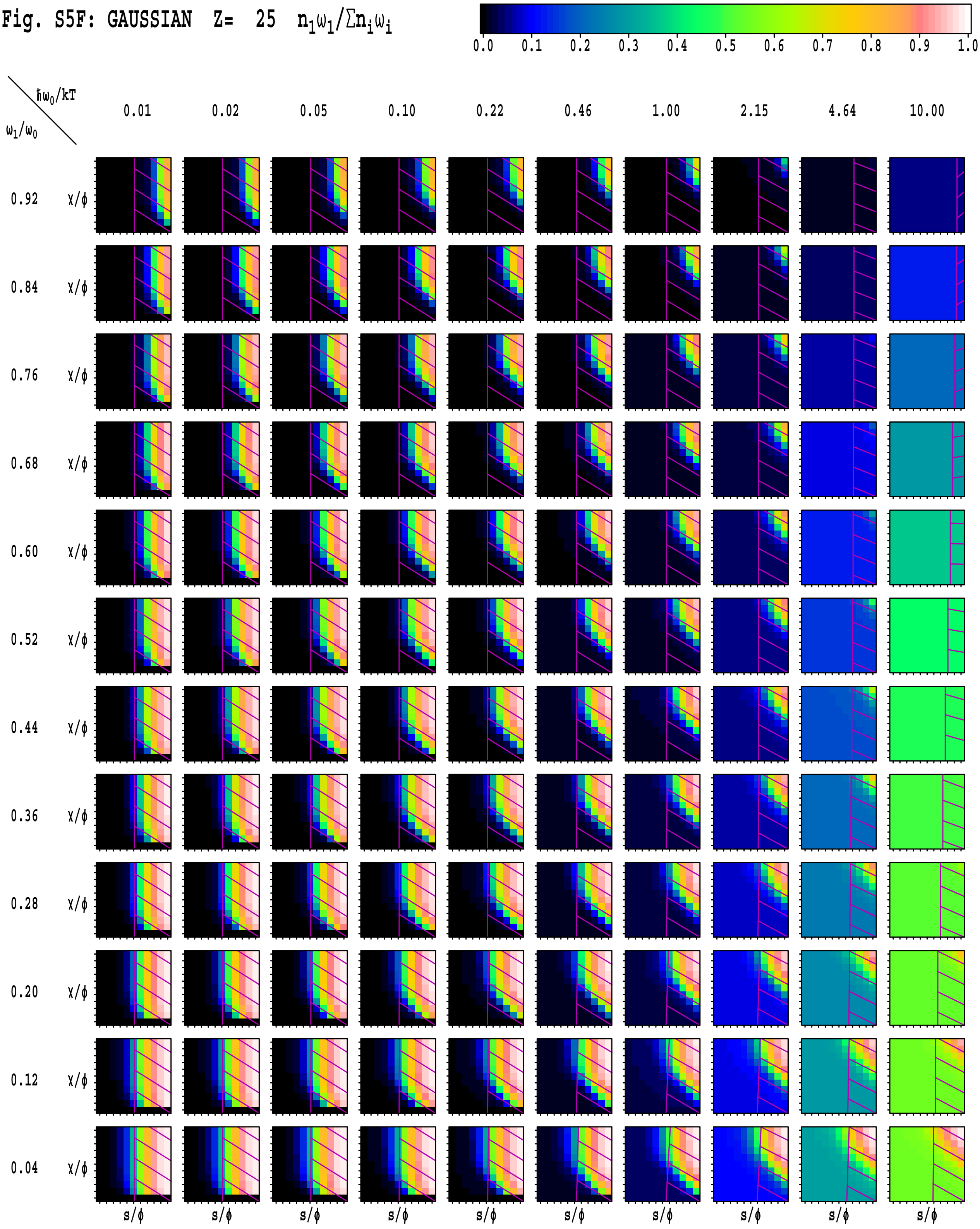

Fig. S5G: GAUSSIAN Z= 25 $n_1/n_1^{\chi=0}$

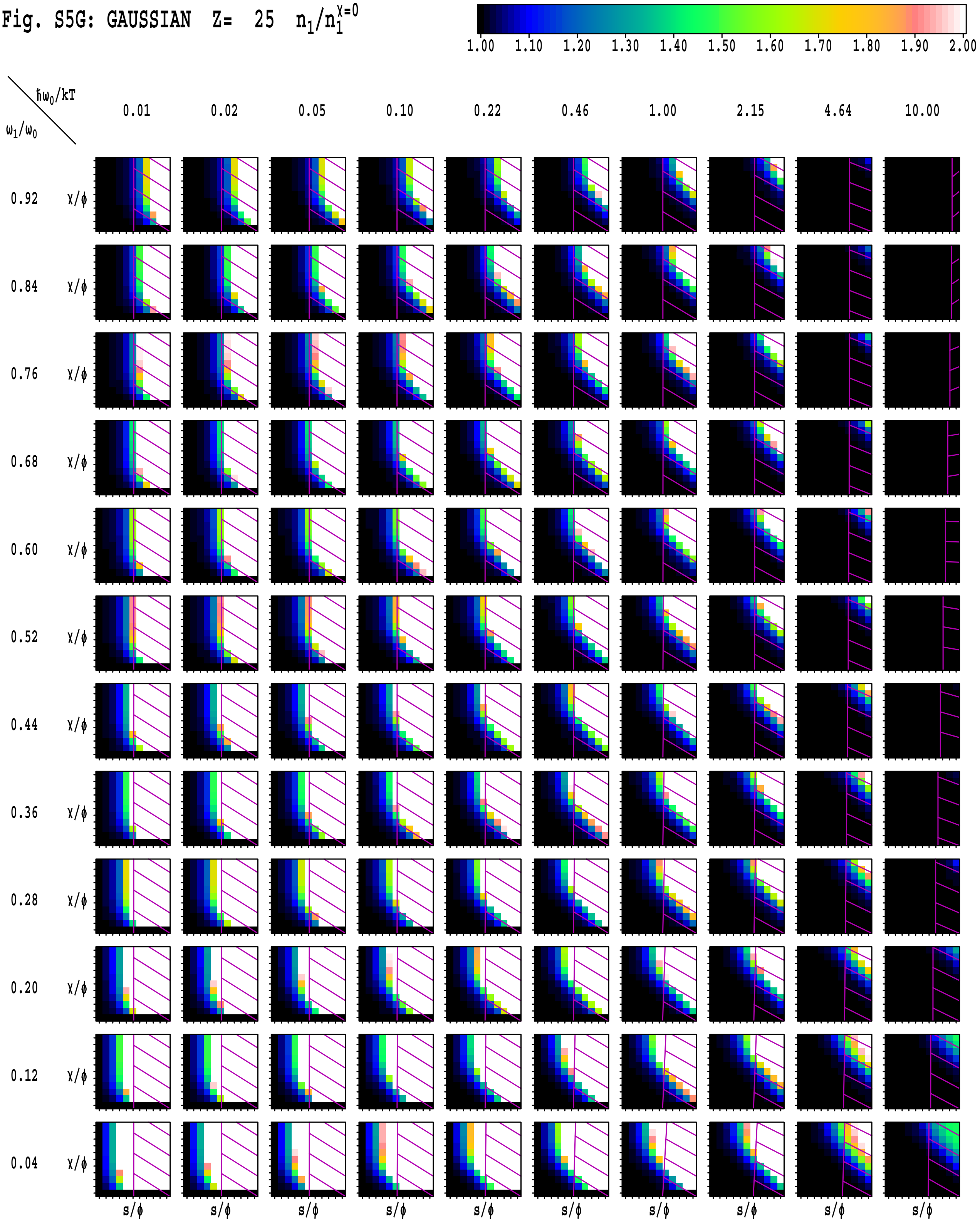

Fig. S6A: CLASSICAL Z= 25 log T_S/T

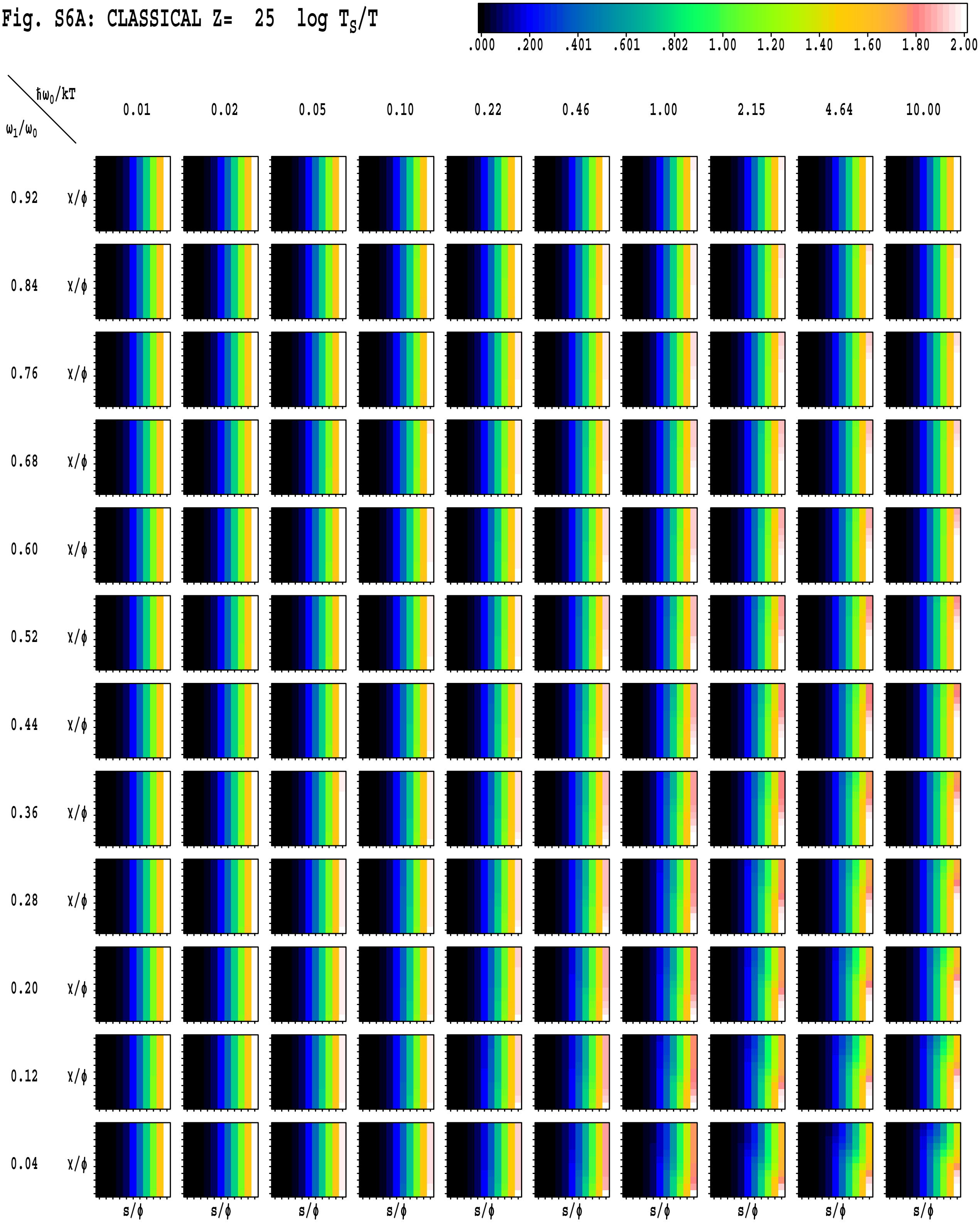

Fig. S6B: CLASSICAL Z= 25 log N/z

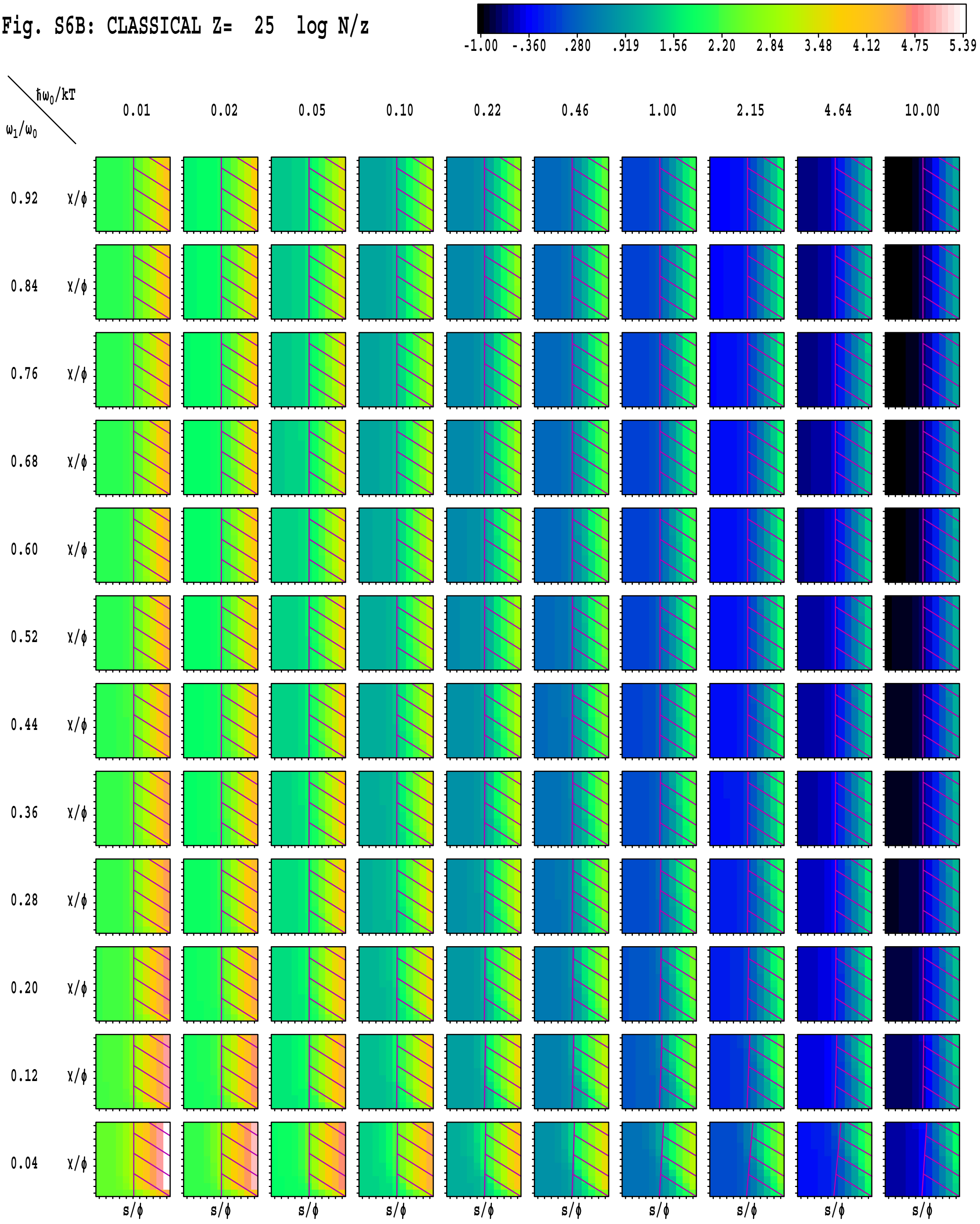

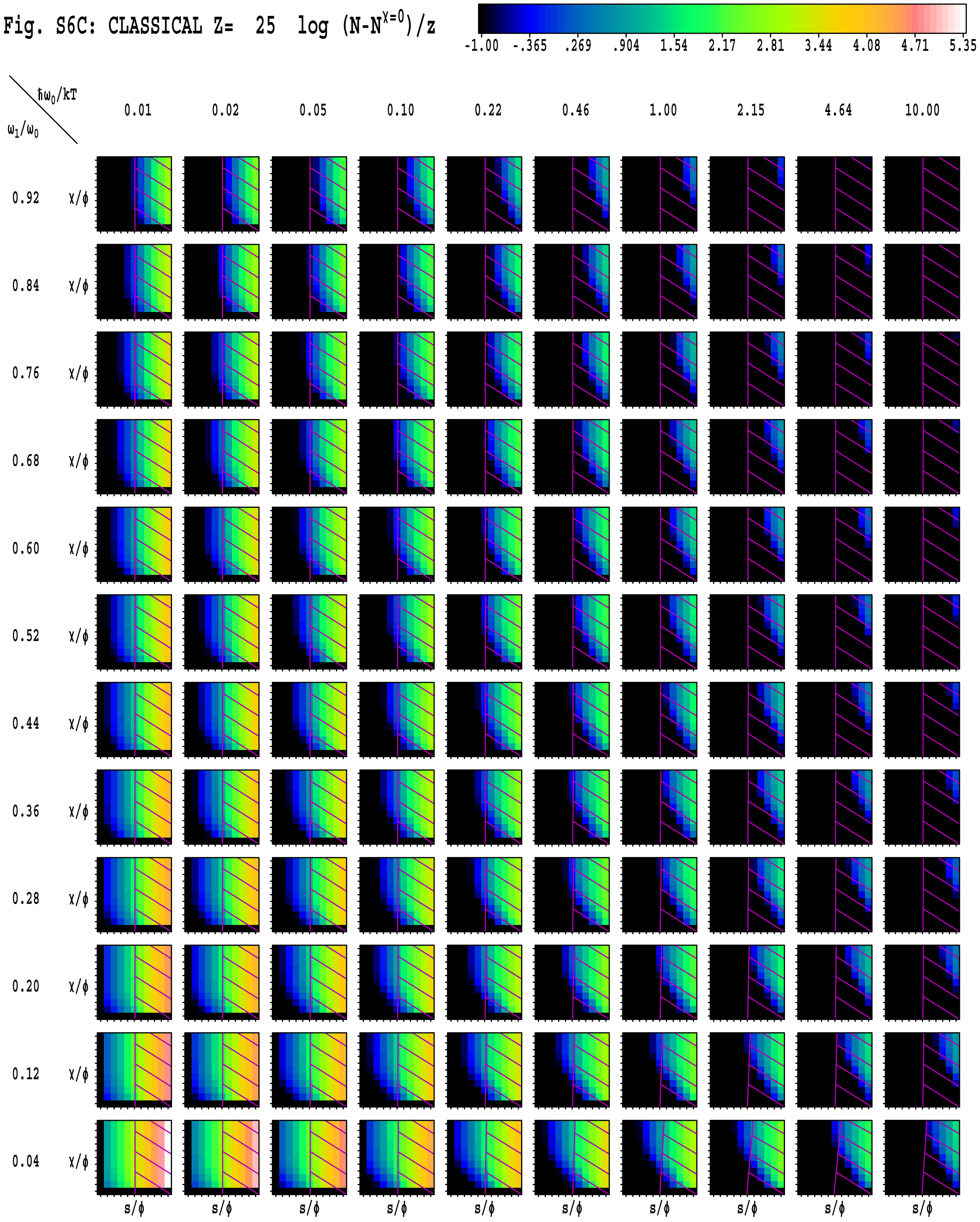

Fig. S6C: CLASSICAL Z= 25 log $(N-N^{\chi=0})/z$

Fig. S6D: CLASSICAL Z= 25 n_1/N

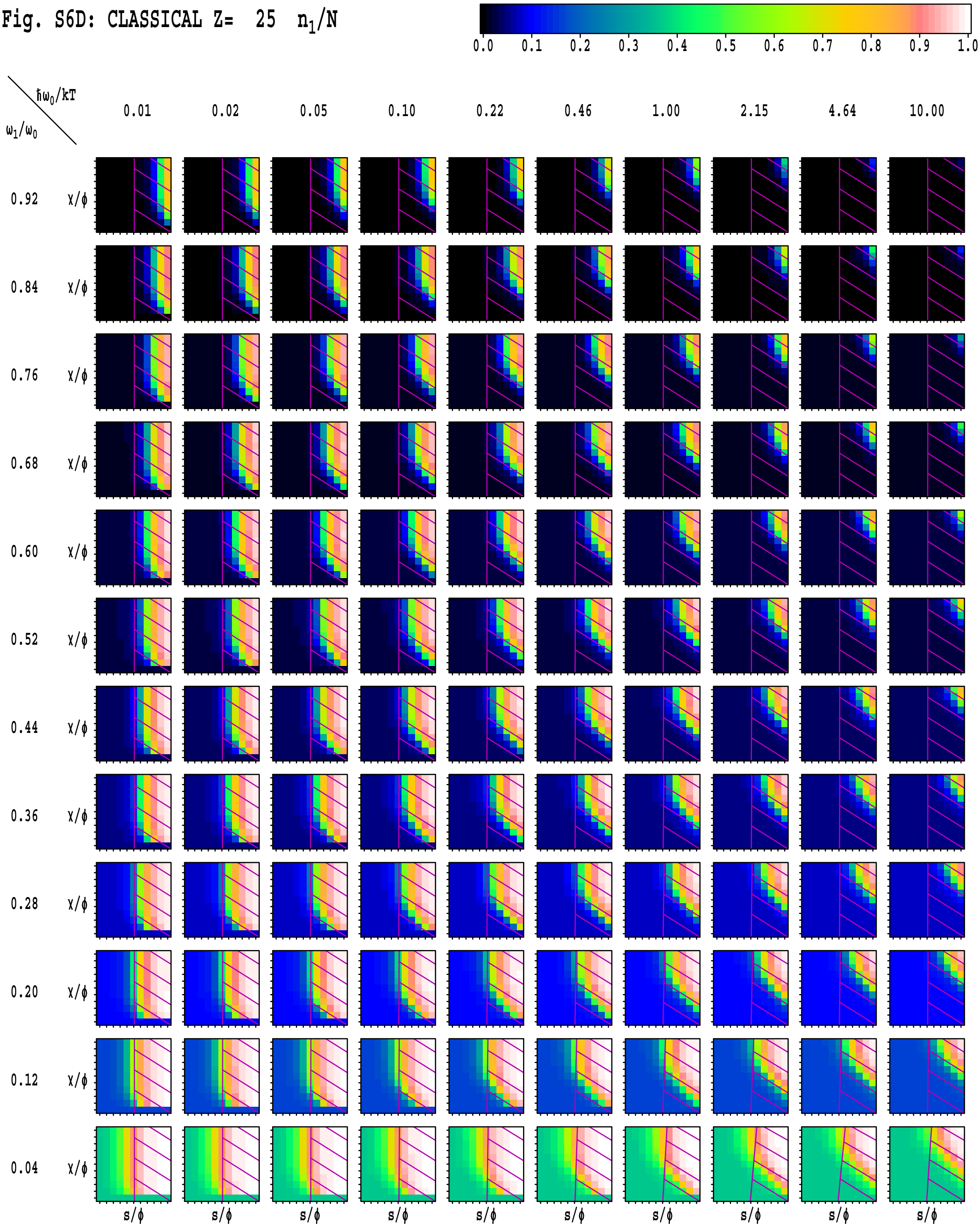

Fig. S6E: CLASSICAL Z= 25 $\eta=(n_1-n_1^{\chi=0})/N$

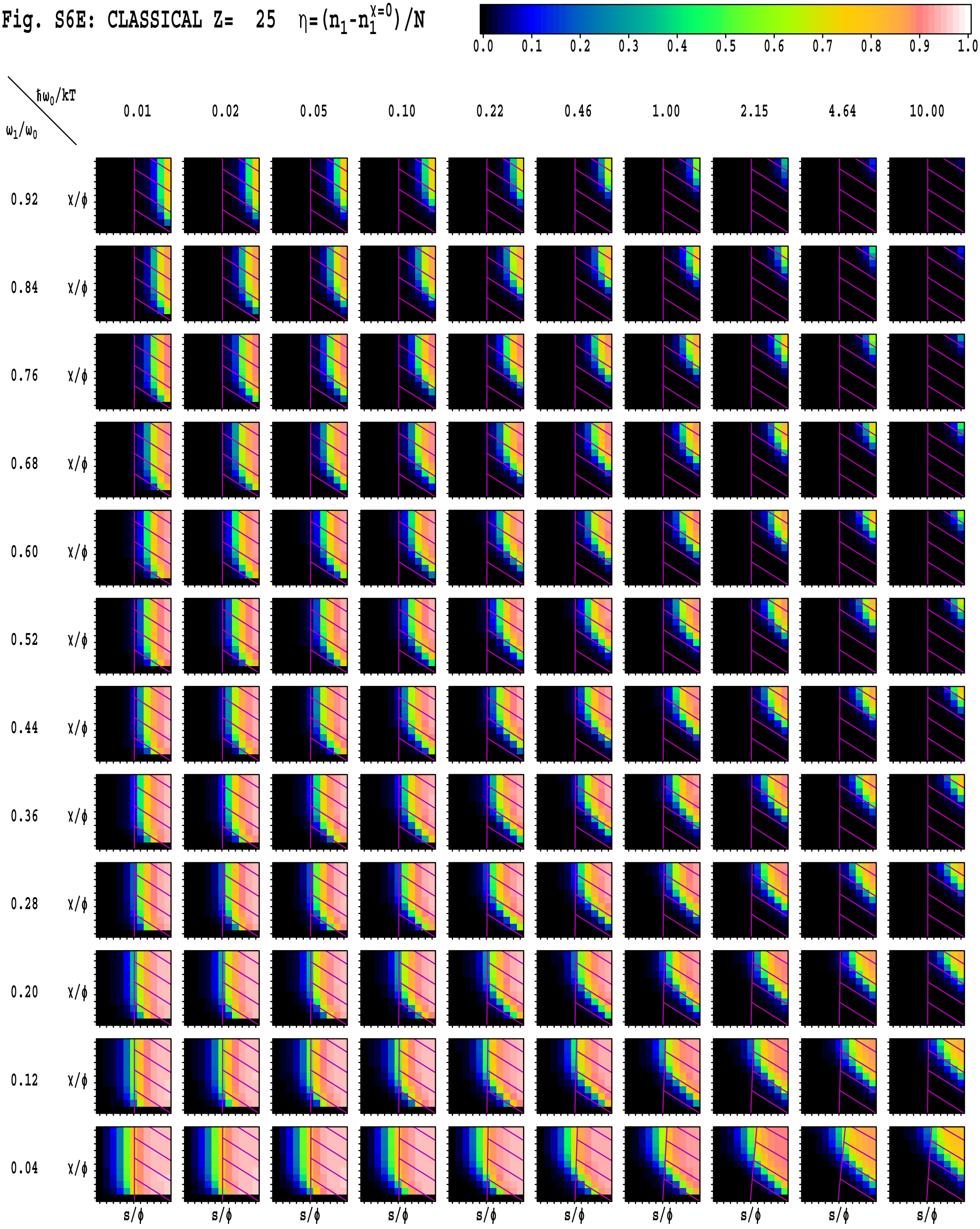

Fig. S6F: CLASSICAL Z= 25 $n_1\omega_1/\sum n_i\omega_i$

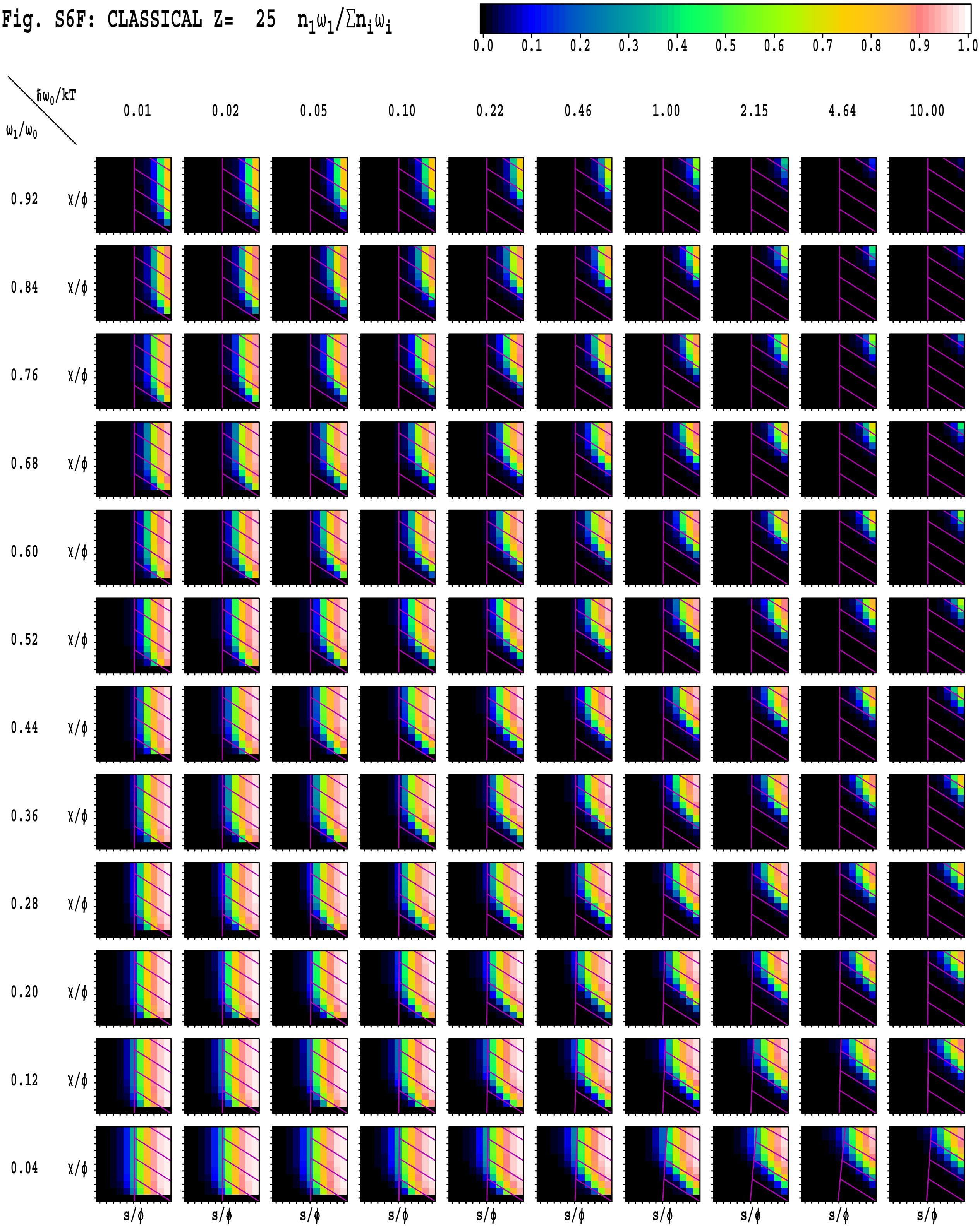

Fig. S6G: CLASSICAL Z= 25 $n_1/n_1^{\chi=0}$

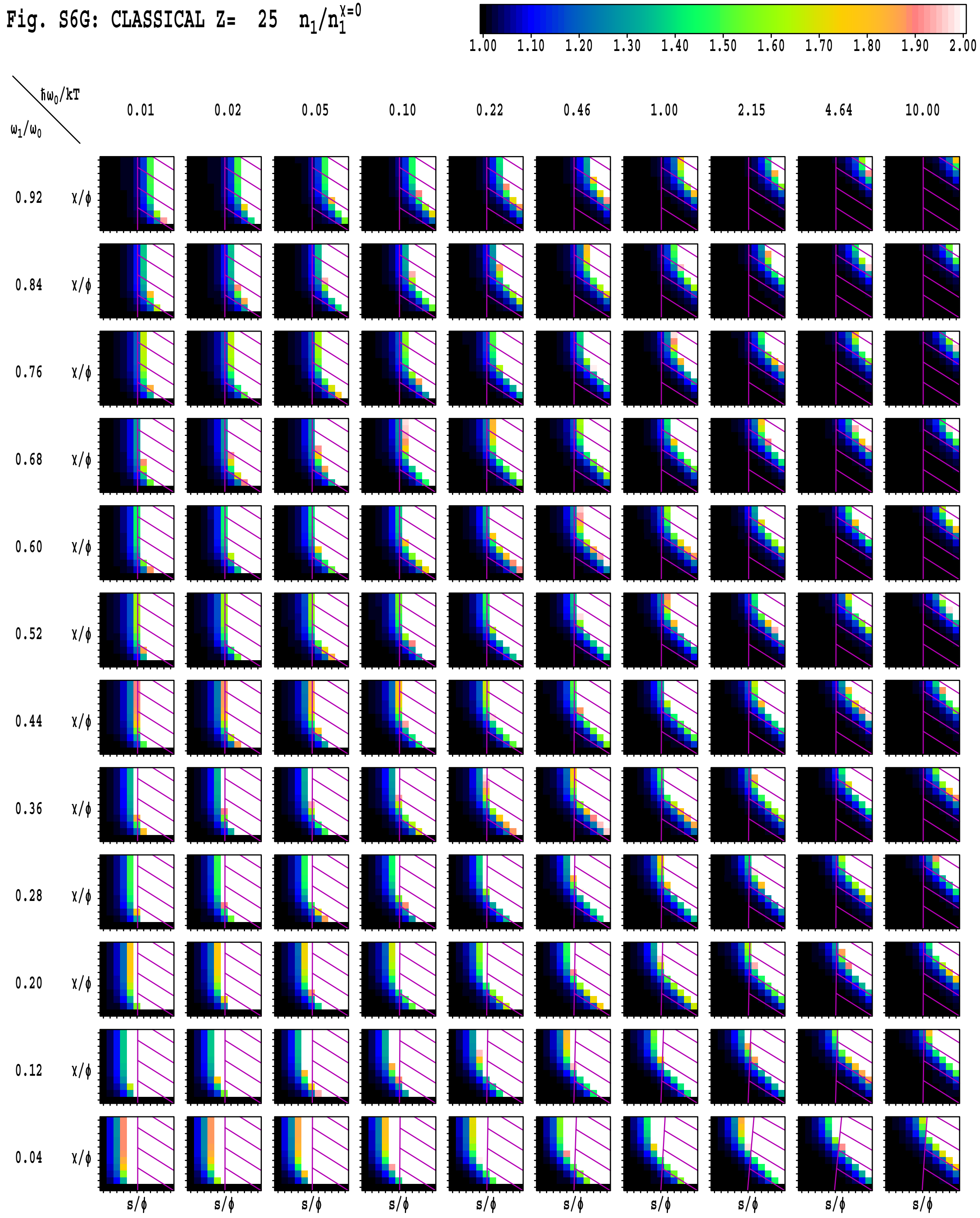

Fig. S7A: ANALYTICAL

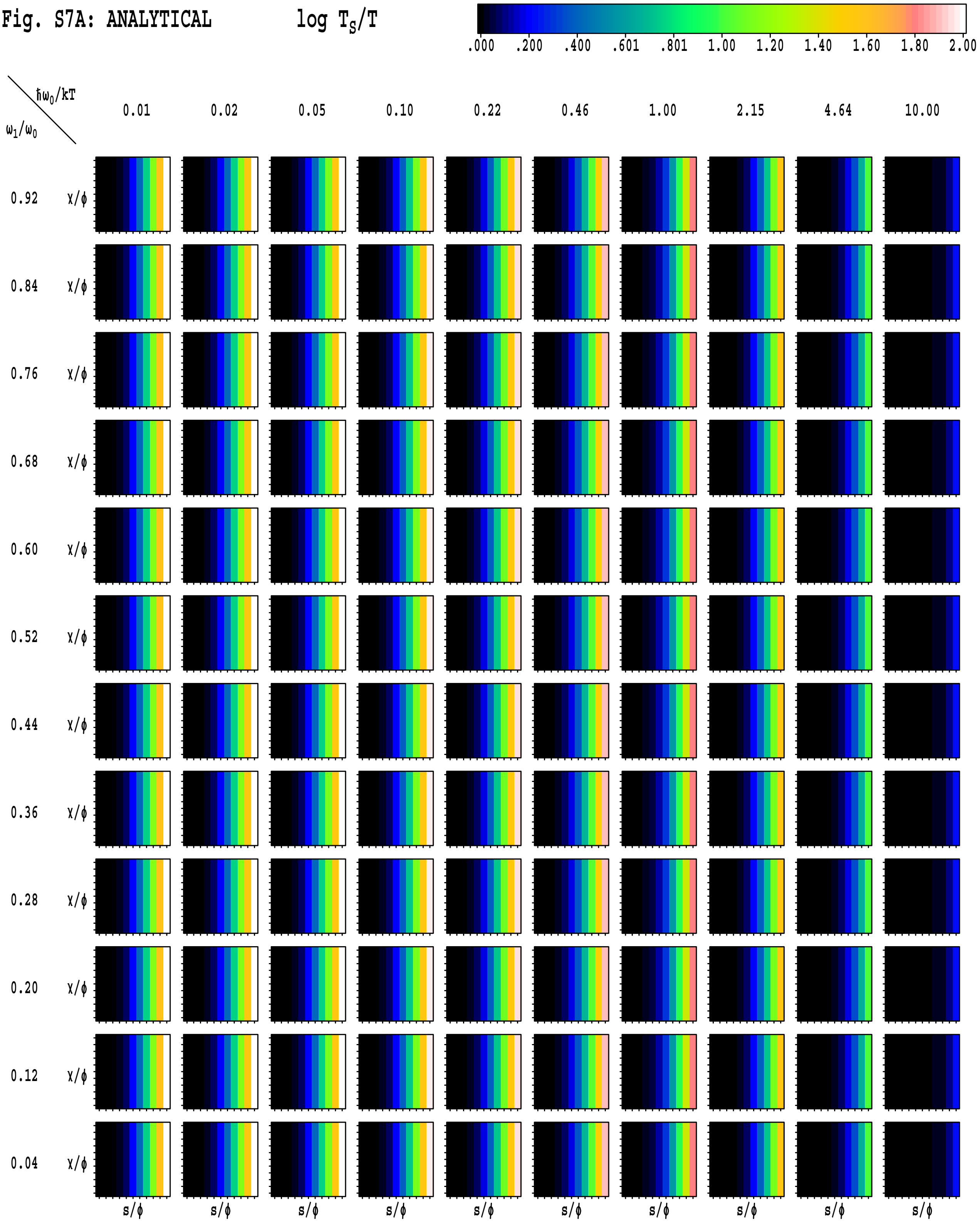

Fig. S7B: ANALYTICAL

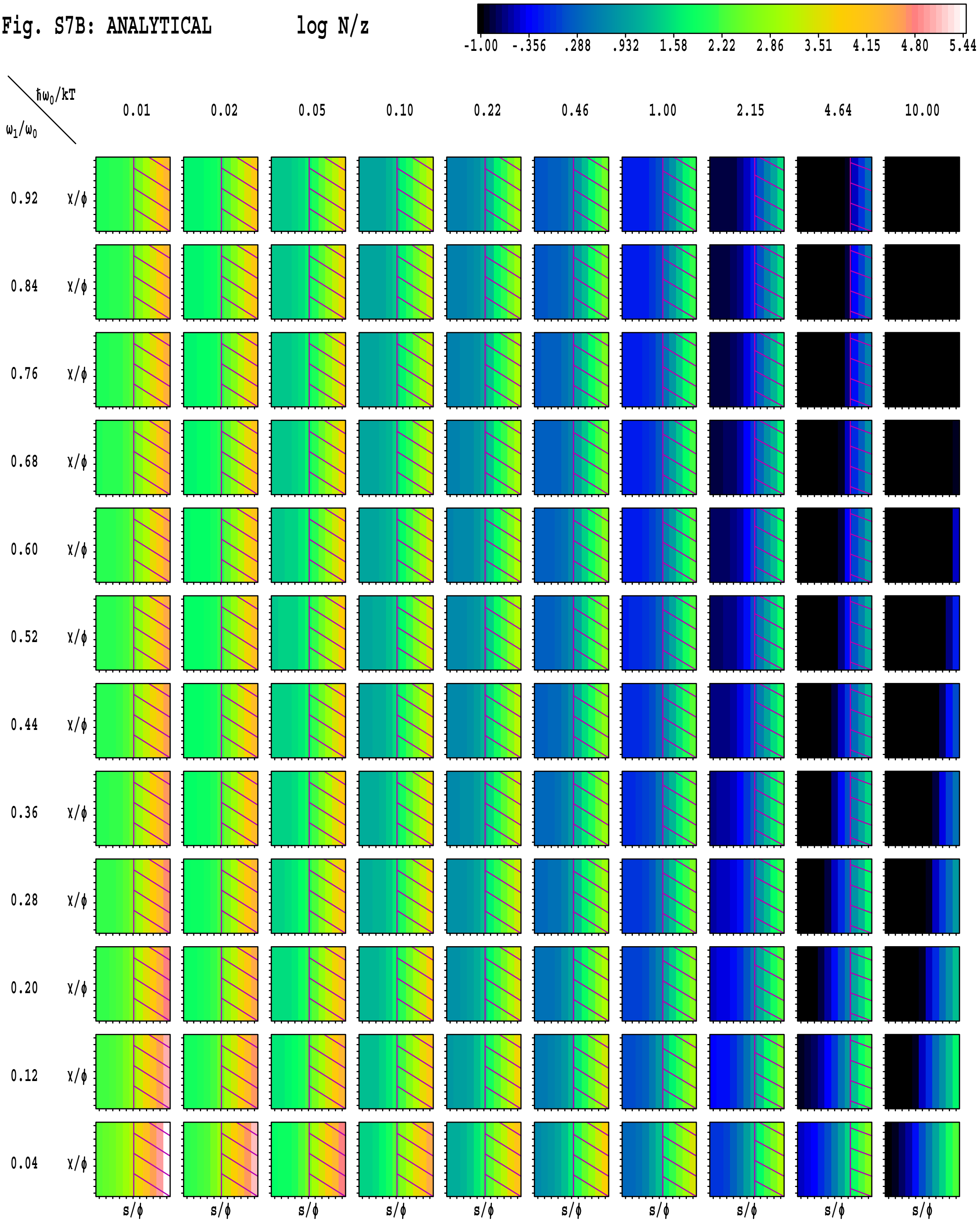

Fig. S7C: ANALYTICAL

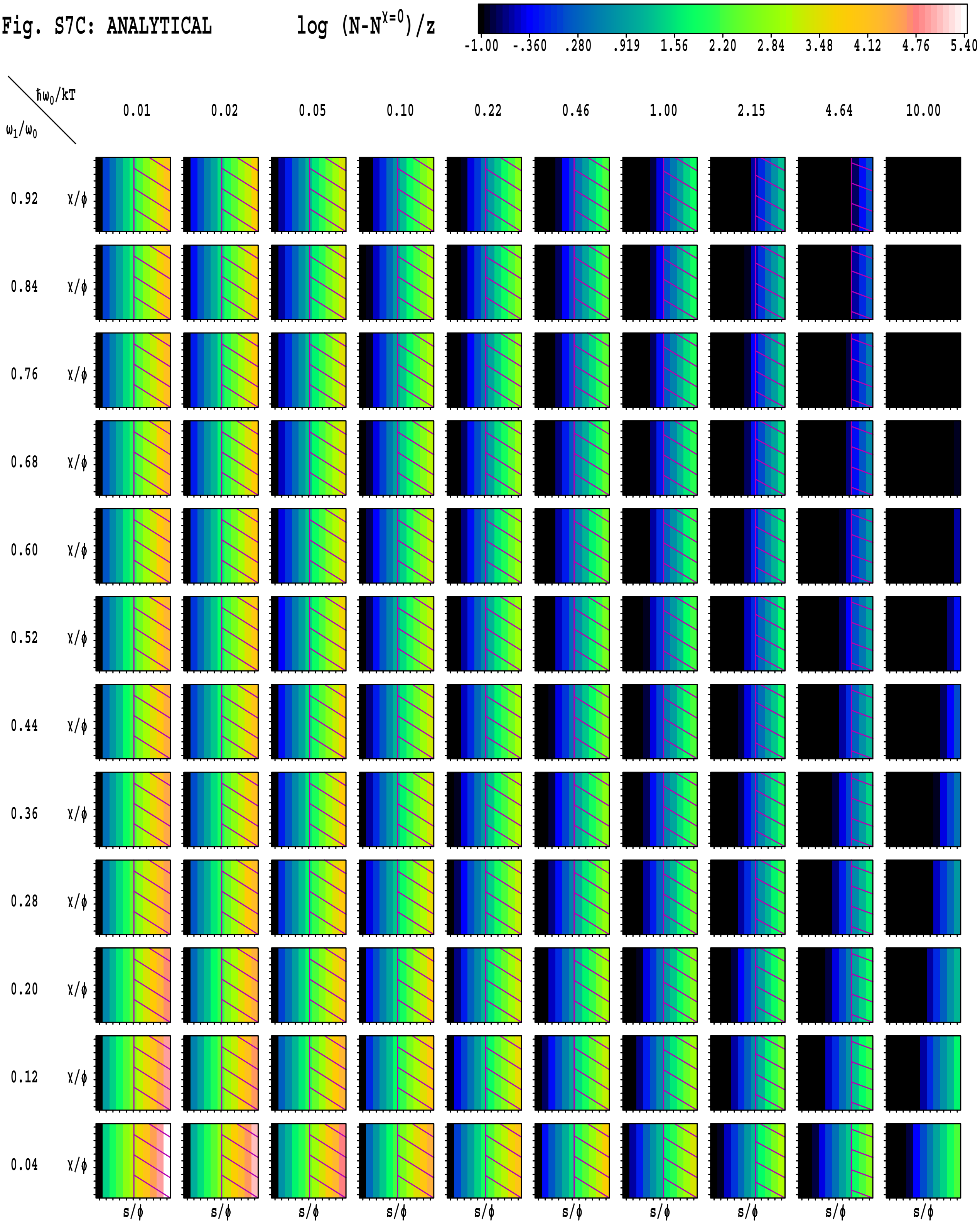

Fig. S8A: LINEAR χ_3 log T_S/T

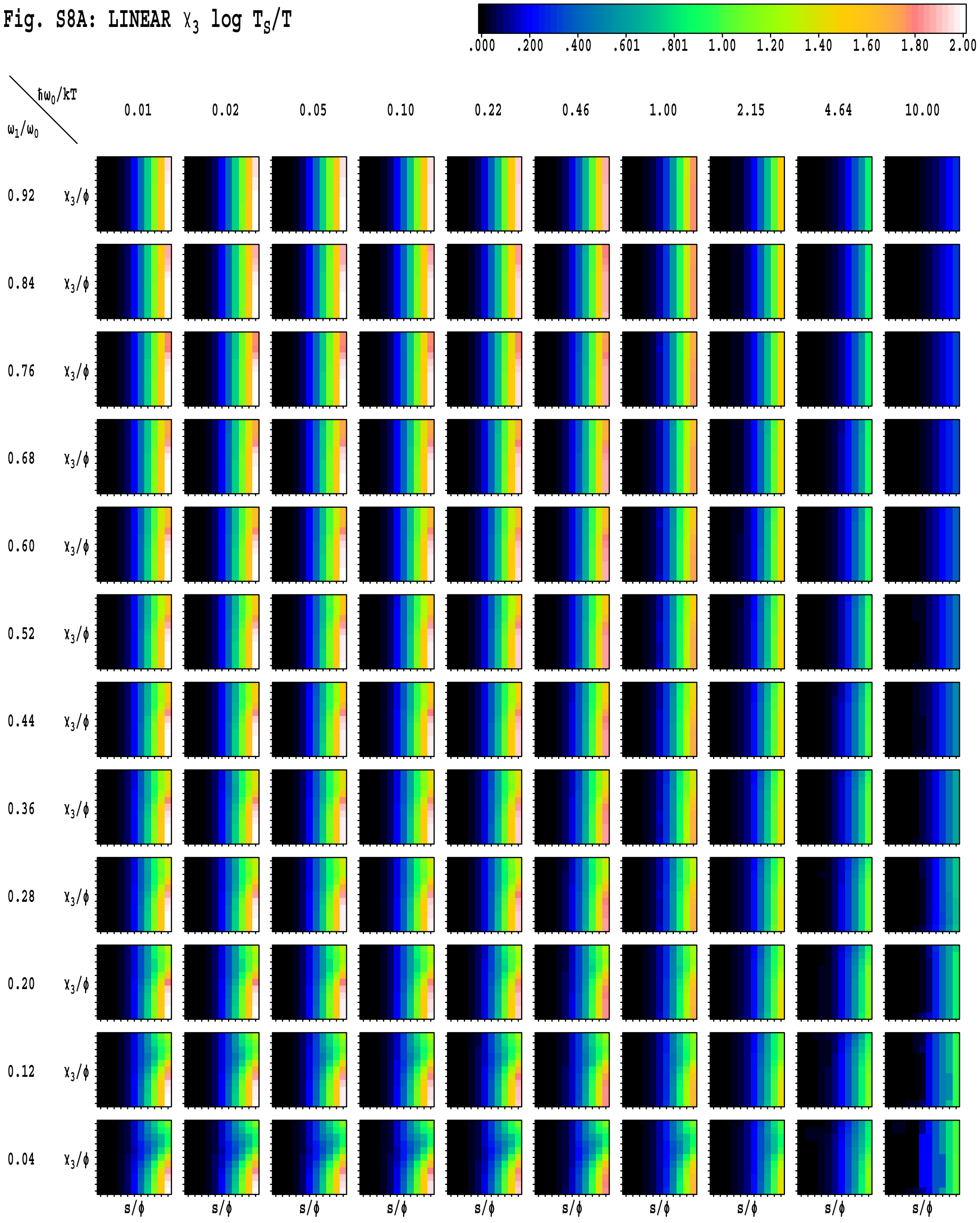

Fig. S8B: LINEAR χ_3 log N/z

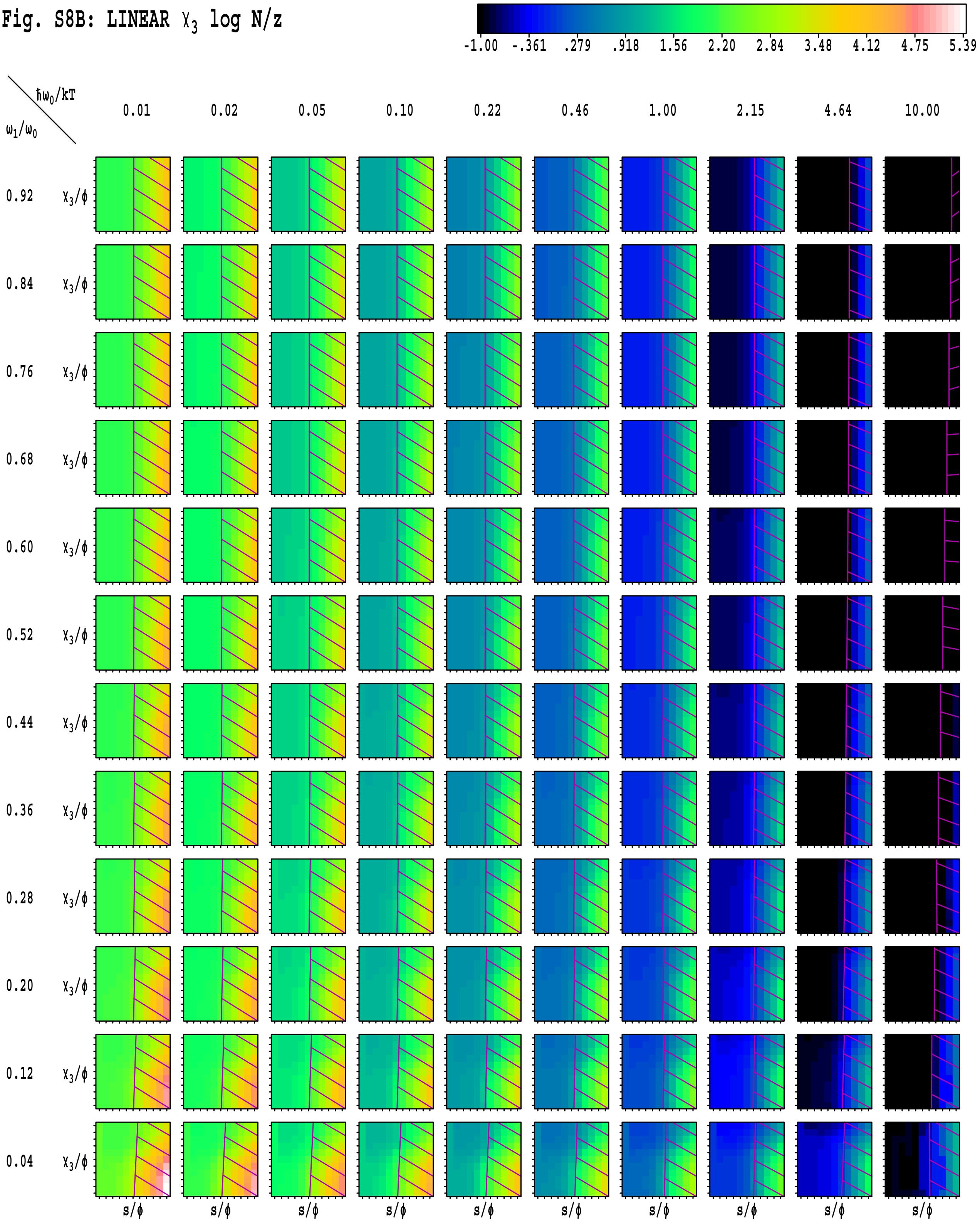

Fig. S8C: LINEAR χ_3 log $(N-N^{\chi=0})/z$

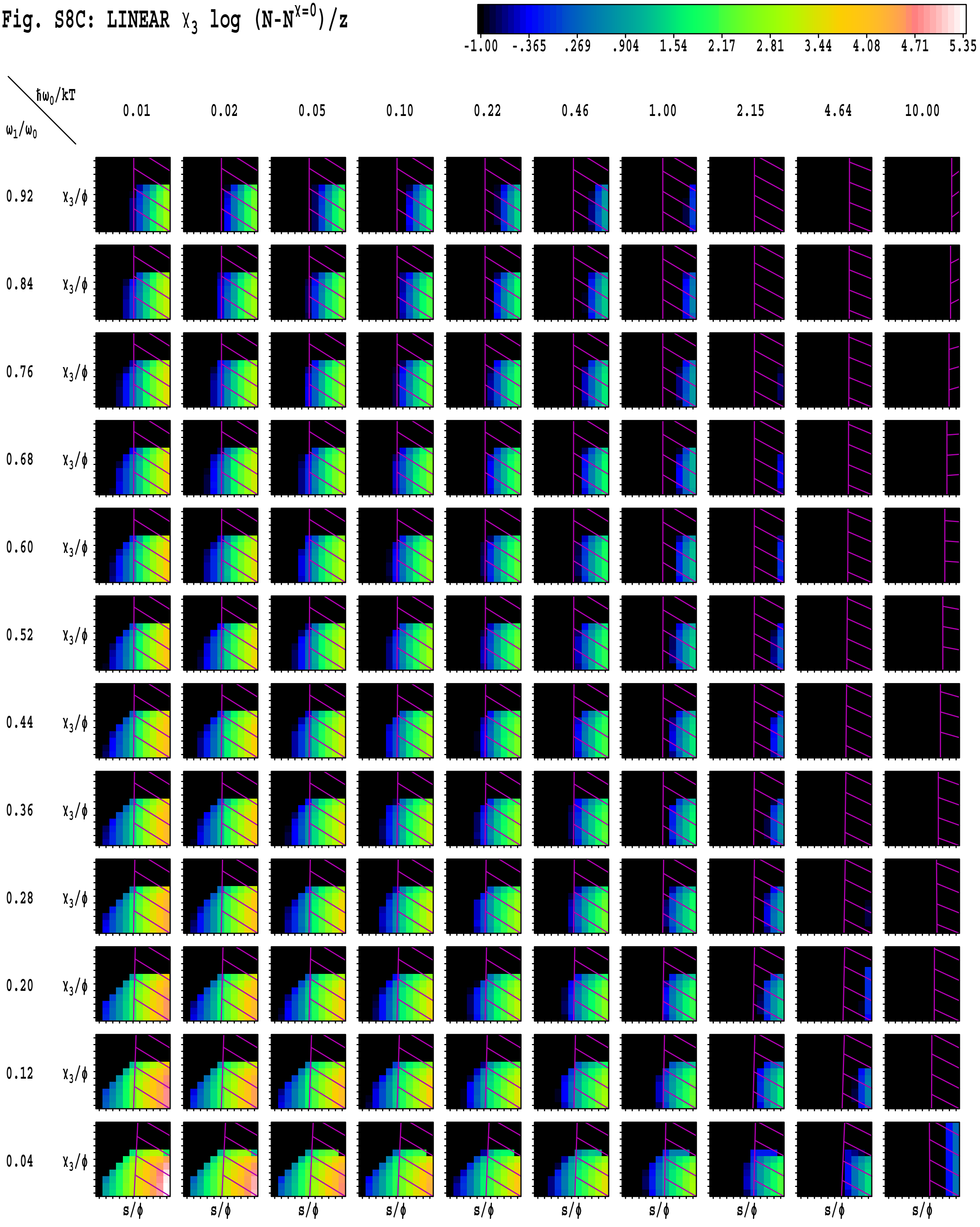

Fig. S8D: LINEAR χ_3 n_1/N

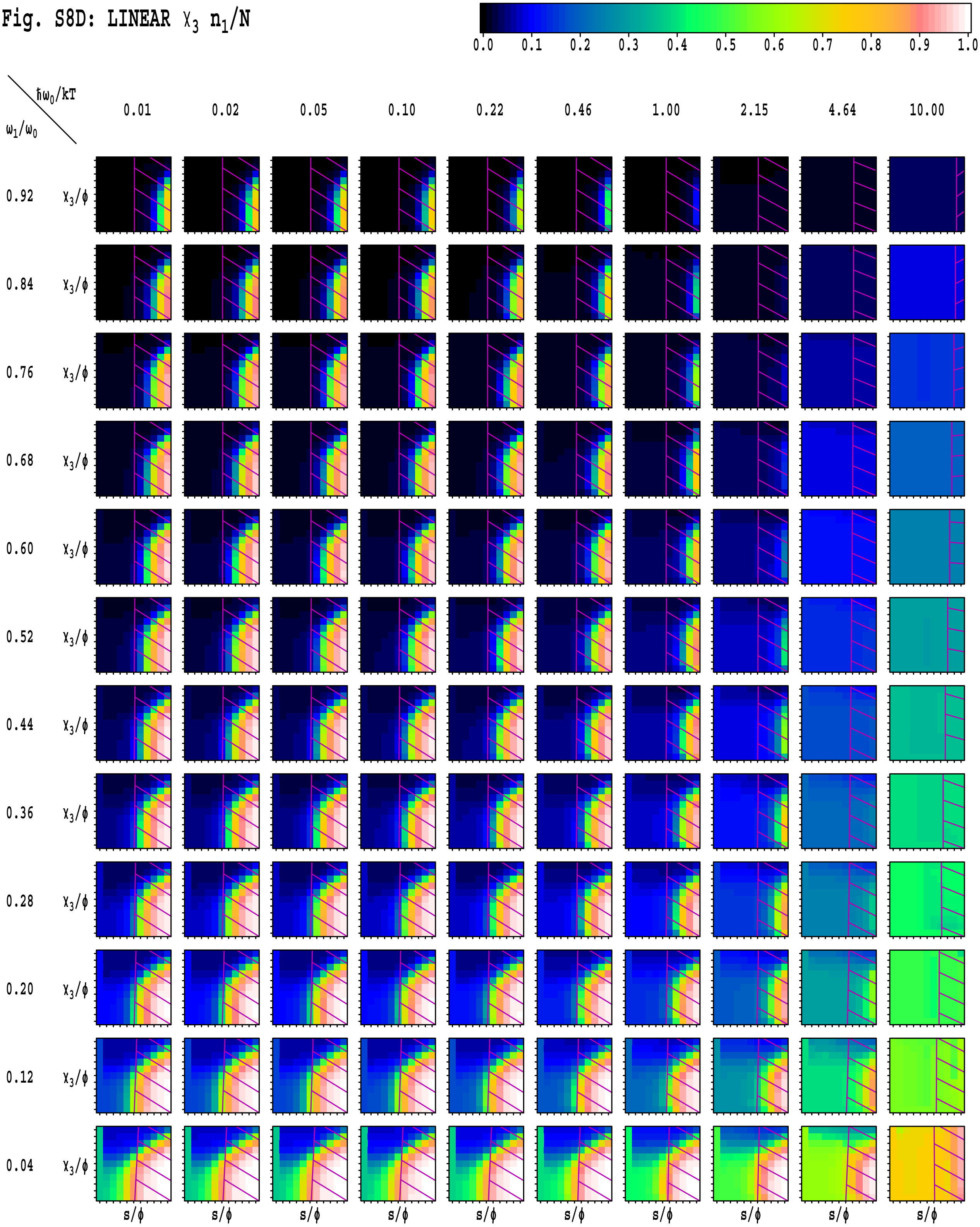

Fig. S8E: LINEAR χ_3 $\eta=(n_1-n_1^{\chi=0})/N$

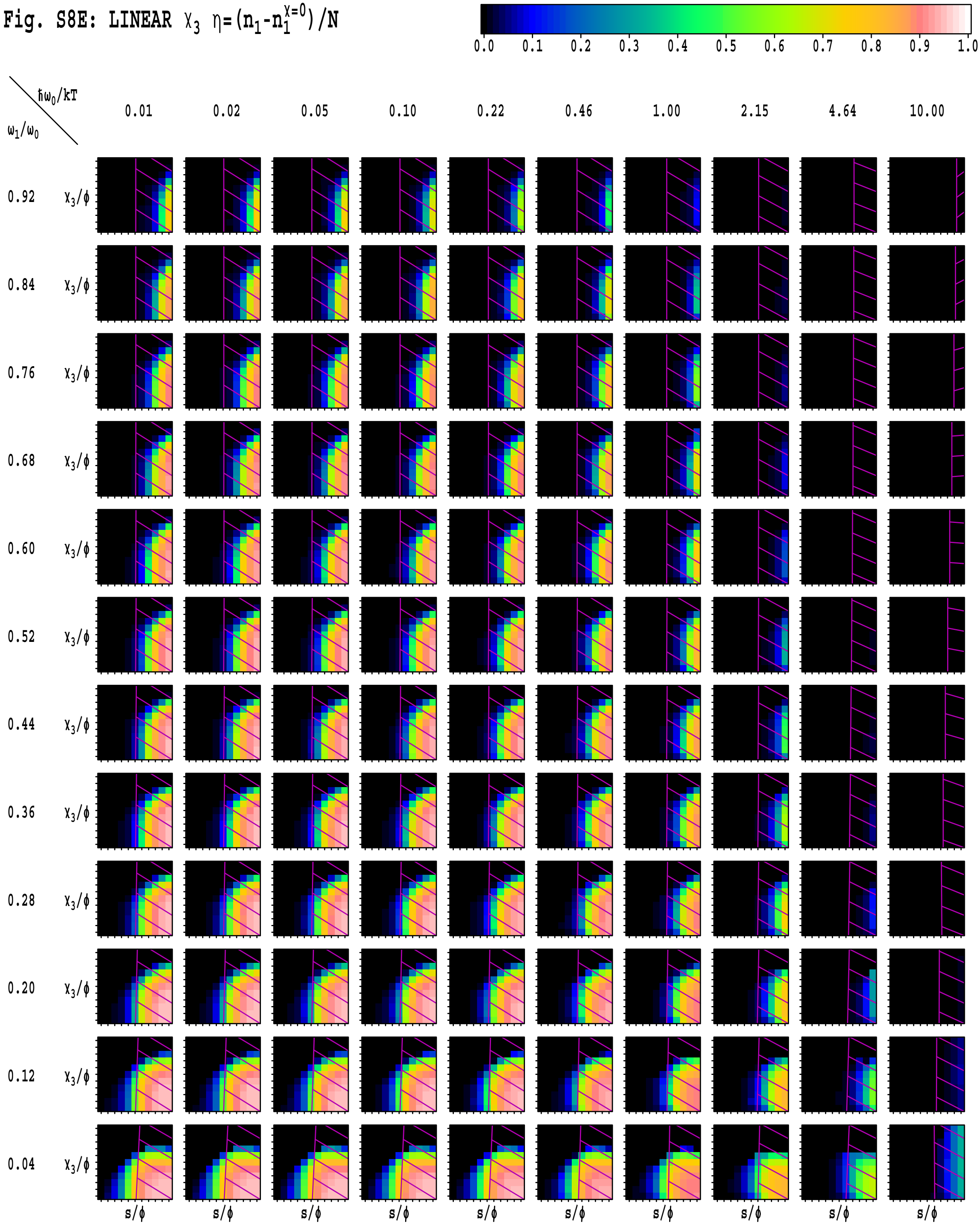

Fig. S8F: LINEAR χ_3 $n_1\omega_1/\sum n_i\omega_i$

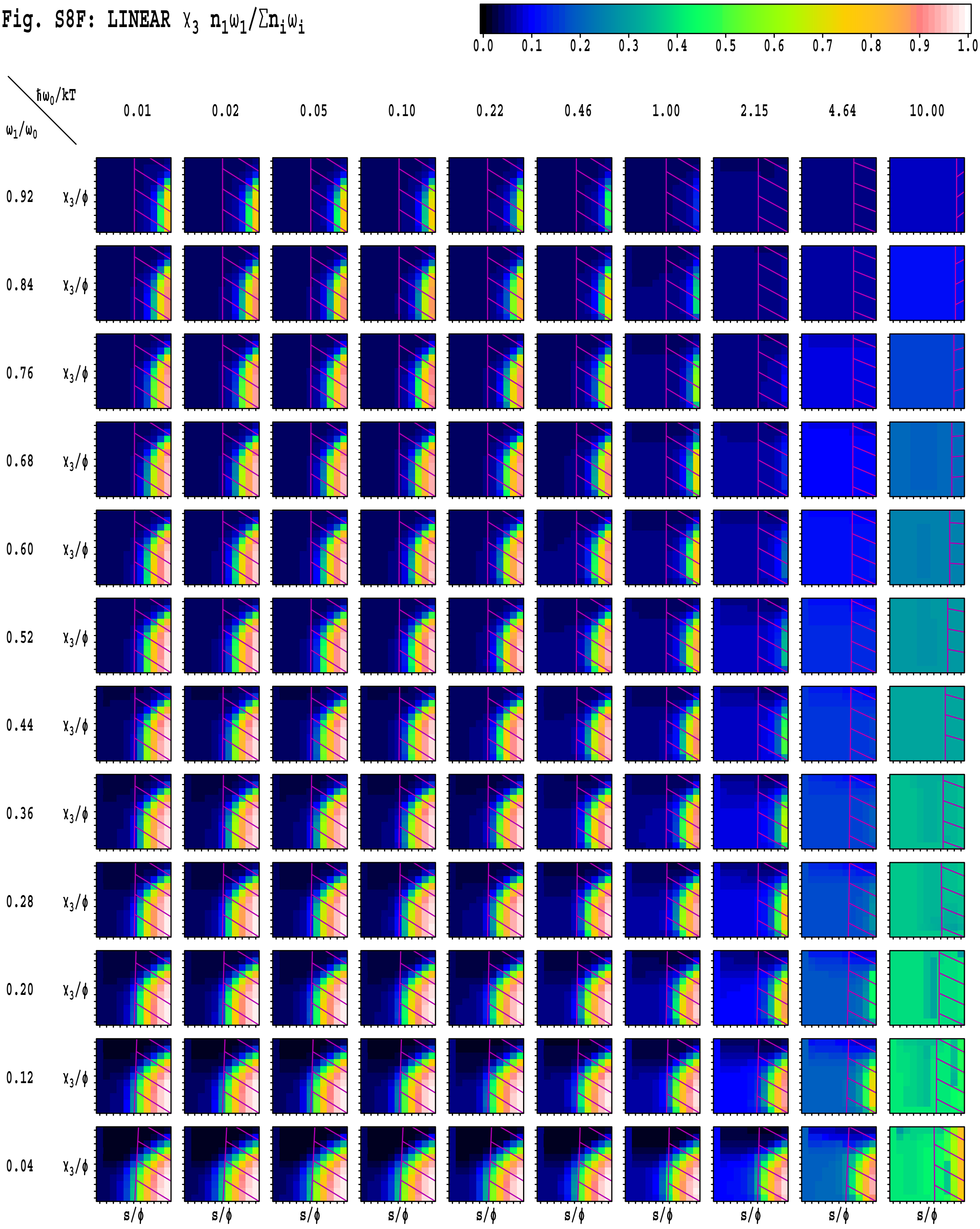

Fig. S8G: LINEAR χ_3 $n_1/n_1^{\chi=0}$

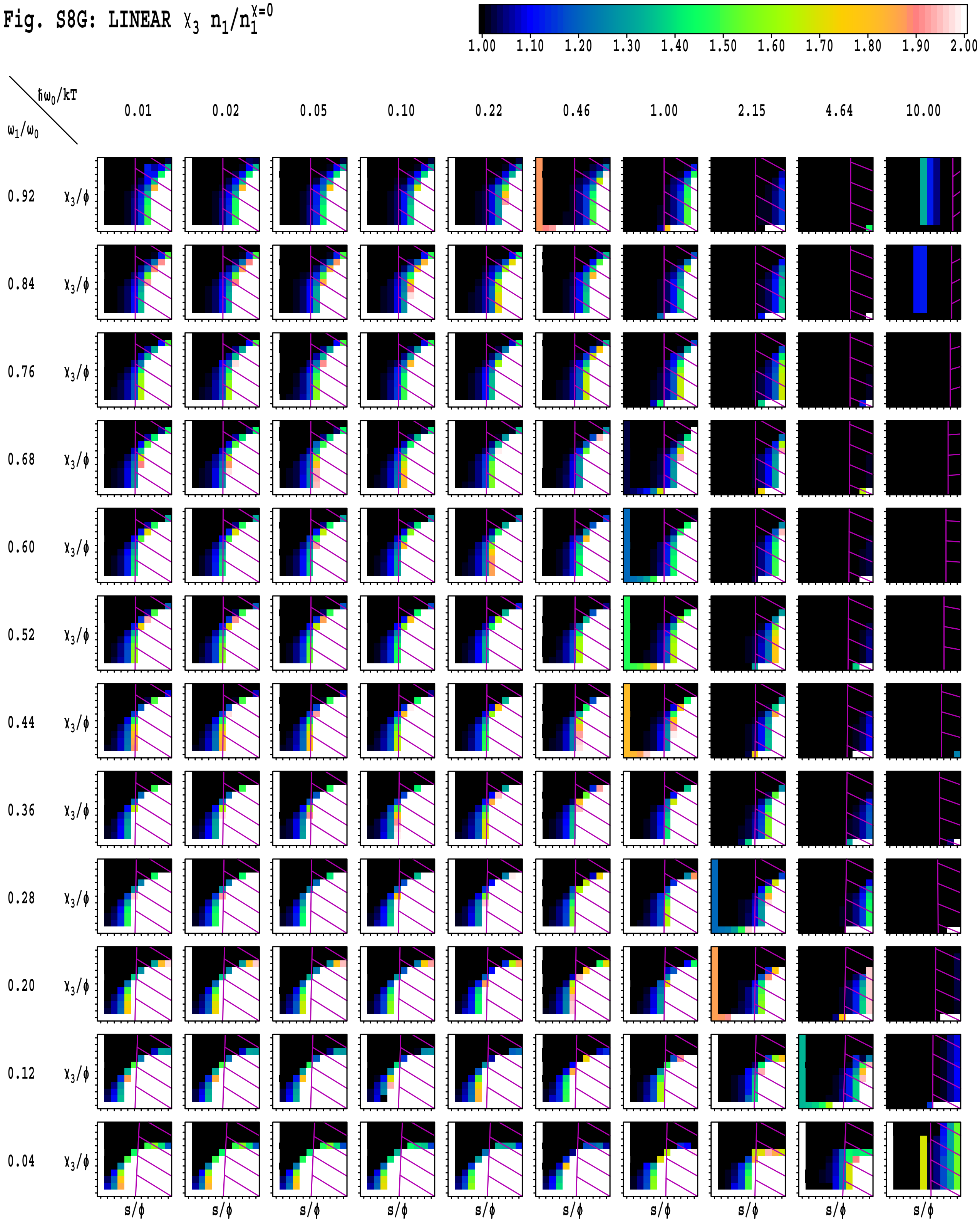

F. **Variations to the basic Fröhlich model**

We have shown that the appearance of the Fröhlich condensate and the significant perturbations to the energy partitioning that arise in partial condensates are both more prominent when the bandwidth is large. This raises the question as to whether the Fröhlich model, Eqns. 6-8, includes sufficient processes to properly represent actual physical phenomena. For example, for small values of ω_1/ω_0, the system modes can act as their own bath, allowing high-order scattering events to redistribute the system energy without requiring energy exchange with the external bath via Eqn. 8. Such higher-order terms can be approximated by an effective low-order equation of the form

$$L_i^3 = \chi_3 \sum_{j=1}^{Z} n_i (1+n_j) e^{\hbar(\omega_i - \omega_j)/kT_s} - n_j (1+n_i) \qquad (20)$$

We have evaluated the steady-state for this enhanced model at $\chi = 0.02$ and the results are given in detail in Figure S8. Condensation is completely inhibited when χ_3 exceeds χ, indicating that the relative importance of these two processes is critical. It is thus clear that any specific application of Fröhlich's model is non-trivial and requires the prior validation of the basic assumptions.

Another variation of the model which we considered was the application of random amounts of energy to each mode, with *s* then indicating the average power input per oscillator. The primary results were robust to this modification, indicating that delicate balancing of the energy sources is *not* required for condensation.

G. **Properties of the Wu-Austin Hamiltonian**

Obtaining Fröhich's energy relaxation rate ϕ and the associated coherence lifetime from the dynamics

In Fröhich's model the rate of energy relaxation to the bath is ϕ. This is identified as dE/dt at the zero-point level for a system mode in contact with a thermal bath at temperature T. Figure S9 shows the results obtained by averaging over 4000 trajectories using $Z_B = 6$ to 215 bath modes, with convergence achieved above 50 modes; the bath temperature is $T = 300$ K while one system oscillator is used, typically at $\omega_1 = 25\ \mathrm{cm}^{-1} \equiv 36$ K.

Figure S9A shows the energy flow into system mode 1 as a function of time. Four different values of the dynamical parameter α are used. As the total coupling is related to the total number of bath modes Z_B, the results are interpreted using the variable $Z_B\alpha$ which takes on values of $Z_B\alpha/k = 0.023$, 0.047, 0.092, 0.139, 0.46, and 4.6 K At each value of the coupling, a linear increase in the average mode-1 energy with time is seen. The slope of this response is the energy relaxation rate ϕ.

Figure S9B shows ϕ as a function of the coupling α plotted on a log-log scale over many orders of magnitude. A line is fitted to the data and indicates

$$\phi = 230\ (Z_B\alpha)^{1.86}\ \mathrm{ns} \quad \text{when } \alpha \text{ is in K.}$$

This is close to a quadratic dependence of the rate on the number of modes and the coupling strength per mode α. If the exponent is frozen at 2 then the coefficient becomes 200 $\mathrm{K}^{-1}\ \mathrm{ns}^{-1}$. Wu and Austin provide an expression for ϕ for each system mode:

$$\phi_i = \frac{\alpha^2}{\hbar} \sum_{j=1}^{Z_B} N(\Omega_j) N(\Omega_j + \omega_1) \exp\frac{\Omega_j}{kT_B}$$

where N is the number of quanta in a mode of the given frequency at equilibrium. This has the quadratic dependence on α and, as revealed by the simulations, but for large Z_B this value scales proportional to Z_B. Hence the Wu-Austin expression scales differently to Fröhich's phenomelogical quantity ϕ.

Figure S9B also shows the effect of varying ω_1. A small effect is anticipated based on Wu and Austin's equation. The calculated response is small but appears erratic.

Figure S9C shows the coherence time plotted against $Z_B\alpha$ on a log-log scale. A small dependence on the mode frequency is again seen, but at $\omega_1 = 25\ \mathrm{cm}^{-1}$ a straight line is fitted to the data that revels

$\tau = 0.81\ \mathrm{K\ ps} / (Z_B\alpha)^{0.92}$ ps when α is in K so the rate is $1/\tau = 1230\ (Z_B\alpha)^{0.92}\ \mathrm{ns}^{-1}$.

Hence the rate of decoherence is roughly proportional to the coupling whilst the rate of energy transfer is roughly proportional to the square of the coupling.

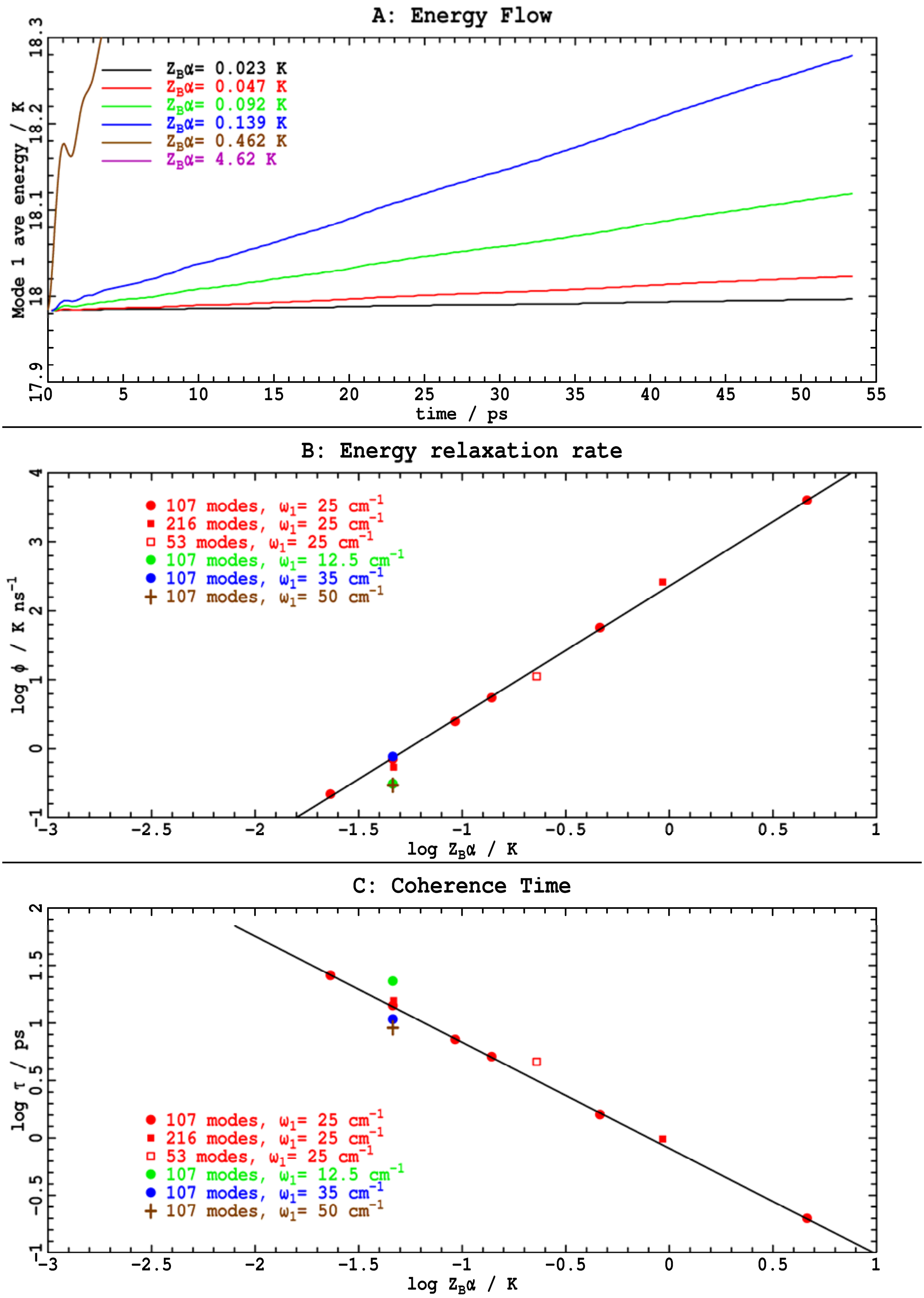

Figure S9: Effect of varying the number of modes and the coupling α on the rate of energy equilibration between the system and bath and on the associated coherence lifetime.

Energy relaxation vs. phase decoherence

While the energy relaxation rates of a few K per ns reported in the previous simulations are quite small, phase coherence is lost within a few ps. Figure S10 shows how the phase coherence is lost so quickly in this one-system-mode situation. Figure S10A shows the energy distribution in mode 1 evaluated at different times. All distributions are centred about the initial zero-point energy of half of 25 $\text{cm}^{-1} \equiv 18$ K. If the system oscillator was uncoupled from the bath then the energy would not vary and the distribution would be a delta function. As time proceeds, the dynamics takes ever increasing excursions to lower and higher energies. The net drift of the average energy is but a small fraction of the dynamical energy fluctuations, however. It is this feature that causes the coherence time to be much shorter than the energy relaxation time. This appears to be a generic property of the cubic coupling used in the model.

The rapid energy flow to and from the system mode causes the phase of the wavepacket to scramble. Figure S10B shows the dispersion of the phase produced after just one vibrational period of motion. It is spiked at $-\pi$ and would be a delta function at this value if there was no coupling with the bath. This phase shift generates the zero-point energy of the harmonic oscillator. As the bath coupling increases, large phase shifts arise even after one period. From a spectroscopic point of view, this is interpreted as: a large number of levels are thermally populated in the bath, and because of the anharmonicity the system oscillator frequency is perturbed by different amounts depending on the bath occupation, so the thermal motion causes the spectrum to broaden.

Shown in Figure S10C is the autocorrelation function (Eqn. 19) calculated for a range of couplings α. This shows how the increasing phase decoherence with increasing coupling causes the autocorrelation function to decay. Figure S10D shows one line from the spectra evaluated from these calculations using Eqn. 18. Note that the line is centred at $\hbar\omega/2 = 18$ K in accordance with the zero-point energy requirement. The coherence time is extracted from the full-width at half-maximum of the spectral line.

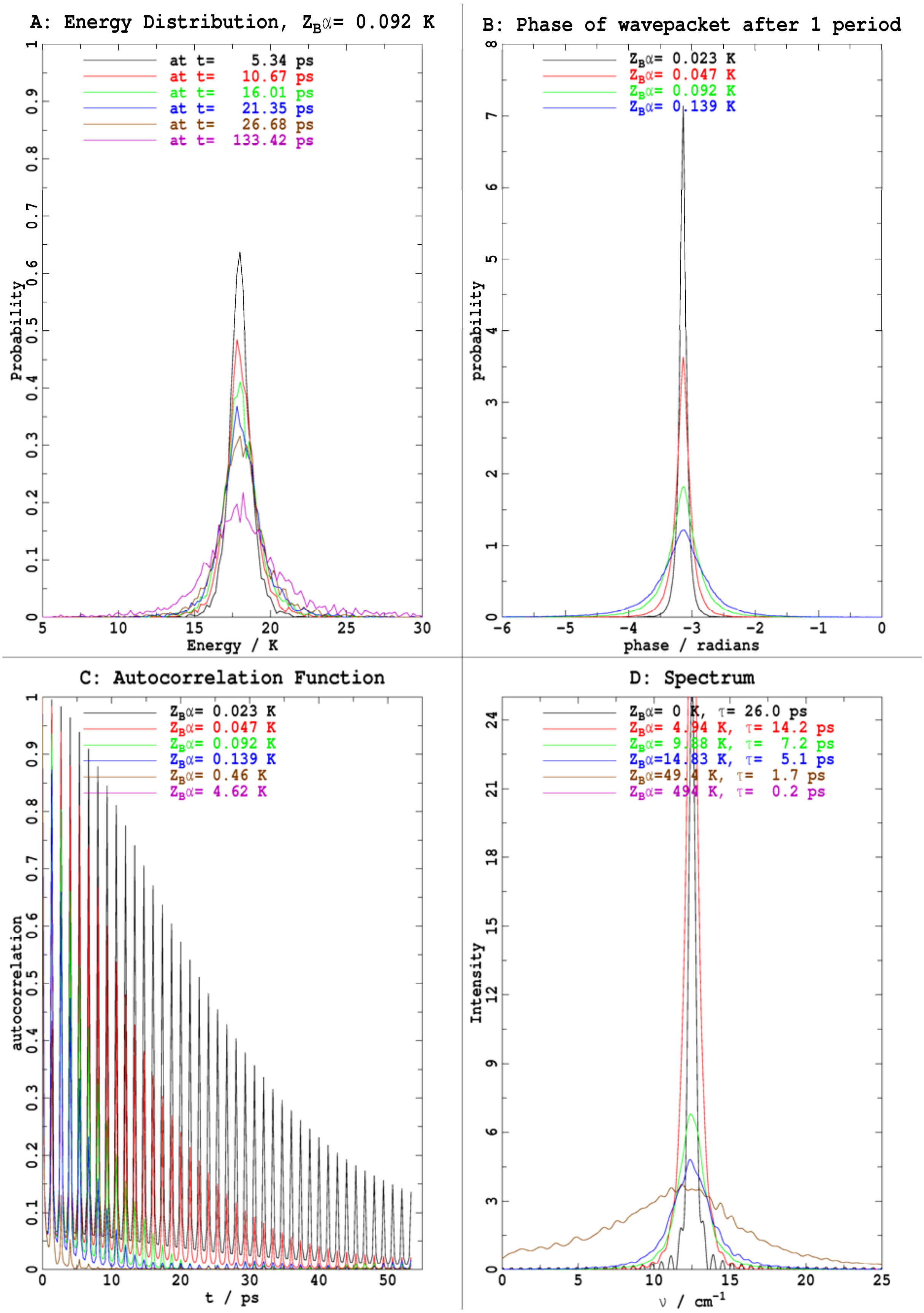

Figure S10: Understanding how the Wu-Austin Hamiltonian leads to phase decoherence at rates many orders of magnitude faster than the energy transfer rate.

Obtaining Fröhich's energy input rate s and the associated coherence lifetime from dynamics

Wu and Austin give the power absorbed by system mode *i* in the classical limit as

$$s_i = \frac{\gamma^2}{\hbar} Z_I \frac{k(T_I - T_{Si})}{\hbar\omega_i} = 91 \frac{\mathrm{cm}^{-1}}{\mathrm{K}^2\mathrm{ns}} \frac{Z_I \gamma^2 (T_I - T_{Si})}{\omega_i}$$

so that if γ and T are in K and ω in cm^{-1} then the calculated rate is in units of K/ns. Numerical results from simulations are shown in Figure S11. These simulations involve just one system oscillator initially at its zero-point energy. Figure S11A shows the increase in the energy of the system mode with time owing to the coupling with the input oscillators, while the initial slope s is plotted as a function of $Z_I\gamma^2(T_I\text{-}T_{S1})/\omega_1$ on a log-log scale. A linear correlation is indicated on this figure giving a slope of 0.98, very close to the expected value of one. Assuming a slope of one, the prefactor is determine to be 140 cm^{-1}/(K^{2}ns), 50% larger than the value expected based on the Wu-Austin result. The difference originates from the ways in which the frequency distributions of the source modes are treated. Wu and Austin assume low frequency so that the density of input states about the system oscillators does not vary with energy. In the calculations, a band of finite width (from 12.5 to 50 cm^{-1} for ω_1 = 25 cm^{-1}) is used. The differences are only minor, and the advantage gained in having a simple algorithm for specifying the input oscillator bandwidth across the whole Wu-Austin parameter space in a highly computationally efficient scheme is more significant than are these differences.

Figure S12C shows the calculated coherence lifetime as a function of $[Z_I^2\gamma^2(T_I\text{-}T_{S1})]^{1/2}$ plotted on a log-log scale. Proper analysis of the effect of the system oscillator frequency ω_1 on the coherence lifetime requires a more sophisticated algorithm for specifying the input oscillators than is used herein, however; all of the results shown are for ω_1 = 25 cm^{-1}. The linear correlation shown in the figure has a slope of -0.994 indicating a reciprocal relationship:

$$\tau = 27 \text{ ps K}^{3/2} \ [Z_I^2\gamma^2(T_I\text{-}T_{S1})]^{-1/2}$$

so the rate of decoherence is $1/\tau$ = 37 ns^{-1} K$^{-3/2}$ $[Z_I^2\gamma^2(T_I\text{-}T_{S1})]^{1/2}$. Hence the interaction of the system with the input oscillators has the same general property as does that with the thermal bath: the rate of energy transfer is proportional to the coupling squared whilst the rate of phase decoherence is proportional to the coupling.

A: Energy Flow

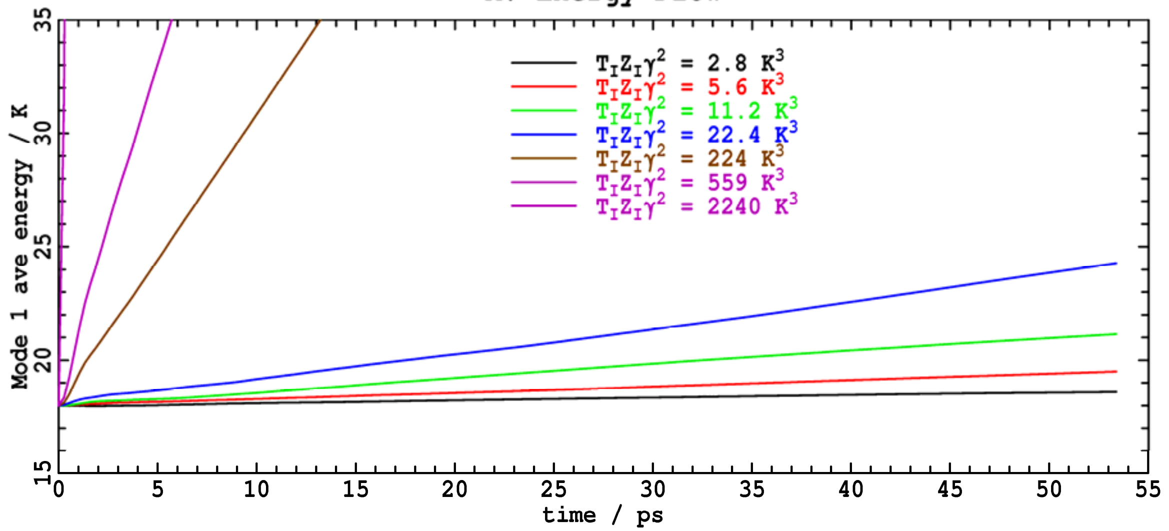

B: Energy relaxation rate

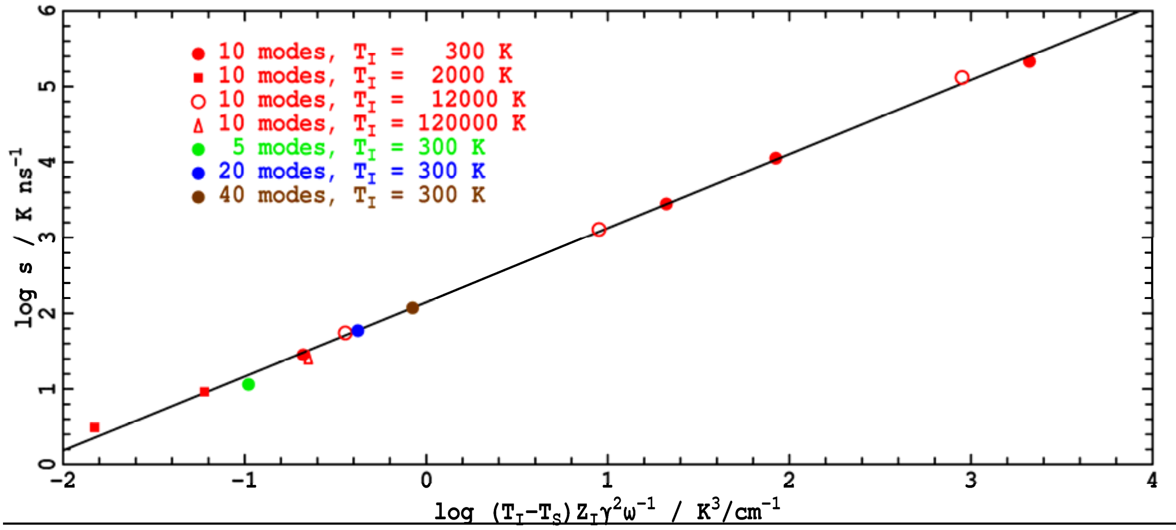

C: Coherence Time

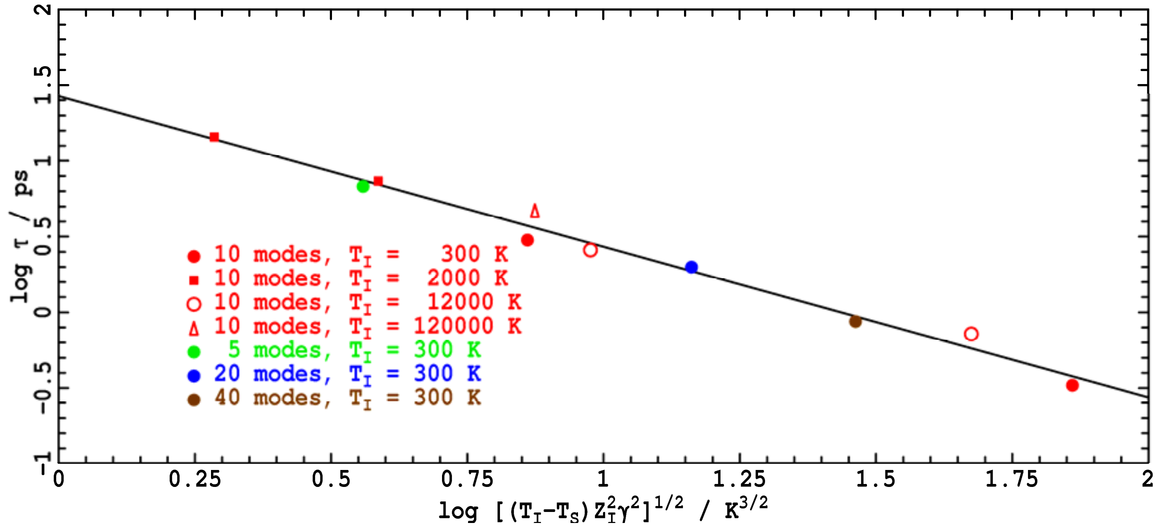

Fig. S11: Effect of varying the number of modes, the coupling γ, and the source temperature on the rate of energy flow from the input and on the associated coherence lifetime.

Strong Fröhlich condensate from the Wu-Austin Hamiltonian in the low-frequency narrow-band limit

Figure S12 shows the production of a strong Fröhlich condensate in the narrow-band high-temp. limit from an initial system in thermal equilibrium at 300 K. The development of the average kinetic energy in four of the $Z = 25$ system modes used in the simulation is shown, along with the instantaneous energy in the condensing mode, mode 1. The observed energy fluctuations are very large and indicate highly incoherent motion.

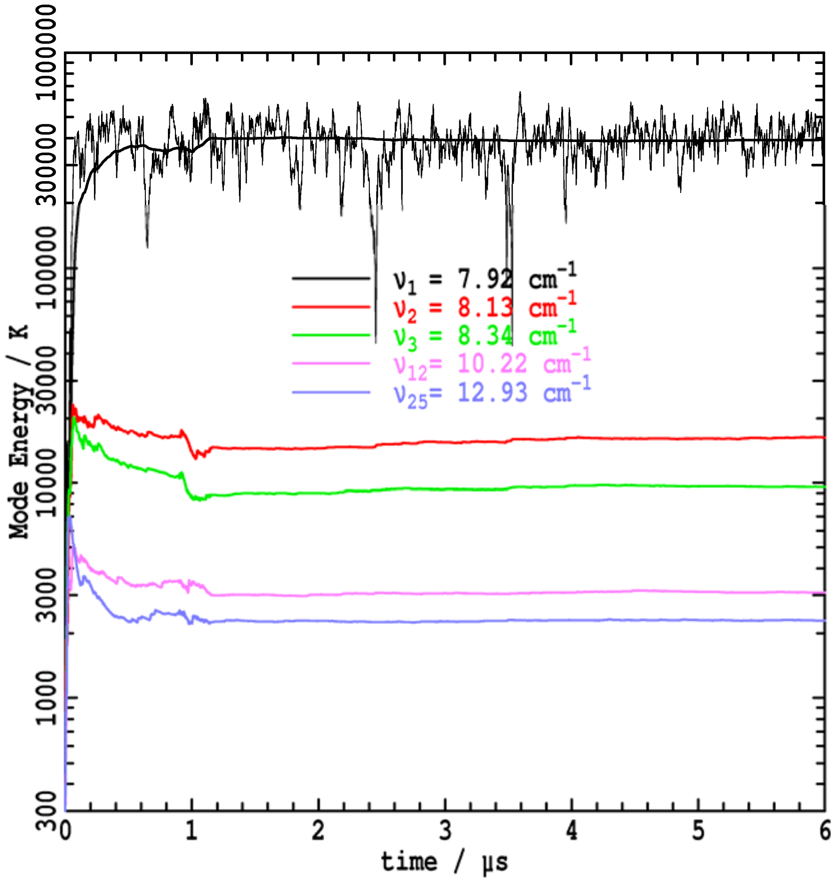

Fig. S12: Dynamics of the Wu-Austin Hamiltonian in the wide-band high-temp. limit ($\omega_1/\omega_0 = 0.76$, $\hbar\omega_0 / kT = 1/15$), showing the change in the average kinetic energy in modes 1 (the mode undergoing Fröhlich condensation), 2, 3, 12, and 25 for $Z = 25$ system oscillators; the instantaneous kinetic energy in mode 1 is also shown (thin line). Other parameters are: linear frequency dispersion, $Z_B = 430$ bath modes at $T = 300$ K (hence $\omega_0 = 10.425$ cm^{-1}, $\omega_1 = 7.923$ cm^{-1}), $Z_I = 200$ source modes at $T_I = 400000$ K, $\alpha/k = 53$ μK, $\beta/k = 75$ μK, $\gamma/k = 375$ μK.

Strong Fröhlich condensate from the Wu-Austin Hamiltonian in the high-frequency narrow-band limit

Figure S13 shows the production of a strong Fröhlich condensate in the narrow-band low-temp. limit from an initial system in thermal equilibrium at 300 K. The development of the average kinetic energy in four of the $Z = 25$ system modes used in the simulation is shown, along with the instantaneous energy in the condensing mode, mode 1, as well as in mode 2. The observed energy fluctuations are very large and indicate highly incoherent motion. The simulation conditions are similar to those used by Mesquita et al. for modelling Fröhlich condensation in the amide-I modes of proteins. Formation of the condensate requires exceptionally high input bath temperatures of at least 400000 K, while the system temperature of the condensate is typically also of this magnitude. Such a condensate could not form in a biological system. Condensates in this regime take over 100 times longer to form than do the condensates simulated in the high-temperature limit, requiring over 1 μs of simulation time.

Five individual trajectories are shown in Figs S13A-S13E, with the driving force for condensation increasing in order A to E. D-E use an input temperature of 400000 K but this is inadequate as the energy in the condensing mode increases to exceed this value; A-C use a much higher input temperature of 4 MK but the ratio of the input to bath coupling is less and so the condensate is not so well formed. For the least driven trajectories A and B, the partial formation of the condensate is apparent, with 15-40 % of the quanta exciting the lowest-frequency mode. The total energy in the condensing mode changes significantly with time, however, and at times more energy is found in mode 2 than in mode 1. Fig S13C shows a much better formed condensate with 60% of the quanta in the lowest mode, but again the fluctuations are large. Fourier transformation of the dynamics indicates that the fluctuations are white noise above ca. 20 MHz, but large oscillations are found in the 400 kHz region. Such profound fluctuations at low frequency may be a signature of strong mechanically formed condensates; in this case, the oscillator being driven is at 300 cm^{-1} so the system response is at 1/20000000 of the oscillator frequency! In the more strongly driven condensates shown in Figs S13D and S13E, the oscillators are suppressed but still apparent, and the condensing mode always has the largest occupancy.

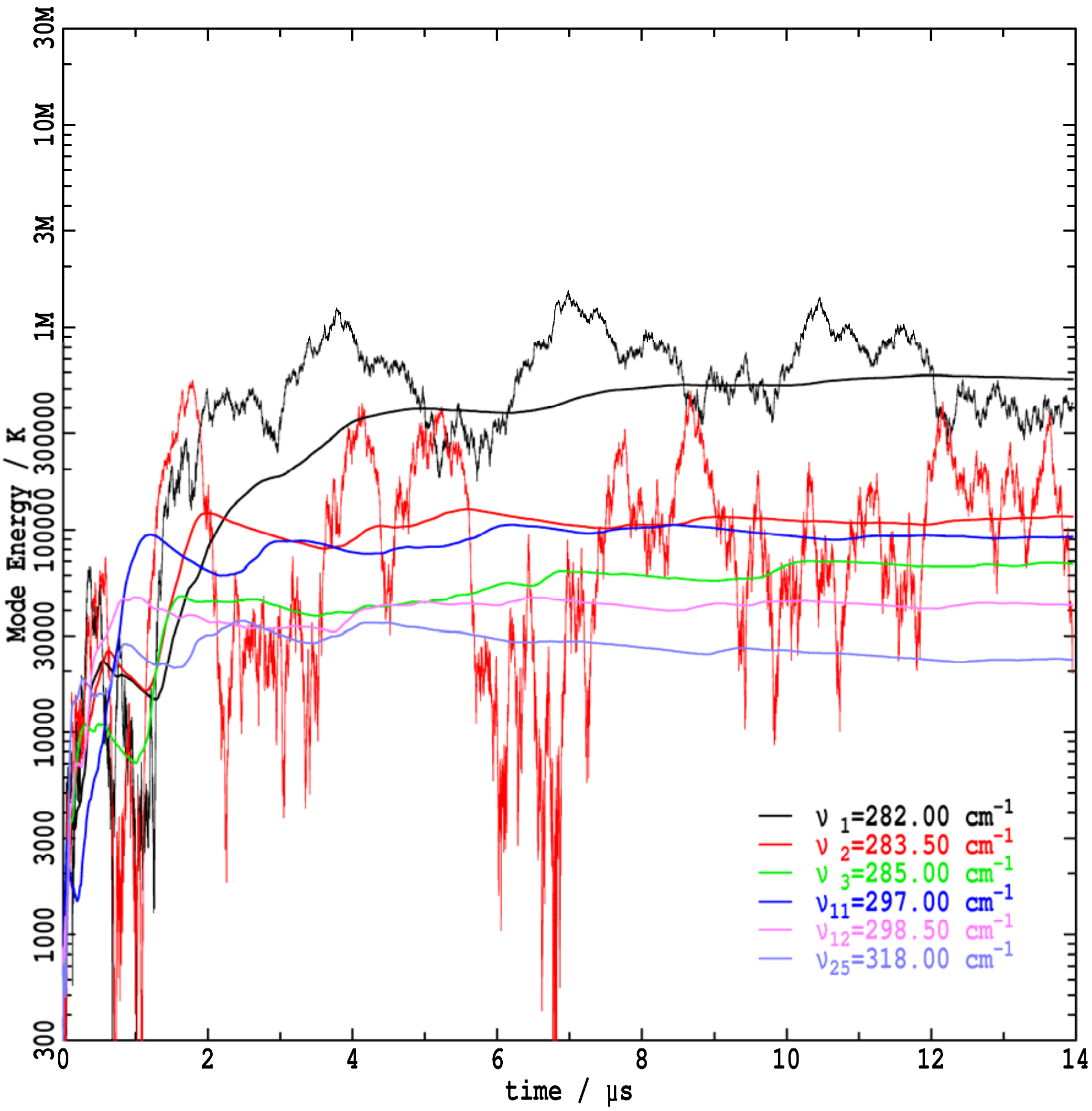

Fig. S13A: Dynamics of the Wu-Austin Hamiltonian in the wide-band low-temp. limit ($\omega_1/\omega_0 = 0.94$, $\hbar\omega_0 / kT = 1.46$), showing the change in the average kinetic energy in modes 1 (the mode undergoing Fröhlich condensation), 2, 3, 11, 12, and 25 for $Z = 25$ system oscillators; the instantaneous kinetic energy in modes 1 and 2 is also shown (thin lines). Other parameters are: linear frequency dispersion, $Z_B = 430$ bath modes at $T = 300$ K (hence $\omega_0 = 300$ cm^{-1}, $\omega_1 = 282$ cm^{-1}), $Z_I = 200$ source modes at $T_I = 4000000$ K, $\alpha/k = 860$ µK, $\beta/k = 2.16$ µK, $\gamma/k = 216$ µK.

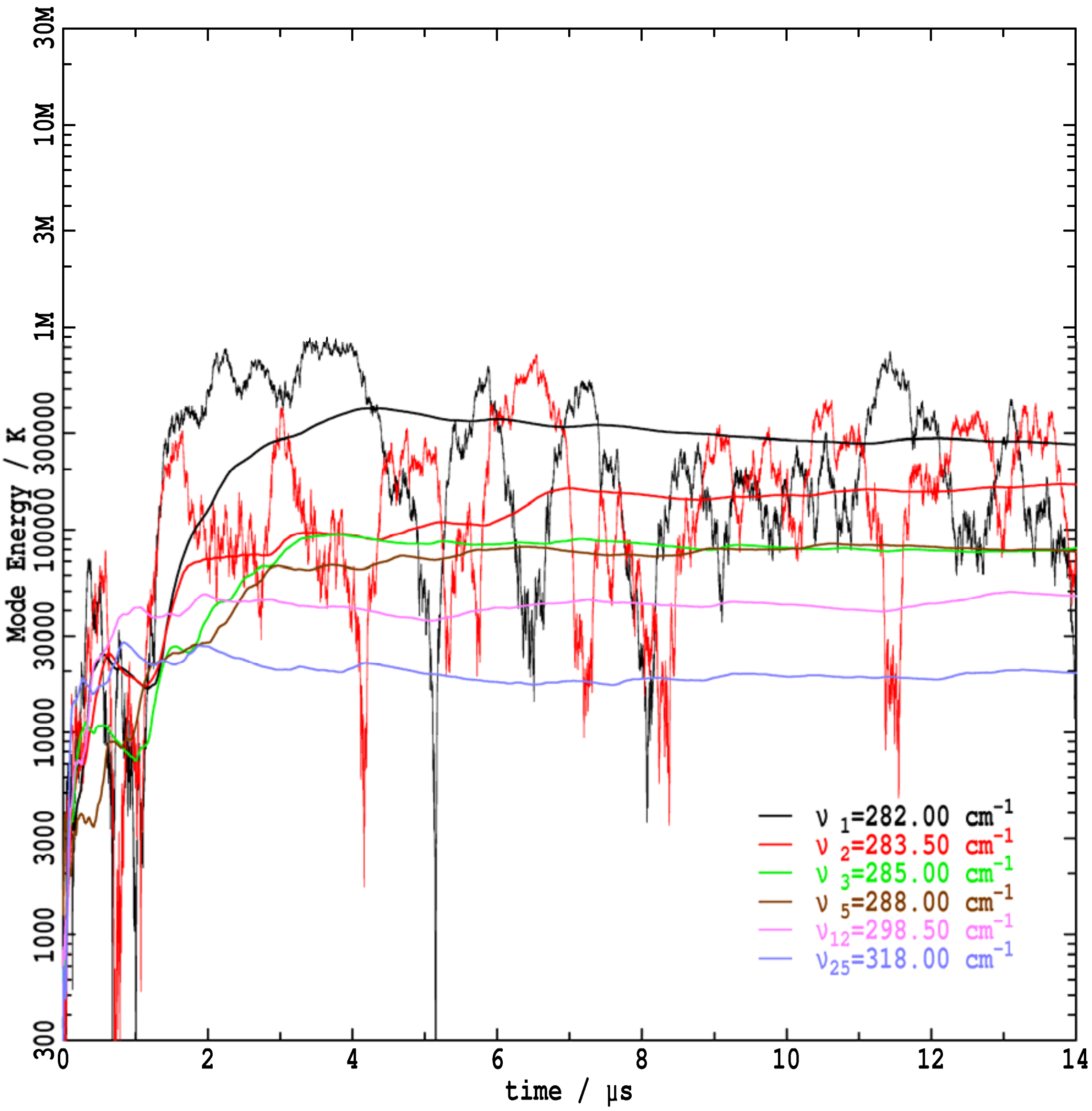

Fig. S13B: Dynamics of the Wu-Austin Hamiltonian in the wide-band low-temp. limit ($\omega_1/\omega_0 = 0.94$, $\hbar\omega_0 / kT = 1.46$), showing the change in the average kinetic energy in modes 1 (the mode undergoing Fröhlich condensation), 2, 3, 6, 12, and 25 for $Z = 25$ system oscillators; the instantaneous kinetic energy in modes 1 and 2 is also shown (thin lines). Other parameters are: linear frequency dispersion, $Z_B = 430$ bath modes at $T = 300$ K (hence $\omega_0 = 300$ cm^{-1}, $\omega_1 = 282$ cm^{-1}), $Z_I = 200$ source modes at $T_I = 4000000$ K, $\alpha/k = 860$ μK, $\beta/k = 8.6$ μK, $\gamma/k = 216$ μK.

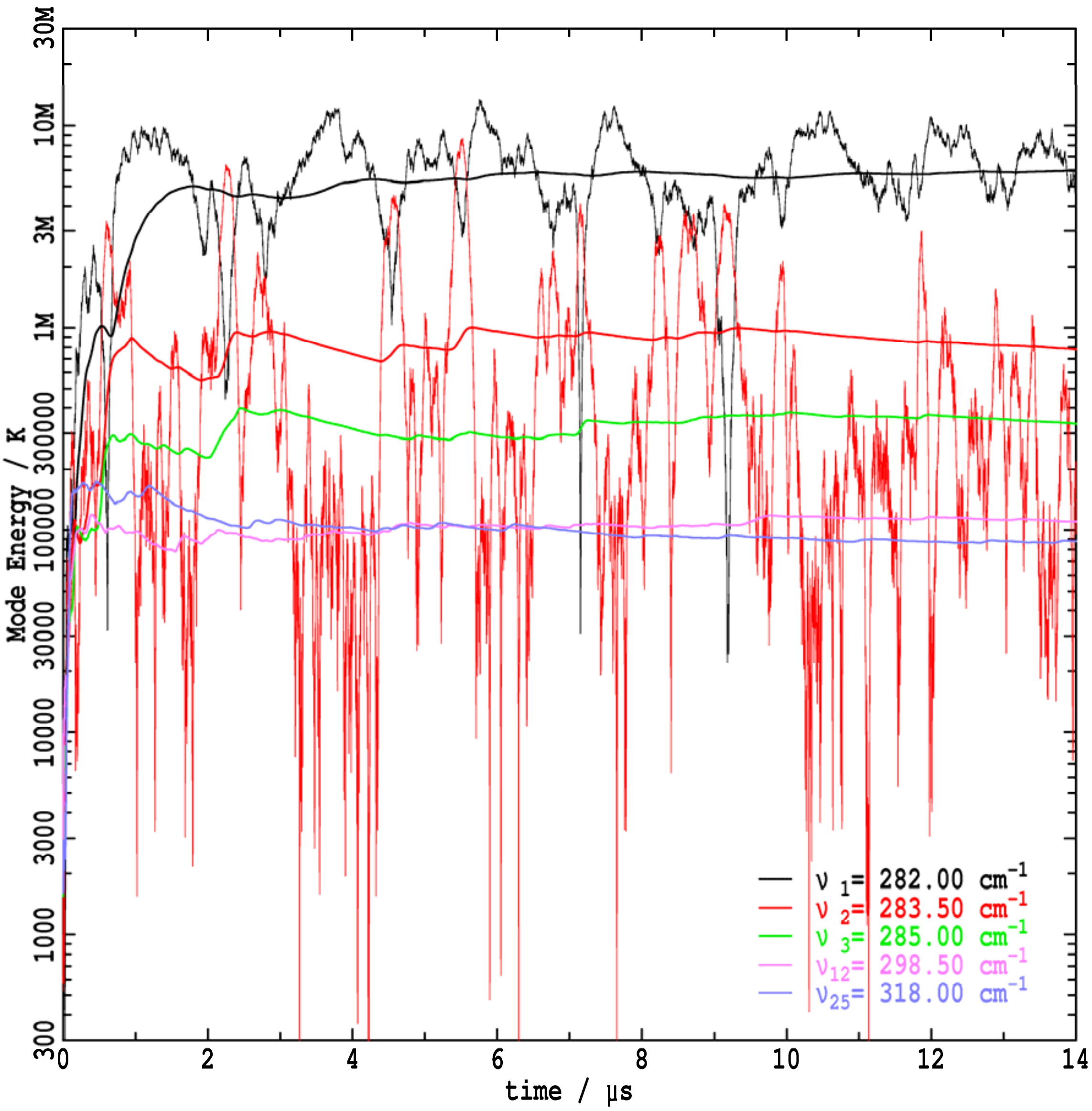

Fig. S13C: Dynamics of the Wu-Austin Hamiltonian in the wide-band low-temp. limit ($\omega_1/\omega_0 = 0.94$, $\hbar\omega_0 / kT = 1.46$), showing the change in the average kinetic energy in modes 1 (the mode undergoing Fröhlich condensation), 2, 3, 12, and 25 for $Z = 25$ system oscillators; the instantaneous kinetic energy in modes 1 and 2 is also shown (thin lines). Other parameters are: linear frequency dispersion, $Z_B = 430$ bath modes at $T = 300$ K (hence $\omega_0 = 300$ cm^{-1}, $\omega_1 = 282$ cm^{-1}), $Z_I = 200$ source modes at $T_I = 4000000$ K, $\alpha/k = 860$ μK, $\beta/k = 8.6$ μK, $\gamma/k = 860$ μK.

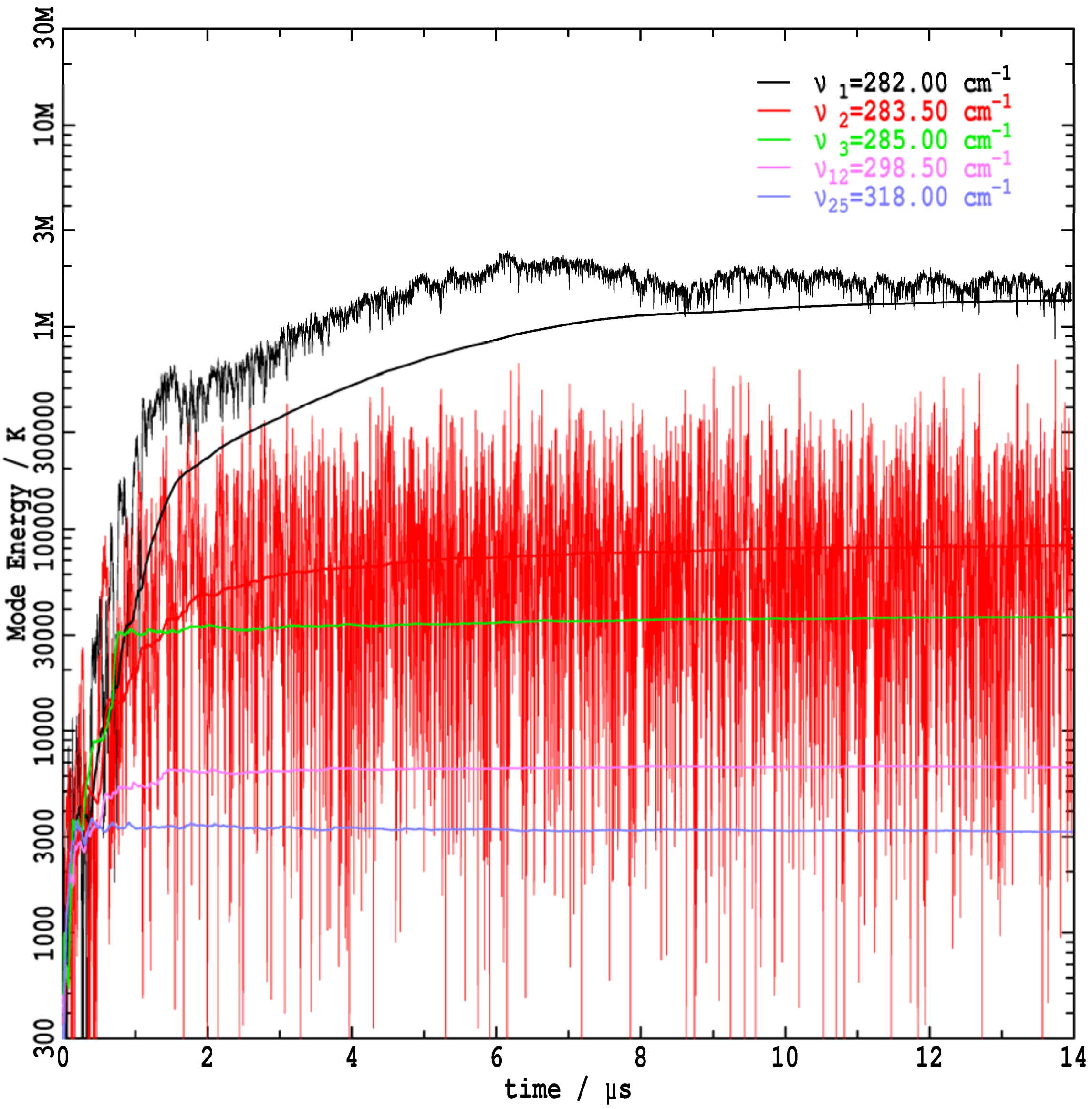

Fig. S13D: Dynamics of the Wu-Austin Hamiltonian in the wide-band low-temp. limit ($\omega_1/\omega_0 = 0.94$, $\hbar\omega_0 / kT = 1.46$), showing the change in the average kinetic energy in modes 1 (the mode undergoing Fröhlich condensation), 2, 3, 12, and 25 for $Z = 25$ system oscillators; the instantaneous kinetic energy in modes 1 and 2 is also shown (thin lines). Other parameters are: linear frequency dispersion, $Z_B = 430$ bath modes at $T = 300$ K (hence $\omega_0 = 300$ cm^{-1}, $\omega_1 = 282$ cm^{-1}), $Z_I = 200$ source modes at $T_I = 400000$ K, $\alpha/k = 86$ μK, $\beta/k = 216$ μK, $\gamma/k = 430$ μK.

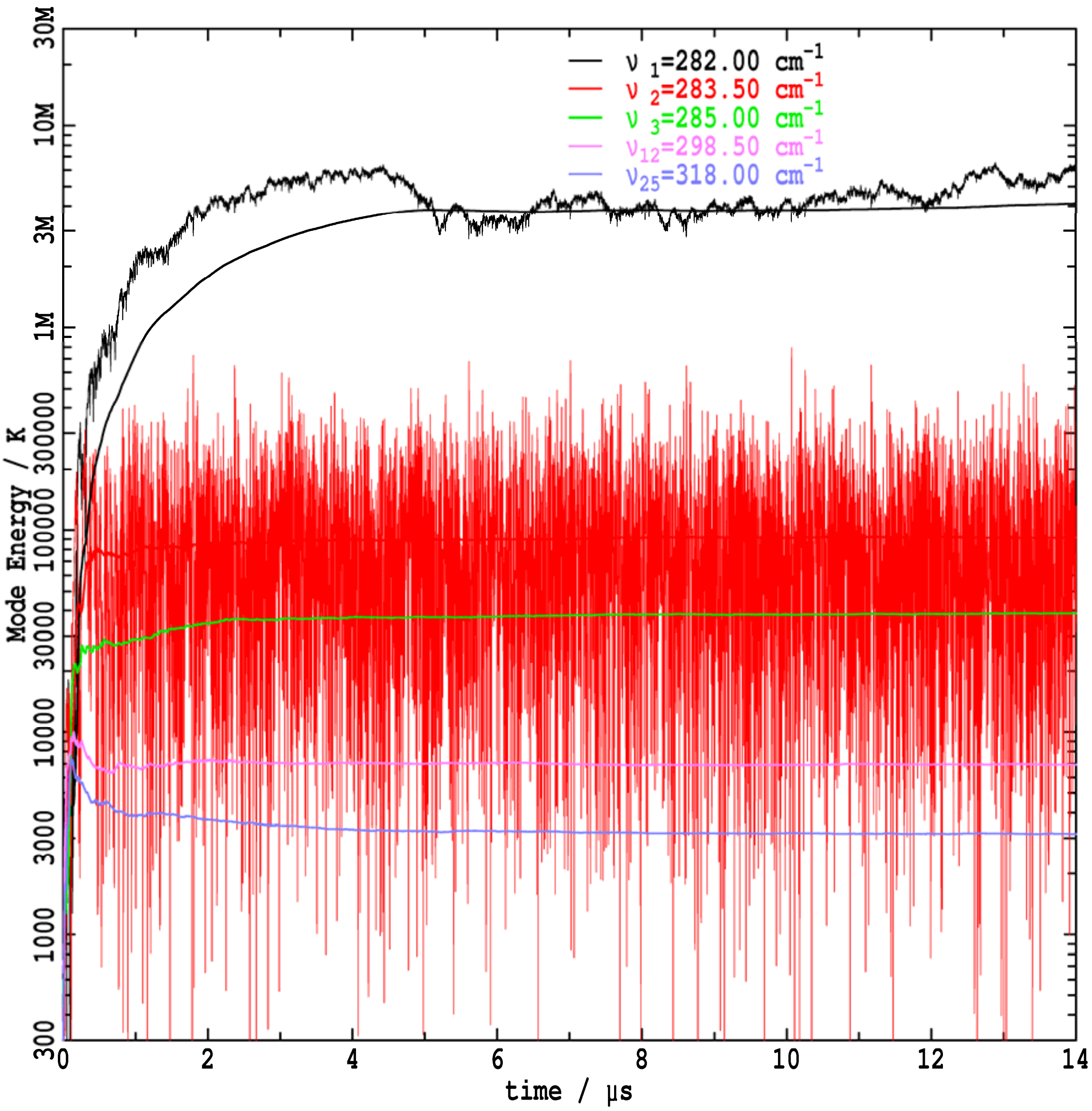

Fig. S13E: Dynamics of the Wu-Austin Hamiltonian in the wide-band low-temp. limit ($\omega_1/\omega_0 = 0.94$, $\hbar\omega_0 / kT = 1.46$), showing the change in the average kinetic energy in modes 1 (the mode undergoing Fröhlich condensation), 2, 3, 12, and 25 for $Z = 25$ system oscillators; the instantaneous kinetic energy in modes 1 and 2 is also shown (thin lines). Other parameters are: linear frequency dispersion, $Z_B = 430$ bath modes at $T = 300$ K (hence $\omega_0 = 300$ cm^{-1}, $\omega_1 = 282$ cm^{-1}), $Z_I = 200$ source modes at $T_I = 400000$ K, $\alpha/k = 86$ µK, $\beta/k = 216$ µK, $\gamma/k = 860$ µK.

Kinetic-energy distribution function for strong Fröhlich condensates derived from the Wu-Austin Hamiltonian

How the Wu-Austin Hamiltonian, with Nose-Hoover thermostats depicting the thermal baths, anticipates but does not achieve coherent motion is demonstrated in Figure S14. Here, the probability of finding mode 1 with a kinetic energy ratio of E/E_{av} is shown, where E is the instantaneous kinetic energy and E_{av} is the average kinetic energy of the mode in the condensate. Shown for reference are the probability functions expected for a canonical energy distribution and for coherent motion. While weak condensates (not shown) lead to nearly canonical energy distributions, the strong condensates depicted in the figure all have probability distributions akin to that expected for coherent motion at low energy but at high energy distorted canonical-like distributions are actually found. *Across the whole of the parameter space, we thus see that the Wu-Austin Hamiltonian does not lead to coherent Fröhlich condensates.*

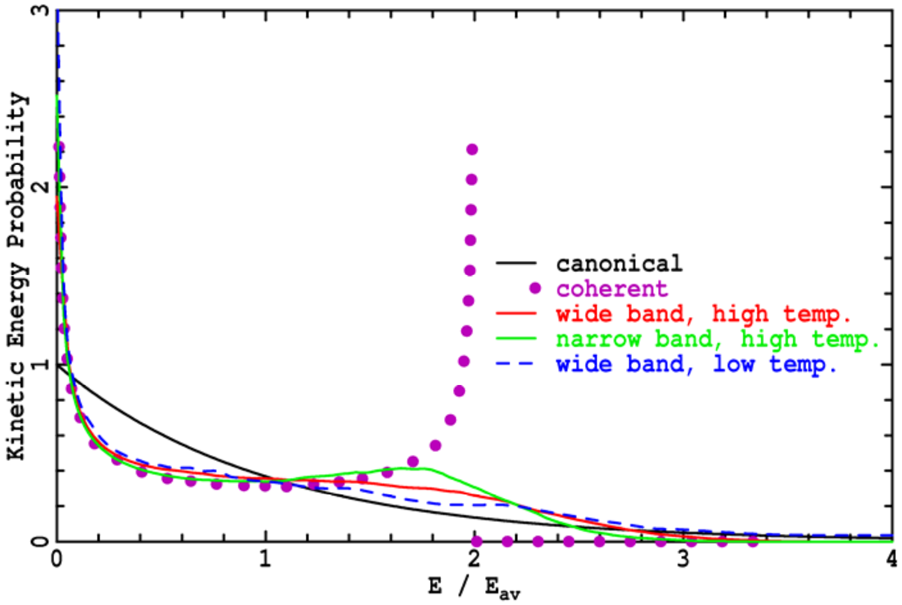

Fig. S14: Kinetic-energy distribution of the mode undergoing Fröhlich condensation as depicted by the Wu-Austin Hamiltonian in the wide-band low-frequency limit ($\omega_I/\omega_0 = 0.12$, $\hbar\omega_0 / kT = 1/15$), the narrow-band low-frequency limit ($\omega_I/\omega_0 = 0.76$, $\hbar\omega_0 / kT = 1/15$), and the narrow-band high-frequency limit ($\omega_I/\omega_0 = 0.94$, $\hbar\omega_0 / kT = 1.46$); for reference, standard classical canonical and coherent kinetic-energy profiles are also provided, where E is the kinetic energy and E_{av} is the average kinetic energy. The simulation conditions are: linear frequency dispersion, $Z = 25$ system oscillators, $Z_B = 430$ bath modes at $T = 300$ K, $Z_I = 200$ source modes at $T_I = 96000$ K (wide band, high temp.) 400000 K (narrow band, high temp.) and 4000000 K (narrow band, low temp.), with $\alpha/k = 150$ μK, $\beta/k = 150$ μK, $\gamma/k = 750$ μK (wide band, high temp.), $\alpha/k = 53$ μK, $\beta/k = 75$ μK, $\gamma/k = 375$ μK (narrow band, high temp.) and $\alpha/k = 860$ μK, $\beta/k = 8.6$ μK, $\gamma/k = 860$ μK (narrow band, low temp.).

H. Minimum system temperature required to attain a condensation index of η = 0.9 from the basic Fröhlich model

Mesquita et al. (*17, 18*) found that the coherence lifetime increased sharply in the strong-condensate regime, with in our language $\eta > 0.9$ typically required. Of the 29040 calculations performed for the construction of Figs. S1-S8 (see Supporting Information) depicting the general solution to Fröhlich's, the *minimum* calculated system temperature T_S found whenever $\eta > 0.9$ occurs for the widest bands ($\omega_1/\omega_0 = 0.04$) and the strongest sources ($s/\phi = 100$) and is sensitive to the number of oscillators Z. While the minimum value of T_S tends to decrease with increasing Z as more modes are available to be drained to form the condensate, the greater density of available low-frequency vibrations has the opposite effect; the resulting calculated minimum T_S is shown as a function of Z for cosine, linear, and Gaussian dispersion in Supporting Information Figure S15. For the cosine dispersion appropriate for a linear chain of coupled oscillators as envisaged in the Orch OR proposal, the competing effects result in a minimum system temperature for coherence of 1560 K for ca. $19 \le Z \le 46$. For linear dispersion, the minimum system temperature is 750 K for ca. $45 \le Z \le 600$, the lower temperature being facilitated by the lower density of states in the vicinity of ω_1. For Gaussian dispersion the coherence is most enhanced, the minimum system temperature required being 460 K whenever $600 \le Z \le$ at least 10000. In the low-temperature limit originally considered by Mesquita et al. pertinent to Fröhlich condensates involving protein amide-I vibrations, our simulations in Supporting Information Fig. S13 indicate that the condensing mode attains an energy corresponding to a temperature of order 10^5 to 10^7 K, indicating that the envisaged biological process is not feasible.

The simulations of Mesquita showed Fröhlich condensation under a modified Wu-Austin Hamiltonian in which input decoherence is suppressed through the replacement of the explicit mechanical energy source with a general macroscopic term. Coherent condensates were produced for η > 0.9. Here we take the basic Fröhlich model and determine the lowest system temperature available anywhere in the parameter space for different numbers of system modes *Z* and dispersion types. This temperature is very high for all dispersion types but is largest for a linear chain of oscillators showing cosine-type dispersion.

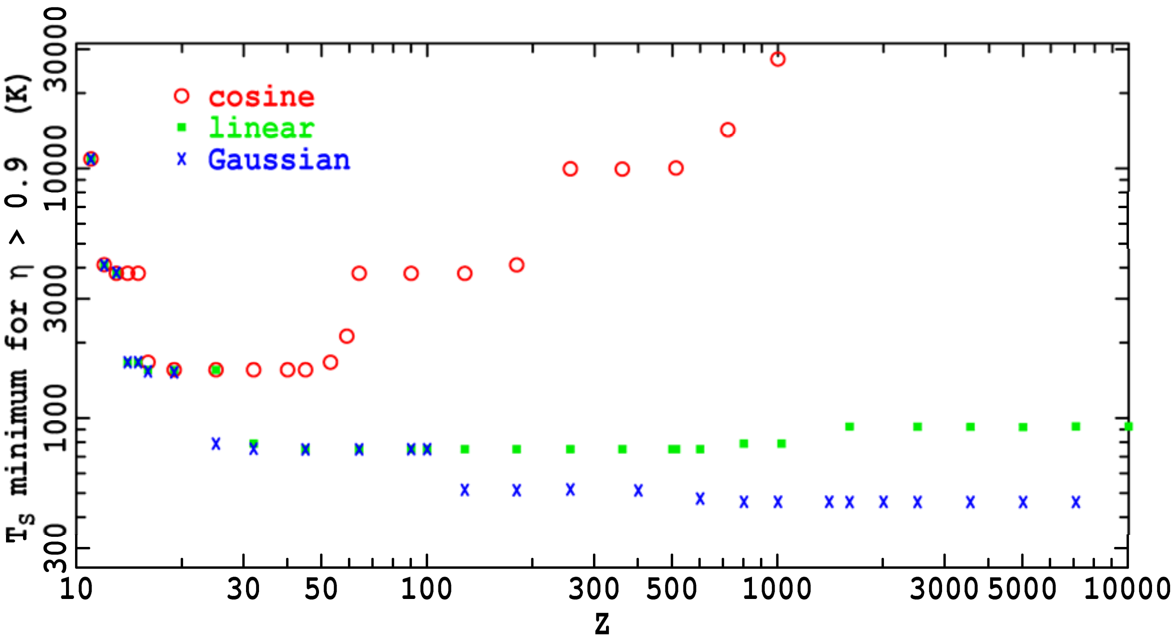

Fig. S15: Minimum system temperature required to reach the high condensation index of η = 0.9. These are obtained considering all data evaluated on the four-dimensional grids with s/ϕ = 0, 0.010, 0.028, 0.077, 0.22, 0.76, 1.67, 4.64, 12.9, 35.9, and 100; χ/ϕ = 0, 0.00010, 0.00028, 0.00077, 0.0022, 0.0060, 0.046, 0.13, 0.36, and 1; $\hbar\omega_0 / kT$ = 0.010, 0.022, 0.046, 0.10, 0.22, 0.46, 1.0, 2.2, 4.6, 10.0; and ω_1/ω_0 = 0.04, 0.12, 0.20, 0.28, 0.36, 0.44, 0.52, 0.60, 0.68, 0.76, 0.84.0.92 using cosine, linear, or Gaussian dispersion for *Z* in the range of 2 to 10000 oscillators